

Electronic Thesis and Dissertation Repository

---

9-15-2017 2:30 PM

## Fabrication and Characterization of CuInS<sub>2</sub> and CuInSe<sub>2</sub> Light-Absorbing Thin Films for use in Solar Cells

Amy R. Tapley, *The University of Western Ontario*

Supervisor: Dr. Zhifeng Ding, *The University of Western Ontario*

A thesis submitted in partial fulfillment of the requirements for the Doctor of Philosophy degree in Chemistry

© Amy R. Tapley 2017

Follow this and additional works at: <https://ir.lib.uwo.ca/etd>

 Part of the [Analytical Chemistry Commons](#), and the [Materials Chemistry Commons](#)

---

### Recommended Citation

Tapley, Amy R., "Fabrication and Characterization of CuInS<sub>2</sub> and CuInSe<sub>2</sub> Light-Absorbing Thin Films for use in Solar Cells" (2017). *Electronic Thesis and Dissertation Repository*. 4903.  
<https://ir.lib.uwo.ca/etd/4903>

This Dissertation/Thesis is brought to you for free and open access by Scholarship@Western. It has been accepted for inclusion in Electronic Thesis and Dissertation Repository by an authorized administrator of Scholarship@Western. For more information, please contact [wlsadmin@uwo.ca](mailto:wlsadmin@uwo.ca).

## Abstract

Solar energy is free and globally abundant and harnessed cost-effectively, it has the potential to be the world's main source of energy.  $\text{CuInGa(S,Se)}_2$  solar cells have a very high efficiency of 20 %. However, gallium is a rare and expensive element. We have decided to work on its alternative  $\text{CuInSe}_2$  (CISe) and  $\text{CuInS}_2$  (CIS) by removing gallium or both gallium and selenium. The p-type CISe or CIS light-absorbing semiconducting layer is crucial for this type of solar cell. Preparation methods for CIS and CISe films were developed to reduce the costs and enhance the photoelectrochemical efficiency.

The first preparation method was a low-temperature, one-pot, solvothermal synthesis of CIS nanocrystals (NCs) using metal salts as precursors, which was optimized based on a photoelectrochemical (PEC) measurement. The resultant NCs were fully characterized in Chapter 2 by conventional analytical and physical methods such as XRD, EDX, SEM, XPS, and TEM. X-ray absorption near edge structure (XANES) was utilized to not only investigate the absence of secondary phases and oxidation states, but also to obtain information about the connectivity of the capping ligand, effects of composition on the electronic structure of the materials, and the position of the conduction band (Chapter 3).

A linker molecule (3-mercaptopropyl) trimethoxysilane (MPTMS) was utilized to link the back contact to the CIS NCs. The monolayer, when tested with PEC measurements, produced a similar photocurrent density to much thicker films of CIS NCs. Polarization XANES was carried out to assess the CIS NC orientation (Chapter 4).

NC films were cast in a variety of ways including spin-coating and drop-casting. The addition of the next layer, CdS, in the full device fabrication was also investigated. It was discovered that a low-temperature annealing process of the CIS/CdS bilayer followed by an additional CdS layer produced a significant photocurrent enhancement (Chapter 5).

Also explored was the successive electrochemical deposition of copper and indium followed by selenization to form CISE. All films formed by these methods were fully characterized using conventional techniques as well as XANES and extended X-ray absorption fine structure (EXAFS) (Chapter 6).

## Keywords

CuInS<sub>2</sub> (CIS), CuInSe<sub>2</sub> (CISe), chalcopyrite, CdS, thin films, linker molecule, monolayer Solvothermal preparation, Nanocrystals, photoelectrochemistry, solar cells, light-absorbing layer, synchrotron radiation, X-ray absorption near edge structure (XANES), extended X-ray absorption fine structure (EXAFS), electrochemical deposition (ECD)

## Co-Authorship Statement

This thesis contains the work of three published manuscripts, found in chapters 2, 3 and 5 while chapters 4 and 6 represent submitted manuscripts. Below is a list, by chapter, of the coauthors and their contributions.

Chapter 2: Tapley, A.; Vaccarello, D.; Hedges, J.; Jia, F.; Love, D. A.; Ding, Z.; *Phys. Chem. Chem. Phys.* **2013**, *15*, 1431-1436. The methodology and experimental approach was proposed by ZD and FJ. JH and AT synthesized all compounds. DAL provided industrial funding for the project. AT performed all characterization and wrote the manuscript with editing and finalization by ZD. Reprinted with permission copyright 2013, Royal Society of Chemistry.

Chapter 3: Tapley, A.; Liu, L.; Cui, X.; Zuin, L.; Love, D. A.; Zhou, J.; Sham, T.-K.; Ding, Z.; *J. Phys. Chem. C* **2015**, *119*, 20967-20974. The experimental approach was designed by ZD, JZ and AT. DAL provided industrial funding for the project. JZ carried out the experiments at the Canadian Light Source. AT synthesized the compounds, performed the optical and electro-analysis, and wrote the manuscript. LL, XC, LZ, TKS, and ZD aided in editing and ZD finalized the manuscript. Reprinted with permission copyright 2015, American Chemical Society.

Chapter 4: Tapley, A.; Love, D. A.; Sham, T.-K.; Ding, Z. *Submitted*. **2017** Experimental approach was designed by AT, TKS and ZD. AT synthesized all compounds and ran all the experiments and wrote the manuscript. DAL provided industrial funding for the project. ZD and TKS aided in editing and ZD in finalizing the manuscript.

Chapter 5: Tapley, A.; Hart, C.; Vaccarello, D.; Love, D. A.; Ding, Z. *J Electrochem Soc* **2014**, *161* (12), H725-H729 AT and CH did all the experimental work and synthesized the samples. AT repeated the experiments and wrote the manuscript. DAL provided industrial funding to the project. DV and ZD edited the manuscript and ZD finalized the manuscript. Reprinted with permission, copyright 2014 The Electrochemical Society.

Chapter 6: Tapley, A.; Turnbull, M. J.; Swick, K.; Ding, Z. *Submitted*. **2017**

Experimental approach and design were proposed by AT, MT and ZD. KS aided in the optimization of the electroplating. MJT performed and analyzed the synchrotron data. AT wrote the manuscript and refined the synthetic approach used by KS. The manuscript was edited and finalized by ZD.

## Acknowledgments

I would first like to thank Dr. Zhifeng Ding for all his support and guidance during my studies. His dedication to science and his teaching abilities are without equal. I am grateful for having been a part of his research group and I know without his aid I would not be the scientist I am today. I would also like to thank Drs. Tsun-Kong Sham and Yun-Mui Yiu. With their understanding and patience I was able to better understand synchrotron radiation. The time they took to sit down with me and help me with synchrotron data was greatly appreciated.

I appreciate the vast amount of support given by the Chemistry Electronic Shop, Surface Science Western, the Biotron, the office staff, Aneta Borecki, as well as funding and scholarship agencies. The people involved in these organizations were always friendly and willing to help.

During my studies at Western I have had the privilege to work with a variety of excellent scientists whose skills are only exceeded by their kindness. I would like to thank Jane Stockmann, Kalen Swanick, Daniel Vaccarello, Kyle Jeffs, Sara Khoshmashrab, Michelle Li, Fraser Filice, Lorenzo Perini, Xuejin Wang, Kelsey Swick, Connor Hart, and Mahdi Hesari. I would also like to thank the people I shared the office MSA 0250 with for all their help and patience during my years.

My family was an integral part of this thesis, their love and support throughout have made my work possible. Both of my parents, Nancy and Noel Tapley and my sister Jennifer Denis always loved and encouraged in every endeavor I have ever undertaken. They believed in me even when I didn't and helped me through every step of the way.

Finally, I would like to thank my husband, Mike Gossmann. Your love and patience have kept me going during all my lengthy studies. I appreciate all you did to make sure I finished my degree. You make me a better scientist and a better person, you are my best friend, my guide and above all else, the love of my life. I am so grateful that I get to spend the rest of my life with you.

## Table of Contents

Abstract.....	i
Co-Authorship Statement.....	iv
Table of Contents.....	vii
List of Tables .....	xi
List of Figures .....	xii
List of Abbreviations .....	xvii
1 Introduction.....	1
1.1 Solar Cell Generations .....	2
1.2 CuInS <sub>2</sub> and CuInSe <sub>2</sub> .....	3
1.3 Semiconductors.....	4
1.4 p-n Junction.....	5
1.5 Tools for Characterization .....	6
1.5.1 Photoelectrochemical Measurement .....	6
1.5.2 Conventional Characterization.....	7
1.5.3 Synchrotron Radiation .....	8
1.6 Scope of Thesis .....	10
1.7 References.....	11
2 Preparation and Characterization of CuInS <sub>2</sub> Nanocrystals for Photovoltaic Materials.....	13
2.1 Introduction.....	13
2.2 Experimental.....	14
2.2.1 Characterization .....	14
2.3 <i>Results and Discussions</i> .....	16



2.3.1	Synthesis .....	16
2.3.2	Photoelectrochemical Measurements.....	17
2.3.3	Composition.....	21
2.3.4	Morphology.....	23
2.3.5	X-ray Diffraction .....	24
2.3.6	Oxidation States .....	25
2.4	Conclusion .....	27
2.5	References.....	27
3	Assessing the Band Structure of CuInS <sub>2</sub> Nanocrystals and Their Bonding with the Capping Ligand.....	30
3.1	Introduction.....	30
3.2	Experimental.....	32
3.3	Results and Discussions.....	34
3.3.1	Correlation of Initial Element Ratios to Photoresponse .....	34
3.3.2	Determination of CIS Nanocrystal Band Gap .....	35
3.3.3	X-ray absorption near edge spectroscopy .....	38
3.3.4	Band structure and bonding interpretation.....	42
3.4	Conclusions.....	44
3.5	References.....	45
4	Characterization of a CuInS <sub>2</sub> Monolayer Linked to FTO by Polarization Measurements and X-ray Absorption Spectroscopy.....	49
4.1	Introduction.....	49
4.2	Experimental.....	50
4.2.1	Nanocrystal Synthesis.....	50
4.2.2	Nanocrystal Monolayer and Film Deposition.....	51
4.2.3	Characterization .....	51

4.2.4	Polarization Measurements.....	52
4.3	Results and Discussions.....	53
4.3.1	CIS Monolayer Linked to FTO.....	53
4.3.2	Photoelectrochemical Measurements.....	55
4.3.3	X-ray Absorption Near-Edge Structure (XANES).....	59
4.4	Conclusion.....	68
4.5	References.....	69
5	Effect of Annealing on the Photoelectrochemical Behaviour of CuInS <sub>2</sub> Nanocrystal Films.....	73
5.1	Introduction.....	73
5.2	Experimental.....	74
5.3	Results and Discussions.....	75
5.4	Conclusion.....	85
5.5	References.....	86
6	Electrochemical Deposition of Light-absorbing CuInSe <sub>2</sub> for use in Solar Cells.....	88
6.1	Introduction.....	88
6.2	Experimental.....	89
6.2.1	CuInSe <sub>2</sub> Fabrication.....	89
6.2.2	Fabrication of Full Solar Cells.....	90
6.2.3	Characterization.....	91
6.3	Results and Discussions.....	94
6.3.1	Optimization of CISE Films.....	94
6.3.2	Composition.....	97
6.3.3	Morphology.....	98
6.3.4	Structure of the CISE Films.....	100
6.3.5	XANES of the Cu and In K-edges.....	104

6.3.6 EXAFS Cu and In K-edge .....	106
6.3.7 Solar Cell .....	114
6.4 Conclusion .....	116
6.5 References.....	117
7 Concluding Remarks and Future Outlook .....	121
7.1 Concluding Remarks.....	121
7.2 Future Work .....	123
List of Appendices .....	125
Curriculum Vitae .....	133

## List of Tables

Table 2.1 Molar Ratios for $\text{CuInS}_2$ .....	21
Table 2.2 XPS binding energy results.....	27
Table 3.1 Relative molar ratios of Cu, In, and S before and after NC synthesis .....	35
Table 5.1 Carbon and nitrogen weight percent results for the annealed films .....	81
Table 6.1 Photocurrent Ranges for different starting ratios of CISE determined from photoelectrochemical measurements .....	96
Table 6.2 Relative molar ratios of $\text{CuInSe}_2$ and $\text{CuIn(S,Se)}_2$ .....	98
Table 6.3 Major peaks from the XRD patterns, their full width at half maximum and the related crystal size.....	103
Table 6.4 EXAFS R-space spectrum results from multishell fitting procedure of CISE and CISSe .....	113

## List of Figures

Figure 1.1 Structure of a CIS photovoltaic device.....	3
Figure 1.2 Band structure of a) an i-type semiconductor b) a n-type semiconductor and c) a p-type semiconductor .....	4
Figure 1.3 The formation of a p-n junction a) before contact b) just after contact and c) The effect of light on the semiconductors and on the p-n junction.....	5
Figure 1.4 XAFS spectrum of a metal outlined with the XANES and EXAFS regions.....	9
Figure 2.1 Diagram illustration for photoelectrochemical measurements.....	15
Figure 2.2 Photoelectrochemical measurements of CIS films that used $\text{Cu}(\text{acac})_2$ as the copper source a) high photocurrent (A) in black b) low photocurrent (B) in red and films that used $\text{CuCl}_2$ as the copper sources c) high photocurrent (C) in purple and d) low photocurrent in blue (D).....	17
Figure 2.3 Mott-Schottky plots of the samples that used $\text{Cu}(\text{acac})_2$ as the sulfur source a) The high photocurrent sample and b) the low photocurrent samples. The measurements in the light are in red and in the dark are in blue. ....	19
Figure 2.4 SEM images of the samples using $\text{Cu}(\text{acac})_2$ as the copper source a) high photocurrent (A) b) low photocurrent (B) and using $\text{CuCl}_2$ as the copper source c) high photocurrent (C) and d) low photocurrent (D). The insets are the corresponding TEM images .....	23
Figure 2.5 X-ray diffraction patterns for all four samples and the standard JCPDS cards for common secondary phases .....	24
Figure 2.6 XPS results for a) Cu $2p_{3/2}$ electron binding energy (inset auger electron kinetic energy) b) In $3d_{5/2}$ electron binding energy c) S 2p binding energy .....	26
Figure 3.1a) Ternary contour plot of the starting atomic percentages of copper, indium and sulfur for CIS with respect to the PEC measurements; and b) two sample PEC	

measurements of NCs that produced high (blue, sample A whose starting composition is indicated by the circle in the ternary contour plot) and low (red, sample B whose starting composition is indicated by the rectangle in the ternary contour plot) photocurrent density. ....	34
Figure 3.2 Tauc plots of a) the high-photocurrent density sample A; and b) the low-photocurrent density sample B.....	36
Figure 3.3 XRD patterns of the high photocurrent sample (blue) and the low photocurrent sample (red). ....	37
Figure 3.4 Normalized XANES spectra in TEY mode of the sulfur K-edge for the a) high photocurrent sample A (blue), low photocurrent sample B (red), $\text{In}_2\text{S}_3$ (purple), $\text{Cu}_2\text{S}$ (green) and MPP (black). b) The first derivative of samples A and B. ....	38
Figure 3.5 Nitrogen K-edge in FY mode for the high photocurrent sample (blue), the low photocurrent sample (red) and MPP (black). ....	40
Figure 3.6 a) The S $L_{3,2}$ -edge spectra in TEY and FY modes, where “A” refers to the high photocurrent sample, “B” refers to the low photocurrent sample and the capping ligand reference in TEY, MPP, is in black for comparison. b) The first derivative spectra of samples A and B as well as MPP using the same color codes as in a). ....	42
Figure 3.7 Bulk band gap and surface conduction band gap bending for the high photocurrent sample (A); and the low photocurrent sample (B). ....	43
Figure 4.1 Experimental schematic for the angular-dependent measurements .....	53
Figure 4.2 Attachment of the linker and the $\text{CuInS}_2$ to the surface of the metal oxide via single Si – O bond (A) or multiple Si – O bonds (B). ....	54
Figure 4.3 PEC measurements in a 0.05 M $\text{MV}^{2+}$ of A) MPTMS linked FTO with $\text{CuInS}_2$ B) FTO without MPTMS after being dipped in $\text{CuInS}_2$ and C) 1-2 $\mu\text{m}$ thick $\text{CuInS}_2$ film. ....	56

Figure 4.4 Schematic demonstration of the PEC measurements of the CIS monolayer with MV <sup>2+</sup> 1) An incoming photon creates an electron hole pair in the CIS that is linked to the surface of the FTO with MPTMS; 2) The photogenerated electron reduces the methyl viologen and the photogenerated hole is filled with an electron from the FTO. ....	59
Figure 4.5 The sulfur L <sub>3,2</sub> -edge of CIS linked to FTO with the MPTMS (purple) spin coated CIS (black) and the capping ligand, 2-mercapto-5-propylpyrimidine (red).....	60
Figure 4.6 The sulfur K-edge of the CIS linked to the FTO (purple), the MPTMS linked to FTO (green) and the capping ligand 2-mercapto-5-propylpyrimidine (red) for A) TEY mode and B) FY mode * denotes a sulfate peak present in the glass substrate.....	62
Figure 4.7 Cu L <sub>3</sub> -edge measurement of bulk CIS (black) and CIS linked to FTO with MPTMS (purple) in A) TEY mode and B) FY mode.....	65
Figure 4.8 Cu L-edge FY measurements at the starting position of the angular-dependent measurement set up for a) detector 1, b) detector 2, c) detector 3, and d) detector 4.....	66
Figure 4.9 Cu L-edge FY measurements at four different angles relative to the starting sample position for angular-dependent measurements for a) detector 1, b) detector 2, c) detector 3 and d) detector 4.....	68
Figure 5.1 Photoelectrochemical measurements in 0.03 M methyl viologen of annealed CIS NCs films at a) unaltered, b) 250 °C, c) 300 °C, d) 350 °C, e) 400 °C and f) 500 °C. ....	76
Figure 5.2 IMPS at open circuit potential of a) the unaltered film and b) the film annealed at 250 °C .....	78
Figure 5.3 Thermogravimetric analysis of a) the capping ligand MPP and b) CIS .....	79
Figure 5.4 XRD of the CIS NC films a) JCPDS card No. 01-085-1575 for CIS b) unaltered, c) 250 °C, d) 300 °C, e) 400 °C, f) 500 °C. ....	80

Figure 5.5 Photoelectrochemical measurements of a) unaltered CIS (black), b) annealed CIS with a second CIS layer (blue) c) annealed CIS with a second layer of CIS annealed again (green) and d) annealed CIS (red). ..... 83

Figure 5.6 SEM images of a) unaltered CIS, b) annealed at 250 °C c) annealed at 500 °C. .... 84

Figure 5.7 Photoelectrochemical measurements of thin films of a) CIS/CdS (A)/CdS (purple), b) CIS/CdS (green), c) CIS (black), d) CIS/CdS(A) (red) where (A) denotes an annealed sample. .... 85

Figure 6.1 Photoelectrochemical measurements in 0.05 M methyl viologen of a) CuInSe<sub>2</sub> films made from a starting Cu/In ratio of 0.4 (red), 0.6 (orange), 0.8 (green), 1.0 (blue) and 1.2 (purple) and selenized with 5 mg/cm<sup>2</sup> of selenium. b) CuInSe<sub>2</sub> films fabricated with the starting ratio of 0.6 selenized with 3 (red), 5 (blue), and 10 (green) mg/cm<sup>2</sup> of selenium. c) CuInSe<sub>2</sub> film with the starting ratio of 0.6 with 5 mg/cm<sup>2</sup> of selenium and some sulfur residue on the furnace tube. .... 94

Figure 6.2 SEM images of a) CISE with a starting ratio of 0.6 and b) CISE with a starting ratio of 1.0 ..... 100

Figure 6.3 X-ray Diffraction patterns of a) CISE with a starting ratio of 0.6 b) CISE with a starting ratio of 1.0 and c) CuInSSe with a starting ratio of 0.6 and d) the planes for the three most intense chalcopyrite peaks. The peaks marked with a ▲ are the molybdenum back contact and the peaks marked with a ● are MoSe<sub>2</sub> ..... 102

Figure 6.4 XANES absorption spectra for pure phase CISE (red) and CISSe (black) a) Cu K-edge and b) In K-edge ..... 105

Figure 6.5 Cu K-edge EXAFS for pure CISE (red) and CISSe (black) a) measured k-space oscillations and b) Fourier transform spectra of the k-space spectra. The solid line is the experimental data and the dashed line is the multishell fit. The structures in the figure illustrate the atoms that contribute to the most intense peak ..... 107



Figure 6.6 Chalcopyrite structure of CISE with the following bonds circled: Cu – Se (S) in pink, Cu – In in blue, Cu – Cu in red, In – Se (S) in green and In – In in orange. .... 110

Figure 6.7 Indium K-edge EXAFS for pure CISE (red) and CISSe (black) a) measured k-space oscillations and b) Fourier transform of the k-space spectra. The solid line is the experimental data and the dashed line is the multishell fit. The structures in the figure illustrate the atoms that contribute to the most intense peak. .... 112

Figure 6.8 PEC measurement of  $\text{CuInSe}_2$  with a starting ratio of  $\text{Cu/In} = 0.6$ , selenized with  $5 \text{ mg/cm}^2$  of selenium (red) and a PEC measurement of that same film coated with CdS (blue). .... 114

Figure 6.9 The J-V curve of  $0.5 \text{ cm}^2$   $\text{CuInSe}_2$  solar cell in the light (blue) and dark (black). The inset is the current produced by the cell at 0 V and b) high efficiency J-V curve of  $0.12 \text{ cm}^2$   $\text{CuInSe}_2$  in the light (blue). .... 116

## List of Abbreviations

A	Absorption
A	Amperes
Å	Angstroms
<i>a</i>	unit cell parameter a
a.u.	arbitrary units
AC	Alternating current
acac	Acetylacetonate
Al:ZnO	Aluminium doped tin oxide
ALD	Atomic layer deposition
<i>b</i>	unit cell parameter b
B(2θ)	Full width at half maximum
BA	benzyl Alcohol
BE	Binding Energy
C	Capacitance
<i>c</i>	unit cell parameter c
CB	Conduction Band
CIGS	CuInGa(S,Se) <sub>2</sub>
CIS	CuInS <sub>2</sub>
CISe	CuInSe <sub>2</sub>
CISSe	CuIn(S,Se <sub>2</sub> )
cps	counts per second
d	d-spacing
D	Nanocrystal size
DI	Deionized
e <sup>-</sup>	electron
E	Energy
E	Potential
ECD	Electrochemical Deposition
EDX	Energy Dispersive Spectroscopy

$E_f$	Fermi Level
$E_g$	Band gap energy
$E_o$	Energy threshold
eV	Electron volts
EXAFS	Extended X-ray absorption fine structure
F	Farad
FT	Fourier Transform
FTO	Fluorine doped tin oxide
FY	Fluorescence yield
g	gram
h	Plank's constant
$h^+$	hole
Hz	Hertz
IMPS	Intensity Modulated Photocurrent Spectroscopy
$I_o$	Incident photon flux
$I_{sc}$	Short circuit current
ITO	Indium doped Tin Oxide
$j$	photocurrent
JCPDS	Joint Committee on Powder Diffraction Standards
k	momentum space wavenumber
$k_d$	Rate of Decay
$k_{et}$	Rate of electron transfer
$k_{ps}$	Rate of product separation
$k_r$	Rate of Recombination
LED	Light Emitting Diode
M	Molarity
$m_e$	mass of an electron
MPP	2-mercapto-5-propylpyrimidine
MPTMS	(3-mercaptopropyl)trimethoxysilane
$MV^{2+}$	Methyl Viologen
NC	Nanocrystals

OLA	Oleyamine
PEC	Photoelectrochemical
PET	polyethylene terephthalate
r	distance
rad	radian
SCE	Saturated Calomel Electrode
SCR	Space Charge Region
SEM	Scanning Electron Microscopy
SGM	Spherical grating monochromater
SR	Synchrotron Radiation
SXRMB	Soft X-ray microcharacterization beamline
TEM	Transmission Electron Microscopy
TEY	Total electron yield
TGA	Thermogravimetric Analysis
TWh	Terra Watt hour
UV	Ultra violet
V	Volt
VB	Valence Band
Vis	visible radiation
VLS-PGM	Variable line space plane grating monochromater
V <sub>oc</sub>	Open Circuit Potential
XAFS	X-ray absorption fine structure
XANES	X-ray Near Edge Absorption Fine Structure
XPS	X-ray Photoelectron Spectroscopy
XRD	X-ray Diffraction
$\alpha$	Absorption Coefficient
$\lambda$	Wavelength
$\nu$	photon frequency
$\phi(k)$	phase shift function
$\theta$	Bragg Angle

# 1 Introduction

The global demand for energy has been projected to increase as much as 48% in the next 20 years,<sup>1</sup> and the world needs to find a way to meet this demand that is sustainable.

Fossil fuels are one of the most widely available and cheapest sources of energy.

However, the major problem with fossil fuels is the CO<sub>2</sub> emissions and greenhouse gases that are produced in both their refinement and use, which destroy the ozone layer and are one of the main causes of global warming.<sup>2,3</sup> Estimates have the CO<sub>2</sub> emissions at approximately 5 tonnes per capita worldwide in 2014.<sup>4</sup> This causes severe effects on the environment, but is still potentially reversible as long as these environmental hazards are reduced, and ideally stopped from production.

Another source of concern is that oil, coal, and natural gas are the main sources of energy currently used worldwide, but are finite resources. Projections for each of the reserves to run out are as early as 50 years, 70 years, and 250 years, respectively, for oil, natural gas, and coal.<sup>5</sup> We, as a society, must shift away from fossil fuel as a source of energy in the long term.

Alternative sources of energy are becoming more and more popular, and sources such as nuclear, hydro, and wind are being utilized everywhere now, especially in Canada. While each of these technologies are excellent in their own right, they too have their own pitfalls. Much more research needs to be done for safer and more inexpensive disposal solutions for nuclear hazardous waste. Hydroelectric energy requires building dams, and the resultant flooding destroys habitats for many flora and fauna. Wind requires building and maintaining incredibly large turbines, which are extremely costly. Combined with the fact that these energy sources are not always an option for people in some areas of the world, suggests that a renewable source with global availability is needed.

Solar energy is an abundant, free source of energy that requires no mining or combustion to obtain. Approximately 885 million TWh from the sun reach the surface of Earth every year, which is thousands of times more than humans consume in that same timespan.<sup>6</sup>

What is required is a method of harnessing solar energy into usable electricity. This can be accomplished through the use of photovoltaic devices or solar cells. These devices

can convert sunlight to electricity without substantial mechanical movement, and they can be placed anywhere the energy is needed.

## 1.1 Solar Cell Generations

There are three generations of photovoltaic devices encompassing several different methodologies for the generation and capture of the photogenerated electron hole pair. The first generation is crystalline wafer silicon solar cells. This technology is the oldest, having reached efficiencies of over 20 %, <sup>7</sup> and is already used commercially. First generation solar cells needed a relatively large amount (10  $\mu\text{m}$ ) of highly crystalline Si, which, up until recently, was costly to produce. To combat the amount and purity of silicon needed, second generation solar cells were developed. The second generation is single junction, thin-film inorganic solar cells. These photovoltaic devices are the answer to the excess material problem found in the Si-based devices. The absorber layer is typically 1 to 2  $\mu\text{m}$  thick using considerably less material than the first generation alternatives. A few examples of this generation include CdTe, CuInGa(S,Se)<sub>2</sub> (CIGS) CuInSe<sub>2</sub> (CISe) and CuInS<sub>2</sub> (CIS). Finally, the third generation solar cells are attempting to compensate for the Shockley-Queisser limit for single junction photovoltaics. <sup>8</sup> The Shockley-Queisser limit uses various assumptions to find the maximum theoretical efficiency of 30% for a single p-n junction photovoltaic device. <sup>8</sup> Examples of this generation include tandem p-n junction solar cells, multi-exciton quantum dot technology, and perovskite solar cells. <sup>8</sup> These technologies are still in the developmental stages, and have a variety of issues to overcome before they can be successfully commercialized.

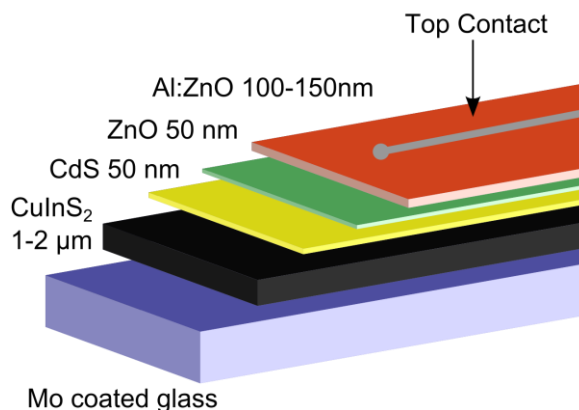


**Figure 1.1 Structure of a CIS photovoltaic device.**

CIGS solar cells have efficiencies that are already high enough to commercialize; upwards of 20%.<sup>7</sup> What is preventing the widespread commercialization of these materials is their cost. Gallium is a relatively rare element which drives up their price. There is an alternative: the gallium can be removed from CIGS to produce CIS or CISE, which can dramatically reduce the cost.

Second generation solar cells have a relatively simple structure; an example of which is shown in Figure 1.1. The back contact is often indium-doped tin oxide (ITO), fluorine-doped tin oxide (FTO), or molybdenum-coated soda lime glass. CIS or CISE is the light-absorbing layer, and CdS is an n-type buffer layer that provides a photocurrent enhancement due to band matching. The aluminum doped zinc oxide (Al:ZnO) and zinc oxide layers are n-type window layers that do not absorb in the solar spectrum, and create the p-n junction.

## 1.2 $\text{CuInS}_2$ and $\text{CuInSe}_2$

CIS and CISE have direct band gaps of 1.4 to 1.5 eV and 1.0 eV respectively, and high absorption coefficients of  $10^4 - 10^5 \text{ cm}^{-1}$ ,<sup>9,10</sup> making them ideal for use in solar cells. Copper, indium, and sulfur are all relatively non-toxic, and – with the exception of indium – inexpensive and earth-abundant elements. Although indium is not globally available, one of the major indium deposits is present in Canada.<sup>11</sup> While indium is a relatively expensive element, the laboratory efficiencies of CIS and CISE incorporated

into a full device are high enough to compensate for the increased cost from the use of indium. The record efficiencies of CIS and CISE based solar cells are currently 12.5% and 15 % respectively.<sup>12, 13</sup> The techniques used to achieve high efficiencies, however, use toxic conditions such as  $H_2S$ ,<sup>14</sup> hydrazine,<sup>15, 16</sup> or KCN;<sup>12</sup> and high-cost techniques that require vacuum systems<sup>17</sup> or high temperatures.<sup>14</sup> These methods are prohibitive for the commercialization as they are both costly and dangerous.

### 1.3 Semiconductors

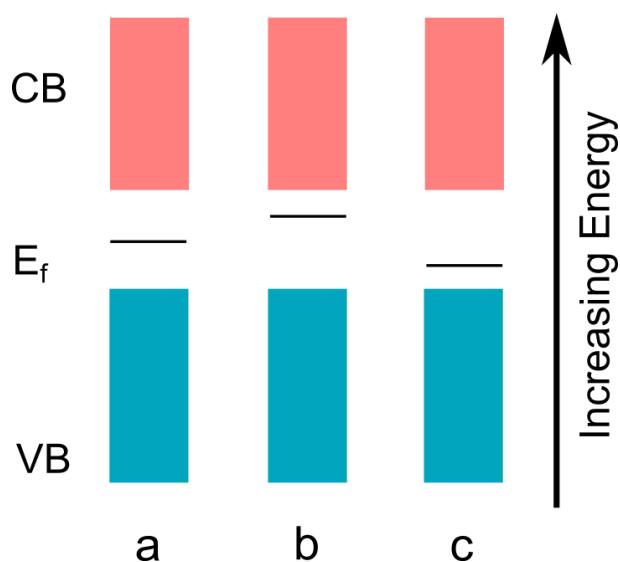


**Figure 1.2 Band structure of a) an i-type semiconductor b) a n-type semiconductor and c) a p-type semiconductor**

Solar cells work through the use of semiconductors. A semiconductor has a conductivity between a metal and an insulator. In a single atom or molecule the energy levels are discrete. In a solid, however, the abundance of energy levels forms bands. The electron filled band is termed the valence band (VB), and the unfilled band is the conduction band (CB). This concept can be used to explain conductors, insulators, and semiconductors. In a conductor, the VB and CB overlap and thus the electron can move freely. An insulator has a large band gap energy ( $E_g$ ) between the VB and CB such that, for an electron to move from the VB to the CB, a large amount of energy is required. A semiconductor has a smaller  $E_g$ , so that a smaller input of energy – be it thermal or photonic – can excite an electron and allow current to pass through the material.



There are three types of semiconductors: intrinsic or *i*-type, p-type and n-type. A representation of each is shown in Figure 1.2a), the VB and CB have a small enough gap between them that electrons can be promoted with a small amount of energy. The fermi level ( $E_f$ ) falls right between the VB and CB. The other types of semiconductors involve introducing a level in the band gap region via doping. The n-type semiconductor (Figure 1.2b) is electron rich, meaning there is a level just below the conduction band into which electrons can move. This moves the  $E_f$  closer to the CB, and introduces an energy level in the band gap region just below the CB. A p-type semiconductor (Figure 1.2c) is an electron-poor semiconductor which introduces an energy level just above the VB and moves the  $E_f$  closer to the VB. The extra energy levels make it easier for the promotion of the electrons, as less energy is needed.

## 1.4 p-n Junction

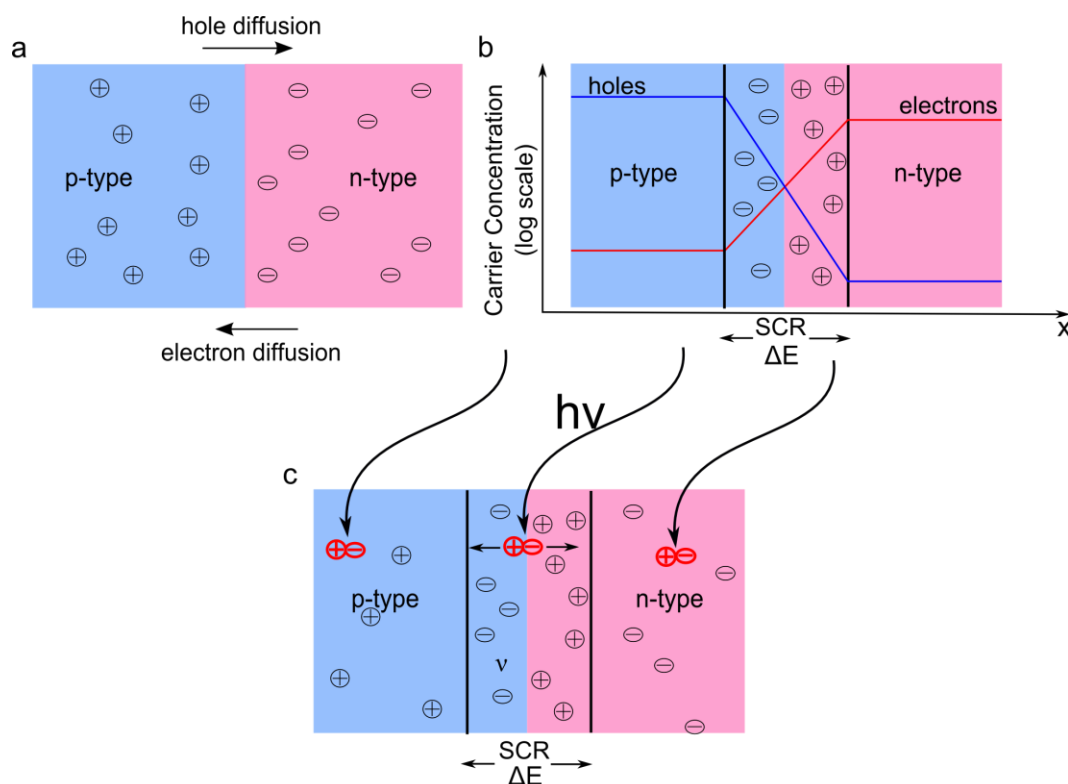


**Figure 1.3 The formation of a p-n junction a) before contact b) just after contact and c) The effect of light on the semiconductors and on the p-n junction**

A semiconductor alone is only the first step in harnessing the sun's energy. A p-n junction needs to be created as the first step of creating a photovoltaic device. It involves a p-type semiconductor being brought into contact with an n-type semiconductor (Figure 1.3a). When the two are in contact, the electron rich n-type semiconductor's electrons diffuse across to the p-type semiconductor at the surface (Figure 1.3b) leaving holes at the interface of the n-type semiconductor. At the interface, the p-type is electron rich, and the n-type is electron-poor, which continues up to a certain depth in both films. This area across both films is called the space charge region (SCR) (Figure 1.3b). This diffusion of electrons and holes across the interface continues until equilibrium is reached. At this point there is an internal potential.

When a photon hits the semiconductors electron hole pairs are generated (Figure 1.3c, shown in red). If the photogenerated electron hole pair occurs in the bulk of the p- or n-type semiconductors they will immediately recombine. If the photogenerated electron hole pair occurs in the SCR the internal bias causes the electron to move toward the n-type side, and the hole to move toward the p-type side, which is shown with arrows in Figure 1.3c.

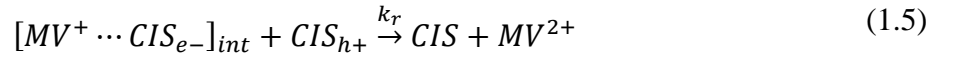
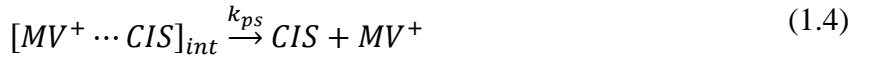
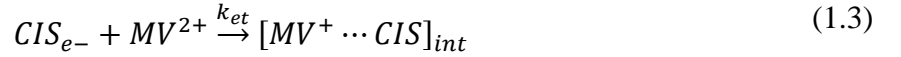
Finally the electrons can be extracted using an external bias in the reverse direction. Note that an external bias in the forward direction (anode connected to the p-type and cathode connected to the n-type) pushes electrons toward the interface, while an external bias in the reverse direction pushes electrons away from the interface. A reverse bias is more useful for solar cell applications as the photogenerated electron hole pair created in the SCR needs to be separated or pulled away from the interface.

## 1.5 Tools for Characterization

### 1.5.1 Photoelectrochemical Measurement

The optimization of the CIS, and CISE layers is the most important aspect of this work. However, building a full device after every small change to the light-absorbing film can be time-consuming and costly. Photoelectrochemical (PEC) measurements allow for the light-absorbing CIS film to be photoelectrochemically characterized without the full device fabrication. PEC measurements utilize methyl viologen ( $MV^{2+}$ ) in an aqueous

system.<sup>18</sup> The CIS film is plated on a conductive back contact and used as the working electrode. Under illumination the CIS reduces the  $MV^{2+}$  to  $MV^+$  following equations 1.1 to 1.5.



The incoming photon creates an electron hole pair (equation 1.1). The pair can then either decay (equation 1.2) or transfer the electron to the  $MV^{2+}$  (equation 1.3). The transfer forms an intermediate species where the  $MV^+$  is associated with the CIS. This intermediate can then separate into  $MV^+$  and CIS, and current can flow; or the electron associated with the  $MV^+$  can recombine with a hole from the CIS film, and no current is produced from the excitation.

### 1.5.2 Conventional Characterization

A variety of techniques and instrumentation were utilized to gather compositional, structural, and morphological information about CIS and CISE. The theory behind these techniques will be briefly discussed here.

Scanning electron microscopy (SEM) involves probing the material with a focused electron beam. As the beam of electrons scans the surface of the material several processes occur some of which include: backscattered electrons, Auger electrons, and X-ray fluorescence.<sup>19</sup> The backscattered and secondary electrons are used to create the image of the surface which gives topological information. The X-rays emitted from the

material in question can also be collected for qualitative and quantitative purposes. This bulk-sensitive technique is termed energy dispersive X-ray spectroscopy (EDX).<sup>19</sup>

When an X-ray passes through matter it interacts with the electron clouds surrounding each atom. The wavelengths of X-rays are comparable to that of the separation between the atoms, constructive and destructive interference occurs. The X-rays are scattered, but only those with constructive interference (or beams that are in phase) are observed.<sup>19</sup>

This means that the spacing between the layers of atoms must be similar to the incident X-ray wavelength, and the atoms are oriented in a highly regular way. X-ray diffraction (XRD) relates the pattern produced from this X-ray scattering to the structure of the crystal. This is accomplished through the use of Bragg's law<sup>19</sup> shown in equation (1.6).

$$\lambda = 2d\sin\theta \quad (1.6)$$

Where  $\lambda$  is the incident wavelength,  $d$  is the spacing between the planes of atoms and  $\theta$  is the Bragg angle. For each plane, defined by the miller indices  $h$ ,  $k$ , and  $l$ , the Bragg angle is unique and manifests as a peak in the diffractogram. Thus the structure, crystallinity and size of the crystals in the system can be determined.

X-ray photoelectron spectroscopy involves measuring the kinetic energy ( $E_k$ ) of the resulting photoelectrons after a material is exposed to an X-ray source. The binding energy of that photoelectron is determined based on equation (1.7)<sup>19</sup>:

$$E_b = h\nu - E_k - w$$

Where  $E_b$  is the binding energy,  $h\nu$  is the energy of the incoming photon, and  $w$  is the work function. The binding energy is characteristic of a specific atom in a specific oxidation state. This measurement allowed for the oxidation states of the atoms in the materials to be probed as well as their surface composition.

### 1.5.3 Synchrotron Radiation

Synchrotron Radiation (SR) is a specific type of radiation that is produced by accelerating electrons to near the speed of light and then using a magnetic field to change their trajectory, which causes them to emit electromagnetic radiation.<sup>20</sup> SR is highly

collimated, and can be used to determine significant information about a material. X-ray absorption spectroscopy fine structure (XAFS) is the measure of the absorption coefficient of a material at specific energies.<sup>21</sup> It is similar to UV-vis spectroscopy, except that instead of an excitation from ground state to an excited state, XAFS involves the ejection of a core electron.<sup>22</sup> It can be broken down into X-ray absorption near edge structure (XANES), which probes the near edge region of a core level of a specific element and extended X-ray absorption fine structure (EXAFS), which probes the local geometric structure surrounding the element of interest.<sup>21, 23, 24</sup> These two ranges of a typically metal spectra are shown in Figure 1.4 . XANES is defined as the region directly around the absorption edge, including pre-edge features and EXAFS begins at the first oscillation of the post edge.<sup>21</sup>

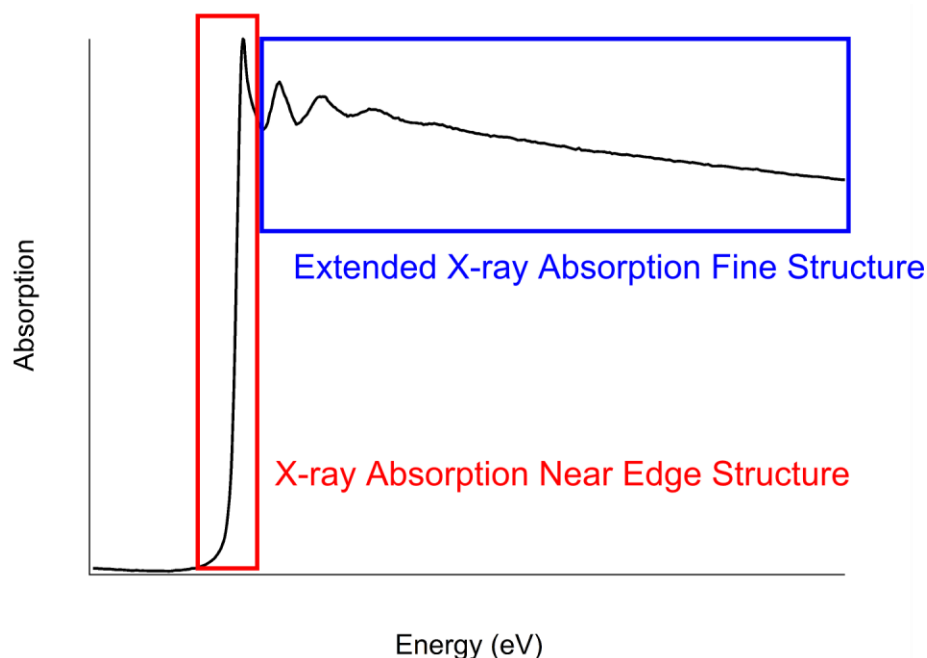


**Figure 1.4 XAFS spectrum of a metal outlined with the XANES and EXAFS regions.**

XANES measurements typically involve a pre-edge region, the region right before the large jump in the absorption coefficient, and the large increase in the absorption coefficient termed the “white line” which occurs at  $E_0$ . Each element has its own specific core electron excitation energy and as such this technique can determine which elements

are present. The pre-edge probes the transitions of the excited electrons into empty orbitals spin-forbidden transitions are changes in this spectrum reflect changes in local geometry, oxidation state and bonding.<sup>21</sup> The energy at which the absorption white line appears is also indicative of oxidation state and involves spin-allowed transitions.<sup>21</sup> As such XANES can be used to determine site specificity, interfacial interactions, and the local chemical environment of the absorbing atom.<sup>23</sup> Its high sensitivity to these and other aspects of the material are why it was chosen for characterization of the CIS and CISE.

## 1.6 Scope of Thesis

This work focuses on a layer-by-layer optimization of CIS and CISE solar cells using low-cost methods. The cost associated with the fabrication of these solar cell devices to achieve a high efficiency is what is preventing them from commercialization. If the associated costs can be lowered then this technology could be of great use in shifting energy use towards becoming renewable and environmentally friendly.

The deposition and fabrication of the CIS and CISE is the most expensive part of the process. In this work, two different methods of light-absorbing layer fabrication and deposition will be explored. The first is a facile one-pot synthesis of CIS nanocrystals (NCs) optimized in Chapter 2. This technique uses low temperatures and non-toxic solvents. The resultant product was fully characterized both in Chapter 2 by conventional means, and in Chapter 3 by synchrotron radiation, to not only investigate the presence of secondary phases, but also to obtain information about the connectivity of the capping ligand, and the position of the conduction band. Chapter 4 describes a novel method of attaching the NCs formed from the one-pot synthesis to the back contact. A linker molecule, (3-mercaptopropyl)trimethoxysilane (MPTMS), was used to chemically adhere the NCs to a metal oxide back contact via bond through the silane end of the molecule and the thiol group on the opposing end. This created a monolayer of CIS NCs over the surface of the back contact that, when tested with PEC measurements, produced a similar photocurrent density to much thicker films of CIS NCs. Chapter 5 explores the second method of light-absorbing layer fabrication. Electrochemical deposition (ECD) of the

copper and indium followed by a selenization to form CISE is the focus of this chapter. ECD is a low cost process that is already carried out on an industrial scale.

Finally, in Chapter 6 the optimization of the next layer, CdS, is performed for the NCs. A low-temperature annealing process provided photocurrent enhancement that will ultimately benefit the full devices. In the final chapter a summation of all the findings of this project will be given.

## 1.7 References

- (1) Conti, J.; Holtberg, P.; Diefenderfer, J.; LaRose, A.; Conti, J.; Turnure, J. T.; Westfall, L. *International Energy Outlook 2016*; Independent Statistics & Analysis U.S. Energy Information Administration: 2016.
- (2) Is There a Connection between the Ozone Hole and Global Warming? [http://www.ucsusa.org/global\\_warming/science\\_and\\_impacts/science/ozone-hole-and-gw-faq.html](http://www.ucsusa.org/global_warming/science_and_impacts/science/ozone-hole-and-gw-faq.html) (accessed June 27th 2017).
- (3) A Blanket Around the Earth. <https://climate.nasa.gov/causes/> (accessed June 27, 2017).
- (4) Olivier, J. G. J.; Janssens-Maenhout, G.; Muntean, M.; Peters, J. A. H. W. *Trends in global CO<sub>2</sub> emissions; 2014 Report*; The Hague, 2014.
- (5) Greene, D. L.; Hopson, J. L.; Li, J.; *Energy Policy* **2006**, *34*, 515-531.
- (6) Philibert, C. *Technology Roadmap Solar Photovoltaic Energy*; International Energy Agency: Paris, 2014.
- (7) Green, M. A.; Emery, K.; Hishikawa, Y.; Warta, W.; Dunlop, E. D.; *Prog. Photovolt: Res. Appl.* **2015**, *23*, 1-9.
- (8) Conibeer, G.; *Mater. Today* **2007**, *10*, 42-50.
- (9) Tuttle, J.; Goral, D. A.; Kennedy, C.; Noufi, R.; *Solar Cells* **1988**, *24*, 67-79.
- (10) Scheer, R.; *Prog. Photovolt: Res. Appl.* **2012**, *20*, 507-511.
- (11) Lokanc, M.; Eggert, R.; Redlinger, M. *The Availability of Indium: The Present, Medium Term and Long Term*; National Renewable Energy Laboratory: Golden, Colorado, 2015.
- (12) Klaer, J.; Bruns, J.; Henninger, R.; Töpper, K.; Klenk, R.; Ellmer, K.; Bräunig, D.; 2nd World Conference and Exhibition on Photovoltaic Solar Energy Conversion, Luxembourg, Schmid, J., Ossenbrink, H. A., Helm, P., Ehmann, H. and Dunlop, E. D., Eds. Joint Research Center: Luxembourg, 1998; pp 537-540.

- (13) AbuShama, J., A. M.; Johnston, S.; Moriarty, T.; Teeter, G.; Ramanathan, K.; Noufi, R.; *Prog. Photovolt: Res. Appl.* **2004**, *12*, 39-45.
- (14) Lee, S. M.; Ikeda, S.; Yagi, T.; Harada, T.; Ennaoui, A.; Matsumura, M.; *Phys. Chem. Chem. Phys.* **2011**, *13*, 6662-6669.
- (15) Liu, W.; Mitzi, D. B.; Yuan, M.; Kellock, A. J.; Chey, S. J.; Gunawan, O.; *Chem. Mater.* **2010**, *22*, 1010-1014.
- (16) Hou, W. W.; Bob, B.; Li, S.-h.; Yang, Y.; *Thin Solid Films* **2009**, *517*, 6853-6856.
- (17) Schneider, N.; Bouttemy, M.; Genevée, P.; Lincot, D.; Donsanti, F.; *Nanotechnology* **2015**, *26*, 054001.
- (18) Ye, H.; Park, H. S.; Akhavan, V. A.; Goodfellow, B. W.; Panthani, M. G.; Korgel, B. A.; Bard, A. J.; *J. Phys. Chem. C* **2011**, *115*, 234-240.
- (19) Skoog, D. A.; Holler, F. J.; Crouch, S. R., *Principles of Instrumental Analysis Sixth Edition*. Brooks/Cole: Belmont, CA, 2007.
- (20) Willmott, P., *An Introduction to Synchrotron Radiation: Techniques and Applications*. John Wiley & Sons: West Sussex, 2011.
- (21) Liu, X.; Weng, T.-C.; *MRS Bull.* **2016**, *41*, 466-472.
- (22) Zhang, P.; *J. Phys. Chem. C* **2014**, *118*, 25291-25299.
- (23) Sham, T. K.; *Adv. Mater.* **2014**, *26*, 7896-7901.
- (24) Mobilio, S.; Boscherini, F.; Meneghini, C., *Synchrotron Radiation Basics, Methods and Applications*. Springer: 2015.



## 2 Preparation and Characterization of CuInS<sub>2</sub> Nanocrystals for Photovoltaic Materials

(A version of this work is presented in Physical Chemistry Chemical Physics. Tapley, A.; Vaccarello, D.; Hedges, J.; Jia, F.; Love, D. A.; Ding, Z.; *Phys. Chem. Chem. Phys.* **2013**, *15*, 1431-1436.)

### 2.1 Introduction

Solar energy is a readily abundant free source of energy that has great potential to be a solution to the world's energy crisis. Thin film solar cells are one of the attractive protocols for harnessing this energy. An example of a thin film solar cell is that of Cu(In,Ga)Se<sub>2</sub> (CIGS),<sup>1,2</sup> which has shown a laboratory efficiency up to 20%.<sup>3</sup> Unfortunately, gallium and selenium are expensive, dangerous, and gallium is difficult to handle; so although this material shows high efficiency, it is not a good candidate for low-cost, low-environmental-impact production of solar cells. The removal of gallium and selenium yields CuInS<sub>2</sub> (CIS). CIS shows great potential to replace CIGS and silicon based solar cells with laboratory efficiencies up to 9.5%.<sup>4</sup> Drawbacks of this solution include the cost associated with the production of this material, as well as the environmental impact of the synthesis.<sup>5</sup> Current methods of preparing the light-absorbing layer involve vacuum deposition<sup>6</sup> and high temperature annealing in a sulfur or selenium atmosphere.<sup>4,5,7</sup> The removal of these steps is important to bring the cost and impact to the environment down. Only a few reports have appeared for alternative fabrication methods such as electrochemical processes, particulate processes, nanoparticle inks, and phase changing materials to the photovoltaic ones via solid state reactions.<sup>8-14</sup> Most of these methods still needed high-temperature annealing.

Herein we report a one-pot synthesis at low temperatures and without the annealing step where CIS nanocrystals (NCs) were prepared. Optimization of the initial stoichiometry was conducted based on a photoelectrochemical (PEC) measurement at interfaces between NC films deposited on indium-doped tin oxide (ITO) and 0.1 M methyl viologen dichloride (MV<sup>2+</sup>) solution. This method allowed for a quick and relatively easy approach

of testing the photoconversion of the NCs relative to each other without the preparation of a full device.<sup>7</sup> Mott-Schottky and UV-Vis absorption experiments were used to investigate the photovoltaic properties and absorption coefficient of the NCs. The NCs were investigated using energy dispersive X-ray spectroscopy (EDX) for the bulk samples and X-ray photoelectron spectroscopy (XPS) as a more surface sensitive approach. Morphology and size were examined using scanning electron microscopy (SEM) and transmission electron microscopy (TEM). Finally, the crystal structure was measured using powder X-ray diffraction (XRD). The CIS molar ratio and reagents were identified as yielding NCs with great potential for a light-absorbing layer in solar cells. With the subsequent characterization, the factors that affect the quality of the absorbing layer were explored.

## 2.2 Experimental

$\text{CuCl}_2 \cdot \text{H}_2\text{O}$  (Sigma-Aldrich 99.0%), copper(II) acetylacetonate ( $\text{Cu}(\text{acac})_2$ , Aldrich Chemistry 97% ), and indium (III) acetylacetonate (Aldrich chemistry 99.99%) were used as the metal sources. The copper and the indium salts were placed in benzyl alcohol (BA, Sigma-Aldrich, 99.8%) in varying ratios. They were dissolved in the BA at approximately 160 °C for two minutes. Then 20 mg of 2-mercapto-5-propylpyrimidine (MPP, Alfa Aesar 98%) was added in combination with a thiourea (Fluka 99.0%) solution in BA at a concentration of 0.2 M. The vial was then heated to 180 °C for 10 minutes in a silicone oil bath. The resulting solution was allowed to cool to room temperature, and the NCs were centrifuged using a Thermo Scientific Sorveall Legend Micro 21 centrifuge at 12,000 g for 6 minutes. The supernatant was discarded and the NCs were dispersed in 1 mL of acetone using a 1510 Branson Sonicator at 42 kHz. The NCs were centrifuged again, the supernatant was discarded, and they were left to dry overnight.

### 2.2.1 Characterization

The quality of the NCs was tested using PEC experiments based on a previous method (shown in Figure 2.1) reported by Ye et al.<sup>7</sup> The as-prepared NCs were dispersed in acetone at a concentration of 20 g/L, and two 6  $\mu\text{L}$  drops were drop cast onto a masked

surface area of  $0.1 \text{ cm}^2$  on a cleaned ITO-coated polyethylene terephthalate (PET) plate (Aldrich, Mississauga, ON). The plate was then submerged in a  $0.1 \text{ M MV}^{2+}$ , (Aldrich Chemicals 98%) and  $0.1 \text{ M KCl}$  (Sigma-Aldrich 99.0%) solution. A saturated calomel electrode (SCE) and a platinum coil were used as the reference and counter electrodes, respectively. The electrochemical cell was placed in front of a 150 W Newport lamp with an AM 1.5D filter. Between the light source and the cell was a shutter that operated at 0.333 Hz for light on and off switching (Figure 2.1). A linear voltage sweep was applied between 0 and  $-0.4 \text{ V}$  at a scan rate of  $5 \text{ mV/s}$  using an Electrochemical Analyzer (CH Instruments, Austin TX).

Mott-Schottky plots were obtained with the same electrochemical setup as in the PEC measurements. Instead of the shutter, the sample was kept in the dark and illuminated in two separate experiments. The ac frequency applied was  $1 \text{ kHz}$  over the same potential range used in the PEC measurement.

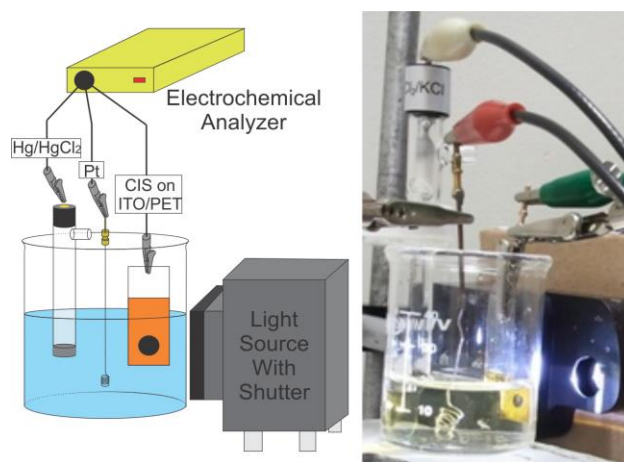


**Figure 2.1 Diagram illustration for photoelectrochemical measurements.**

The SEM was performed using a Hitachi S-4500 field emission electron microscope with a Quartz XOne EDX system at Surface Science Western. The TEM was carried out on a Philips CM 10 transmission electron microscope at The Biotron Institute for Experimental Climate Change Research at Western. XRD spectra were obtained using an Inel CPS Powder Diffractometer with a Cu X-ray radiation (Inel XRG 3000) generator,

and an Inel CPS 120 detector. The XPS was investigated using a Kratos AXIS Nova Spectrometer using a monochromatic Al K $\alpha$  X-ray source.

## 2.3 *Results and Discussions*

### 2.3.1 Synthesis

The metal and sulfur sources were varied to find the recipe that produces NCs with the largest current density based on the PEC measurement. Two different copper salts were utilized separately while keeping the indium (III) acetylacetonate constant. Indium was varied from approximately 0.5-2.5 molar equivalents relative to copper. Thiourea was used as a sulfur source due to the poor solubility of sulfur in BA, and it was varied from 0.5 to 4 molar equivalents relative to copper. When thiourea is heated to 180 °C or above, hydrogen sulfide is produced.<sup>15</sup> H<sub>2</sub>S can not only reduce copper, but it can also react with it to form copper sulfides. H<sub>2</sub>S can also combine to In(III) to form In<sub>2</sub>S<sub>3</sub>. This makes it a better candidate for this synthetic strategy than elemental sulfur. A potential issue can arise from forming copper and indium sulfide subphases that inhibit the ability of the material to produce a current. Their presence can be tested using XRD.

The one-pot synthesis was done at a relatively low temperature using a short capping ligand: MPP. Previous studies often used oleylamines to stabilize the NCs.<sup>7, 16</sup> MPP has been used previously to stabilize copper clusters.<sup>17</sup> It was found that this capping ligand gave better quality NCs based on the PEC measurements. This could be attributed to the delocalization of electron density on the pyridimine ring facilitating electron transfer when the NCs are exposed to light. MPP also contains a sulfur atom which potentially incorporates into the CIS crystal structure. This is especially likely, as in this synthesis no excessively high temperatures are used to burn out the organic components of the NCs.

### 2.3.2 Photoelectrochemical Measurements

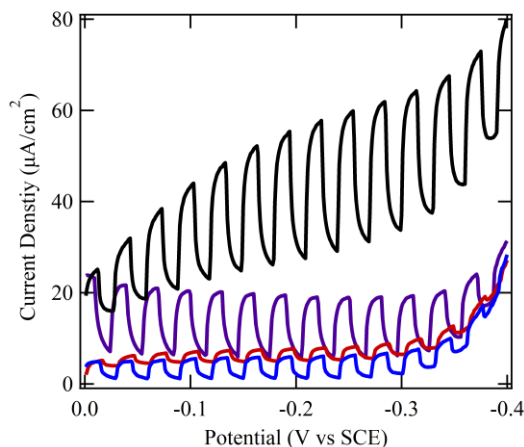


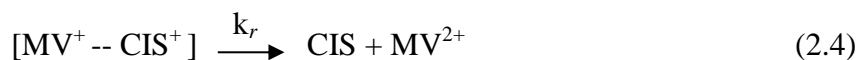
**Figure 2.2 Photoelectrochemical measurements of CIS films that used  $\text{Cu}(\text{acac})_2$  as the copper source a) high photocurrent (A) in black b) low photocurrent (B) in red and films that used  $\text{CuCl}_2$  as the copper sources c) high photocurrent (C) in purple and d) low photocurrent in blue (D)**

The typical PEC measurements are shown in Figure 2.2 and illustrate a contrast between NCs with a relatively large current density, samples A and C, and ones with lower responses to photons, samples B and D. These samples were chosen so the differences between NCs that did and did not demonstrate a large photoresponse could be investigated. A and B used  $\text{Cu}(\text{acac})_2$  as the copper source, while C and D used  $\text{CuCl}_2$ . The current densities ranges were between 12.8 and 27.9  $\mu\text{A}/\text{cm}^2$  for A, 1.21 and 2.88  $\mu\text{A}/\text{cm}^2$  for B, 9.18 and 13.6  $\mu\text{A}/\text{cm}^2$  for C, and 3.32 and 7.36 for D. If just the highest photocurrent densities are considered the following observations can be made: sample A is almost an order of magnitude larger than B, sample C is only about two times larger than D, and finally sample A had a density approximately two times larger than of sample C.

The CIS NCs that used  $\text{CuCl}_2$  as the copper source would often show current densities higher than that of the  $\text{Cu}(\text{acac})_2$  samples. This is not reflected in the PEC measurements in Figure 2.1, however, because the samples that used  $\text{CuCl}_2$  were not as reproducible as those synthesized from  $\text{Cu}(\text{acac})_2$ . The lack of reproducibility from the  $\text{CuCl}_2$  samples may be due to  $\text{CuCl}$  present in the flask. CIS formed directly from  $\text{Cu}(\text{I})$  is electrically

resistive leading to an inconsistent photocurrent. This agrees well with the results reported by Messaoudi et al<sup>18</sup> on the preparation of CIS using a spray pyrolysis method.

A small slope in all of the PEC measurements suggests lower resistive properties within the film. The rises and falls in photocurrent can be explained by looking at the kinetics of interfacial photoreactions. The following reactions are what occurred when light hit the samples. This is similar to the case at a semiconductor electrode/electrolyte<sup>19-22</sup> or liquid/liquid interface, where a photosensitizer is adsorbed at the interface and the redox couple stays in the organic phase.<sup>23, 24</sup>



The initial excitation of the light-absorbing layer is shown in equation 2.1. The excited state can either decay back to its original state (equation 2.2) or react with the  $\text{MV}^{2+}$  to form an intermediate species via electron transfer (equation 2.3). The charges in the intermediate state can then either recombine (equation 2.4) at a rate of  $k_r$ , or separate (equation 2.5) at the rate of  $k_{ps}$ .<sup>23</sup> When the NCs were illuminated, an increase in photocurrent was seen. After the initial response, a gradual increase in the current density was observed until the shutter closed. Upon removal of the light, the photocurrent sharply decreased to a certain point before tapering off. The large increase in current in samples A and C suggests a greater concentration of charge carriers. The gradual rise and fall in photocurrent upon illumination and light-off for all the four samples indicates that  $k_{ps} > k_r$ .<sup>23</sup> This observation is very similar to that of photocurrents enhanced by a gold nanoparticle film at polarized interfaces formed by porphyrin in organic phase and ferrocene in water.<sup>23</sup>

The gradual increase in photocurrent in samples A and C during illumination, after the initial current spike, might be caused by the excited states at the absorbing layer/solution interface that have reached the concentration limit to react with  $MV^{2+}$  in excess. In any case,  $k_r$  is small for all the samples, since photocurrent decay was not observed during the illumination. In the case where  $k_r$  is larger, a sharp increase followed by decay in the current would be observed. Very interestingly, when the light is off, the feature of a negative overshoot in the current before returning to zero<sup>23</sup> is absent from the obtained transients. Instead, a gradual decrease in the photocurrent is observed. These very interesting observations implicate the diffusion of the excited states (though minor upon illumination) to the absorbing layer surface and their reaction with  $MV^{2+}$  (equation 2.3) to generate the positive current compensating for the expected negative current caused by the recombination (equation 2.4). This result is very similar to that obtained by Schaming et al. for their photoelectrochemical system at a liquid/liquid interface covered with Au nanoparticles.<sup>23</sup> The as-prepared NC films are very favourable for photovoltaic applications. While photocurrent generated by samples B, C and D are independent of applied voltage, A displayed the highest current in the potential range between -0.2 and -0.4 V.

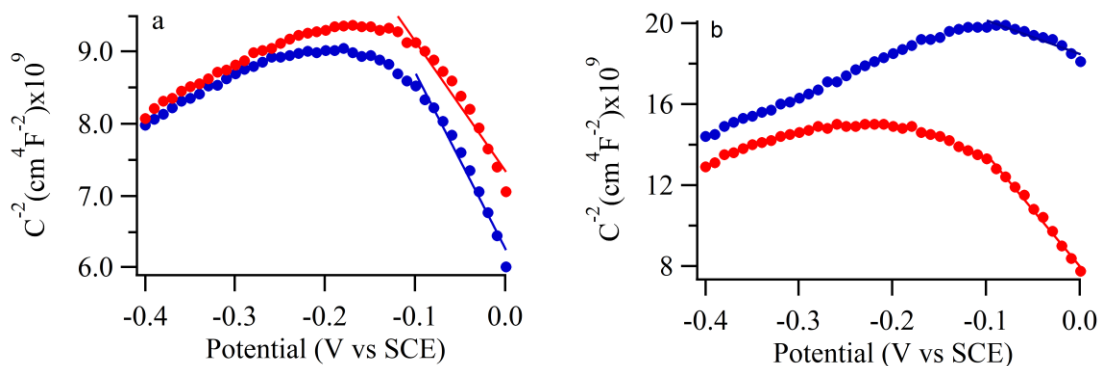


**Figure 2.3 Mott-Schottky plots of the samples that used  $Cu(acac)_2$  as the sulfur source a) The high photocurrent sample and b) the low photocurrent samples. The measurements in the light are in red and in the dark are in blue.**

Figure 2.3 displays the results of the Mott-Schottky experiments that were performed on the overall best (Figure 2.3a, sample A) and overall worst (Figure 2.3b, sample B) samples.

The linear section of the plots indicates a space charge region in the materials, and the negative slope of the line indicates that a p-type semiconducting material was obtained.<sup>25</sup> The slope of the line is inversely proportional to the acceptor concentration ( $N_A$ ), which has been calculated at  $8.65 \times 10^{20}$ ,  $1.18 \times 10^{21}$  for sample A and  $1.26 \times 10^{21}$  and  $3.79 \times 10^{20}$  sample B in the dark and upon illumination, respectively.

A negatively sloped linear plot is only observed for more negative potentials and the plot may deviate from the line due to the semiconductor thickness.<sup>25</sup> The slope of the line decreased when the light is removed from this system for sample A, meaning the acceptor concentration increases, which is likely due to charge trapping at the interface of the material and the electrolyte.<sup>25</sup> Sample B had a lower concentration of charge carriers than sample A. As well, sample B did not show a linear plot over as wide a range as sample A. Although sample B is a p-type semiconductor, from both Mott-Schottky plots and PEC measurements it can be determined that it does not have as many desirable features as sample A. The absorption coefficients were calculated to be approximately  $1.6 \times 10^4 \text{ cm}^2 \text{ g}^{-1}$  for both samples A and B, which is comparable to previously reported values.<sup>27, 28</sup> Please note that the MPP capping ligand was not removed, whereas the ones in the literature were eliminated, and just the CIS was tested. Both the charge carrier concentrations and the absorption coefficient gave us insight into the photovoltaic properties of the CIS NCs made through our one-pot synthesis.



### 2.3.3 Composition

**Table 2.1 Molar Ratios for CuInS<sub>2</sub>**

<b>Method</b>	<b>Sample</b>	<b>Cu</b>	<b>In</b>	<b>S</b>
<b>Initial</b>	A	1.00	1.02	4.03
	B	1.00	1.95	3.88
	C	1.00	2.37	3.36
	D	1.00	2.00	6.56
<b>EDX</b>	A	1.00	0.49	1.34
	B	1.00	1.02	2.23
	C	1.00	0.45	1.26
	D	1.00	0.96	2.00
<b>XPS</b>	A	1.00	1.37	2.07
	B	1.00	2.54	2.88
	C	1.00	2.25	3.02
	D	1.00	2.49	3.02

EDX and XPS for measuring the composition of the resulting black powder were employed, and the resulting data is listed in Table 2.1. It was generally found that for the NCs to show a large photoresponse the starting ratios must be copper-deficient and indium-rich. Excess sulfur was required to attain a larger current density. Contrary to the initial ratios, the final product is often copper-rich and indium-deficient as was seen in the values given by the analytical methods used. Sulfur was also most often present in excess.

When the bulk composition was investigated with EDX, all four samples were copper-rich and indium-deficient with the exception of sample B. This is not unexpected as all four samples showed a photoresponse. P-type copper-rich samples are materials that are typically the most effective absorbing layers and show higher current densities.<sup>29</sup> The low current density samples were very close to a stoichiometric compound, while samples A

and D were indium-deficient. Since sulfur was added in excess, it was expected to remain in excess in the final product. However, samples A and D had comparatively less than the other samples. An excess in sulfur may increase the chance of the formation of secondary phases.<sup>30</sup>

The surface composition of the material can be seen in Table 2.1 under XPS. All samples were copper-deficient, indium-rich and sulfur-rich. The Cu(acac)<sub>2</sub> samples had less sulfur than the CuCl<sub>2</sub> samples. The presence of excess sulfur on the surface may indicate the presence of Cu<sub>2</sub>S.<sup>30</sup> Samples A and D present less indium than B and C. Sample A has the largest amount of copper at the surface which further supports correlation between photoresponse and the presence of more copper. Another interesting feature of the surface is that carbon and nitrogen were present. This is indicative that the capping ligand, MPP, is still present and supports the idea that MPP may be a part of the crystal itself.

### 2.3.4 Morphology

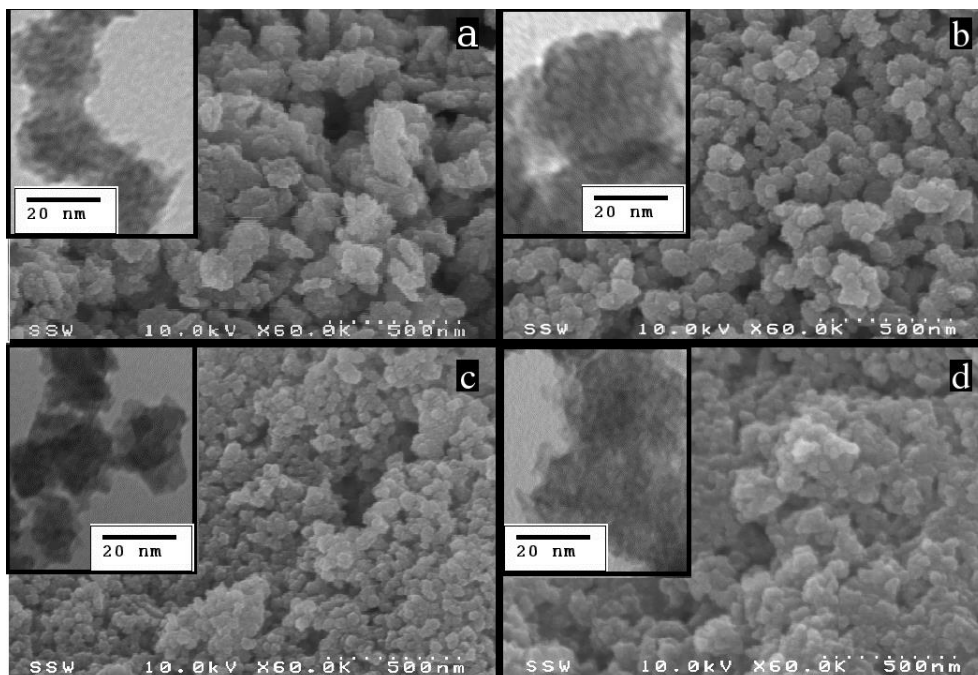


**Figure 2.4 SEM images of the samples using  $\text{Cu}(\text{acac})_2$  as the copper source a) high photocurrent (A) b) low photocurrent (B) and using  $\text{CuCl}_2$  as the copper source c) high photocurrent (C) and d) low photocurrent (D). The insets are the corresponding TEM images**

The SEM images of the four samples are shown in Figure 2.4. The structures present in all four samples were between 30 and 70 nm in diameter. The structures in samples A and C (Figure 2.4 a and c) were typically smaller than those of samples B and D (Figure 2.4b and d). The overall morphologies of samples A, B, and D showed a more amorphous surface. Sample C had more discrete particles. Samples A, D and to some extent B's particles had much more jagged edges, and it was difficult to differentiate single particles. The amorphous nature of high-photocurrent sample A may promote electron mobility throughout the film. The high-photocurrent sample C does not show this feature, which is an explanation as to why it does not produce as much photocurrent as sample A. Samples B and D showed similar morphological characteristics to sample A, although as discussed previously their composition is not ideal. The low photocurrent samples (B and D) may be producing secondary phases, which will be discussed in the next section.

The insets in Figure 2.4 are the corresponding TEM images. They reveal sizes for the structures that are on the same order of magnitude as those in the SEM images. It is evident that the structures shown in SEM are not individual particles, but rather clusters of smaller sub-structures. The clustering of smaller NCs was seen in all four samples. The sizes of these sub-structures can be investigated further using the Debye-Scherrer equation with XRD.

### 2.3.5 X-ray Diffraction

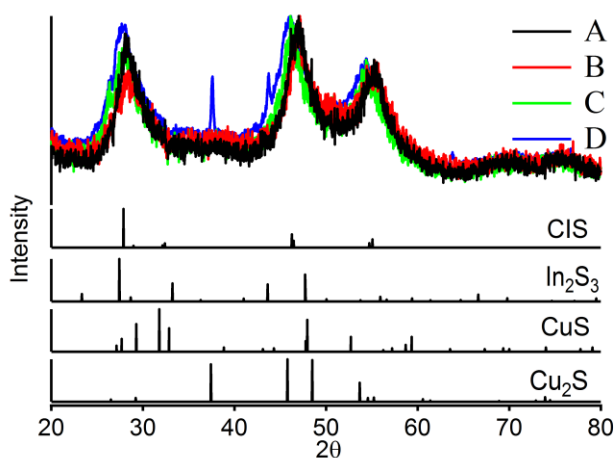


**Figure 2.5 X-ray diffraction patterns for all four samples and the standard JCPDS cards for common secondary phases**

The results for the XRD analysis are shown in Figure 2.5. All samples match well with the JCPDS card for chalcopyrite CIS. The cell parameters were calculated at  $a$  and  $b$  are equal to 5.51 Å and  $c$  is equal to 10.72 Å. These values matched well with the standard values of 5.52 Å for  $a$  and  $b$ , and 11.1 Å for  $c$ . The shortened  $c$  value could be caused by the difference in the capping ligand. The shorter MPP ligand may pack more efficiently than the oleylamine chains. It is difficult to tell if an  $\text{In}_2\text{S}_3$  phase is present as it may be obscured by the broad peaks. The copper sulfides are only distinctly present in sample D as there was a peak was observed that matched well with the  $\text{Cu}_2\text{S}$  card. This phase forming may be the cause of the inconsistency in the PEC results. If this phase can form, but not always – as in the high photocurrent  $\text{CuCl}_2$  sample C – it will inhibit the photocurrent production.

In order to calculate theoretical dimensions for the CIS products, the Debye-Scherrer equation was used (equation 2.6)<sup>31</sup> where  $D$  is the NC size,  $\lambda$  is the x-ray wavelength,  $\theta$  is the Bragg angle, and  $B(2\theta)$  is the full width at half maximum. This equation produced a theoretical NC size at approximately 2 nm for all samples. This further supports the results seen in the SEM and TEM pictures that smaller NCs cluster into larger structures.

$$D = \frac{0.9\lambda}{B(2\theta)\cos\theta} \quad (2.6)$$

### 2.3.6 Oxidation States

XPS was not only used to investigate the surface composition of the materials, but also to provide insight into the oxidation states of the elements present based on the observed binding energies (BE) listed in Table 2.2, and allowed them to be compared to literature values. Figure 2.6 displays high resolution XPS spectra of the three elements – Cu, In and S – for all four NC samples.

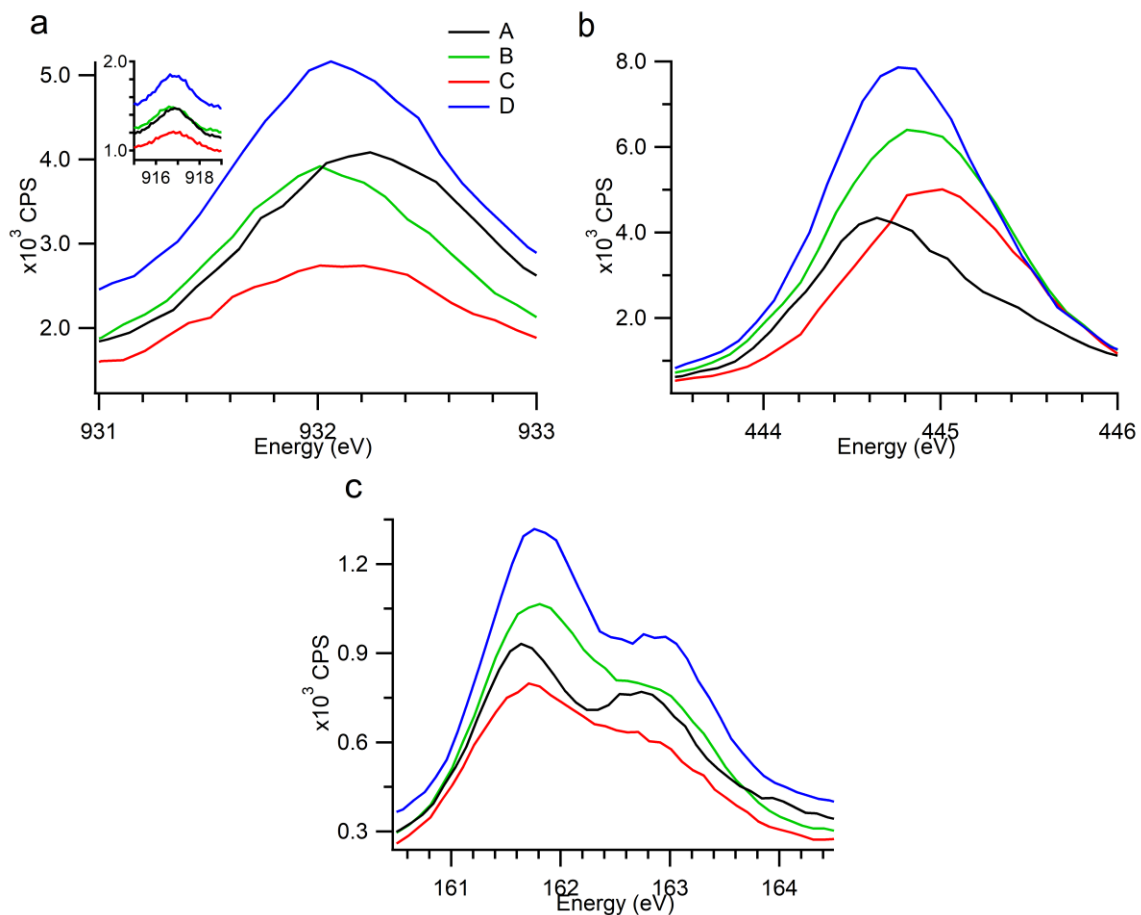


**Figure 2.6 XPS results for a) Cu 2p<sub>3/2</sub> electron binding energy (inset auger electron kinetic energy) b) In 3d<sub>5/2</sub> electron binding energy c) S 2p binding energy**

Biesinger et al. described the problems associated with the binding energies of Cu(0) and Cu(I) being often indistinguishable (932.63 eV and 932.18 eV, respectively). A modified Auger parameter sums the binding energy of the Cu 2p<sub>3/2</sub> electron and the kinetic energy of the copper Auger electron. This yields unique values for both oxidations of copper: Cu(0) at 1851.24 eV and Cu(I) at 1849.17 eV.<sup>32</sup> Through this method Cu(I) was identified in all samples. The peaks obtained in the experiment are in agreement with the peaks for In(III).<sup>33, 34</sup> Similarly, the sulfur present in the CIS is in agreement with the literature values for S<sup>2-</sup>.<sup>35</sup> These oxidation states reflect a neutral stoichiometric CIS product.

**Table 2.2 XPS binding energy results**

Sample	Copper Modified Auger Parameter (eV)	Indium BE (eV)	Sulfur BE (eV)
A	1849.0	444.65	161.64
B	1848.8	444.87	161.74
C	1849.0	444.99	161.67
D	1848.9	444.81	161.76

## 2.4 Conclusion

CIS NCs with a consistently large current density were synthesized with the starting ratio of 0.98:1:3.95 for Cu(acac)<sub>2</sub> and 0.5:1:3.27 for CuCl<sub>2</sub>. The PEC measurements allowed for the optimization of the CIS stoichiometry. The PEC measurements also gave insight into the kinetics of the photoreaction, suggesting  $k_{ps} > k_r$ . Mott-Schottky and UV-Vis experiments confirmed that the NCs are a p-type semiconductor with a high absorption coefficient. Examining the bulk composition showed a copper- and sulfur-rich material, while surface analysis showed an indium-rich, sulfur-deficient material. The sizes of the NC clusters were found to be in the 30-70 nm range. XRD patterns revealed a chalcopyrite structure with cell parameters of  $a$  and  $b$  equal to 5.5 Å and  $c$  equal to 10.7 Å, and a NC size of 2 nm. By means of XPS, oxidation states were found to be I, III, and 2- for Cu, In and S, respectively.

## 2.5 References

- (1) Komaki, H.; Furue, S.; Yamada, A.; Ishizuka, S.; Shibata, H.; Matsubara, K.; Niki, S.; *Prog. Photovolt: Res. Appl.* **2012**, *20*, 595-599.
- (2) Li, B.-Y.; Zhang, Y.; Wang, H.; Wang, B.; Wu, L.; Sun, Y.; *Prog. Photovolt: Res. Appl.* **2013**, *21*, 838-848.
- (3) Repins, I.; Contreras, M. A.; Egaas, B.; DeHart, C.; Scharf, J.; Perkins, C. L.; To, B.; Noufi, R.; *Prog. Photovolt: Res. Appl.* **2008**, *16*, 235-239.
- (4) Cherian, A. S.; Jinesh, K. B.; Kashiwaba, Y.; Abe, T.; Balamurugan, A. K.; Dash, S.; Tyagi, A. K.; Sudha Kartha, C.; Vijayakumar, K. P.; *Solar Energy* **2012**, *86*, 1872-1879.

- (5) Kemell, M.; Ritala, M.; Leskelä, M.; *Crit. Rev. Solid State Mater. Sci.* **2005**, *30*, 1-31.
- (6) Schleussner, S.; Zimmermann, U.; Wätjen, T.; Leifer, K.; Edoff, M.; *Sol. Energy Mater. Sol. Cells* **2011**, *95*, 721-726.
- (7) Ye, H.; Park, H. S.; Akhavan, V. A.; Goodfellow, B. W.; Panthani, M. G.; Korgel, B. A.; Bard, A. J.; *J. Phys. Chem. C* **2011**, *115*, 234-240.
- (8) Harati, M.; Jia, J.; Giffard, K.; Pellarin, K.; Hewson, C.; Love, D. A.; Lau, W. M.; Ding, Z.; *Phys. Chem. Chem. Phys.* **2010**, *12*, 15282-15290.
- (9) Mitzi, D. B.; Yuan, M.; Liu, W.; Kellock, A. J.; Chey, S. J.; Deline, V.; Schrott, A. G.; *Adv. Mater.* **2008**, *20*, 3657-3662.
- (10) Panthani, M. G.; Akhavan, V.; Goodfellow, B.; Schmidtke, J. P.; Dunn, L.; Dodabalapur, A.; Barbara, P. F.; Korgel, B. A.; *J. Am. Chem. Soc.* **2008**, *130*, 16770-16777.
- (11) Hibberd, C. J.; Chassaing, E.; Liu, W.; Mitzi, D. B.; Lincot, D.; Tiwari, A. N.; *Prog. Photovolt: Res. Appl.* **2010**, *18*, 434-452.
- (12) Hsin, C.-L.; Lee, W.-F.; Huang, C.-T.; Huang, C.-W.; Wu, W.-W.; Chen, L.-J.; *Nano Lett.* **2011**, *11*, 4348-4351.
- (13) Guo, Q.; Ford, G. M.; Hillhouse, H. W.; Agrawal, R.; *Nano Lett.* **2009**, *9*, 3060-3065.
- (14) Ahmed, S.; Reuter, K. B.; Gunawan, O.; Guo, L.; Romankiw, L. T.; Deligianni, H.; *Adv. Energy Mater.* **2012**, *2*, 253-259.
- (15) Timchenko, V. P. N., A.L.; Slepysheva, O.A.; *Russ. J. Gen. Chem.* **2004**, *74*, 1046-1050.
- (16) Pein, A.; Baghbanzadeh, M.; Rath, T.; Haas, W.; Maier, E.; Amenitsch, H.; Hofer, F.; Kappe, C. O.; Trimmel, G.; *Inorg. Chem.* **2010**, *50*, 193-200.
- (17) Wei, W.; Lu, Y.; Chen, W.; Chen, S.; *J. Am. Chem. Soc.* **2011**, *133*, 2060-2063.
- (18) Messaoudi, C.; Bihri, H.; Sayah, D.; Cadène, M.; Abd-Lefdil, M.; *J. Mater. Sci. Lett.* **1992**, *11*, 1234-1236.
- (19) Wang, H.; Peter, L. M.; *J. Phys. Chem. C* **2012**, *116*, 10468-10475.
- (20) Peter, L. M.; *Chem. Rev.* **1990**, *90*, 753-769.



- (21) Peat, R.; Peter, L. M.; *J. Electroanal. Chem.* **1987**, *228*, 351-364.
- (22) Li, J.; Peter, L. M.; *J. Electroanal. Chem.* **1985**, *193*, 27.
- (23) Schaming, D.; Hojeij, M.; Younan, N.; Nagatani, H.; Lee, H. J.; Girault, H. H.; *Phys. Chem. Chem. Phys.* **2011**, *13*, 17704-17711.
- (24) Fermin, D.; Duong, H.; Ding, Z.; Brevet, P.; Girault, H.; *Phys. Chem. Chem. Phys.* **1999**, *1*, 1461-1467.
- (25) Byers, J. C.; Ballantyne, S.; Rodionov, K.; Mann, A.; Semenikhin, O. A.; *ACS Appl. Mater. Interfaces* **2011**, *3*, 392-401.
- (26) Schmuki, P.; *J. Electrochem. Soc.* **1995**, *142*, 1705.
- (27) Wu, J.-J.; Jiang, W.-T.; Liao, W.-P.; *Chem. Commun.* **2010**, *46*, 5885.
- (28) Xu, J.; Luan, C.-Y.; Tang, Y.-B.; Chen, X.; Zapien, J. A.; Zhang, W.-J.; Kwong, H.-L.; Meng, X.-M.; Lee, S.-T.; Lee, C.-S.; *ACS Nano* **2010**, *4*, 6064-6070.
- (29) Hernández-Pagán, E. A.; Wang, W.; Mallouk, T. E.; *ACS Nano* **2011**, *5*, 3237-3241.
- (30) Krunksa, M.; Miklib, V.; Bijakinaa, O.; Rebanea, H.; Merec, A.; Varemaa, T.; Mellikov, E.; *Thin Solid Films* **2000**, *361-362*, 61-64.
- (31) Wu, J. M.; Chen, Y.-R.; *J. Phys. Chem. C* **2011**, *115*, 2235-2243.
- (32) Biesinger, M. C.; Lau, L. W. M.; Gerson, A. R.; Smart, R. S. C.; *Appl. Surf. Sci.* **2010**, *257*, 887-898.
- (33) McGuire, G. E.; Schweitzer, G. K.; Carlson, T. A.; *Inorg. Chem.* **1973**, *12*, 2450-2453.
- (34) Freeland, B. H.; Habeeb, J. J.; Tuck, D. G.; *Can. J. Chem.* **1977**, *55*, 1527-1531.
- (35) Moretti, G.; Anichini, A.; Fierro, G.; Lojacocono, M.; Porta, P.; *Surf. Interface Anal.* **1990**, *16*, 352-358.

### 3 Assessing the Band Structure of CuInS<sub>2</sub> Nanocrystals and Their Bonding with the Capping Ligand

(A version on this work is presented in Journal of Physical Chemistry C. Tapley, A.; Liu, L.; Cui, X.; Zuin, L.; Love, D. A.; Zhou, J.; Sham, T.-K.; Ding, Z.; *J. Phys. Chem. C* **2015**, 119, 20967-20974)

#### 3.1 Introduction

The sun is an available energy source that is vastly abundant, and it has the potential to solve the energy crisis if it can be harnessed cost-effectively. Inorganic thin-film solar cells that are renewable, environmentally friendly, and low-cost are therefore in high demand. One example of these light-absorbing semiconductor films utilizes Cu(In,Ga)Se<sub>2</sub> (CIGS). It is a promising material given that a CIGS solar cell has high laboratory photoconversion efficiencies of above 20%.<sup>1</sup> Although the use of gallium and selenium in CIGS adds undesirable costs to the CIGS-based solar cells, they can be removed and replaced, leading to a ternary chalcogenide CuInS<sub>2</sub> (CIS) that is also promising as the light absorber layer in thin-film photovoltaics.<sup>2-4</sup> CIS has a direct band gap between 1.4 and 1.5 eV and a high absorption coefficient in the range of 10<sup>4</sup> cm<sup>-1</sup> to 10<sup>5</sup> cm<sup>-1</sup>.<sup>5-7</sup> Solar cells utilizing CIS as the light-absorbing layer are therefore good candidates, with an efficiency of >10 %, <sup>2, 8</sup> and >12 % in its quasi-ternary counterpart CuIn(S, Se)<sub>2</sub>.<sup>7</sup>

The fabrication of efficient CIS solar cells currently requires high temperatures and vacuum methods in a toxic environment, both of which are preventing CIS solar cells from becoming commercially viable.<sup>7, 9-16</sup> Recently, our group has synthesized CIS nanocrystals (NCs) using a one-pot solvothermal method that avoids high-cost and dangerous techniques.<sup>16-18</sup> The NCs have been previously characterized photoelectrochemically and structurally.<sup>17, 18</sup> The use of 2-mercapto-5-*n*-propylpyrimidine (MPP) as a capping ligand in place of the typical oleylamine eliminates the need of thermal removal for the device to produce photocurrent; making it a more cost-effective capping ligand.<sup>17</sup> The interactions of this capping ligand with CIS will be addressed herein.

The CIS NCs can be synthesized at various compositions, and their properties are based on the starting molar ratio of Cu/In,<sup>9, 17, 19</sup> which allows control over the final ratio of the three elements. Copper-rich CIS has proven to achieve a higher overall quality than indium-rich CIS,<sup>9, 14, 19</sup> but synthetic methods of copper-rich CIS typically need to be etched by KCN to remove CuS for a high efficiency.<sup>10, 19, 20</sup> There has been research on how variations in the composition at different depths affects the band gap due to a secondary CuS phase,<sup>10, 19, 20</sup> but it was limited to the effect of etching the CIS surface. The one-pot synthesis finalized here does not involve KCN etching, and therefore eliminates the use of an undesirable chemical during the synthesis without sacrificing the product's high photocurrent. Also reported here is the effect of composition on the band gap and the structure without KCN etching.

X-ray absorption near edge structures (XANES) using synchrotron radiation is a powerful tool that probes the immediate surroundings of the absorbing atom in a given chemical environment. It can give invaluable information on a variety of aspects of the materials under investigation – such as element and site specificity, oxidation states, interfacial interaction, *in situ* structural evolution of materials, and *in situ* catalysis – which are difficult to obtain otherwise.<sup>21-26</sup> Secondary phases such as CuS and In<sub>2</sub>S<sub>3</sub> can inhibit photocurrent and detract from the efficiency of CIS. It can be very difficult to determine if these phases are present, as they have similar diffractograms and produce only slight shifts in Raman.<sup>17, 27</sup> Previous studies have been carried out on CIGS using synchrotron radiation, specifically to determine its conduction band (CB) using XANES.<sup>28</sup> Current research on CIS is mostly on the crystallization process (e.g. the formation mechanism) using various diffraction methods, but there has been very limited research on the electronic structure of these materials.<sup>20, 29-31</sup> There is a lack of information on the composition and bonding of the NCs, including the Cu/In ratio as well as the use of MPP as a capping ligand for CIS. MPP removes the need for the high-temperature annealing necessary with the insulating ligands typically involved in the synthesis of the NCs. Its interaction with the NCs is as of yet unknown though it has been postulated that the delocalized electronic structure of the pyrimidine rings aids in the conductivity and overall performance of the film.<sup>17</sup>

In this work, the S K-edge XANES was used to determine the phase purity and the local chemical environment in the optimized CIS NCs. N K-edge XANES was then used to explore the CIS-capping ligand interaction. Finally, the relative CB edge shift between surface and bulk was examined by S L-edge XANES with total electron yield (TEY, sampling surface of a few nanometers (nm)) and fluorescence yield (FY, sampling bulk of NCs with tens of nm probing depth) modes. The S L-edge energy lies in the soft X-ray range; ideally suited for detection at the surface. The band bending information from the surface thus obtained was combined with the bulk band gap of NCs determined by conventional optical measurement (i.e. Tauc plots) to further clarify the structure difference between low- and high-performance CIS NCs. The above undertaking provides further insight into the correlation of photoelectrochemical performance to CIS composition, band structures, and bonding with ligands.<sup>20, 28, 32</sup>

## 3.2 Experimental

CIS NCs were synthesized using a one-pot solvothermal method that has been outlined previously.<sup>17</sup> Briefly, the NCs were synthesized by combining copper acetylacetonate (Aldrich Chemical, 97%) and indium acetylacetonate (Aldrich Chemistry, 99.99%) in benzyl alcohol (Alfa Aesar, 99%); the mixture was heated to dissolve the metal salts, after which the MPP (Alfa Aesar, 98%) was added along with the thiourea (Fluka, 99.0%). The solution was then heated to 180 °C for 10 mins, and then was allowed to cool to room temperature. After rinsing with acetone and allowing the NCs to dry, they were dispersed in acetone at 20 g/L, and dropcast in two 6  $\mu$ L aliquotes onto a cleaned fluorine-doped tin oxide (FTO) glass substrate. Photoelectrochemical (PEC) measurements were carried out in a 0.05 M methyl viologen dichloride ( $MV^{2+}$ , Aldrich Chemicals, 98%) solution with 0.1 M KCl (Sigma-Aldrich, 99.0%) as the supporting electrolyte. A saturated calomel electrode (SCE) was used as a reference, and a Pt coil as the counter. All three electrodes were submerged in the  $MV^{2+}$  solution in front of a 150 W Newport lamp with an AM 1.5D filter. A shutter between the system and the light source (which operated at 0.33 Hz) was employed to provide a square-wave light stimulus to the film during the linear potential sweep. The linear sweep was from 0.0 to -0.4 V at a scan rate of 5 mV/s using a CHI 832a electrochemical analyzer.

UV-Vis absorption spectra were carried out using the same NC dispersion as described previously, and were drop cast onto a glass substrate. The scan was run on a Varian Cary 50 Bio UV-Vis spectrophotometer from 1100 nm to 400 nm. Energy dispersive X-ray spectroscopy (EDX) was carried out on a Hitachi S-4500 field emission electron microscope with a Quartz XOne system at Surface Science Western.

A Philips CM 10 transmission electron microscope at the Biotron Institute for Experimental Climate Change Research at Western was used to carry out transmission electron microscopy (TEM) measurements.

Powder X-ray Diffraction was done on the two chosen samples using an Inel CPS Powder Diffractometer with a Cu X-ray radiation (Inel XRG 3000) generator, and an Inel CPS 120 detector.

XANES experiments were carried out on the undulator based high resolution spherical grating monochromator (SGM, 11ID-1) beamline; the soft X-ray microcharacterization beamline (SXRMB, 06B1-1); and the variable line space plane grating monochromator (VLS-PGM, 11ID-2) beamline at the Canadian Light Source.<sup>33-36</sup> SGM provides a soft X-ray energy from 250 to 2000 eV with a resolution ( $E/\Delta E$ ) of  $>5000$ , which is suitable for the N K-edge XANES measurements.<sup>33, 34</sup> The S K-edge XANES spectra were measured at the SXRMB beamline, which has an energy range of 1.7–10 keV, and resolution of  $\sim 3000$  using Si(111) crystals in the double crystal monochromator.<sup>35</sup> The S  $L_{3,2}$ -edge XANES were collected at the VLS-PGM beamline (5 eV -250 eV).<sup>36</sup> The samples were dispersed on a double-sided carbon tape and mounted  $45^\circ$  toward the incident X-ray beam. XANES spectra at the SGM beamline were obtained in total electron yield (TEY) mode with the detection of sample drain current, which is surface sensitive due to the relatively short escape depth of low kinetic energy electrons, and in X-ray fluorescence yield (FY) mode with a silicon drift detector with  $< 100$  eV energy resolution at the N K-edge (AMPTEK Inc., Bedford, MA), which is relatively bulk-sensitive. The detector at the SXRMB beamline in TEY mode measured sample current and in FY mode uses a silicon drift detector from Bruker, Madison, WI. The TEY measures specimen current resulting from photoelectrons, Auger electrons, and secondary electrons; while FY

collects partial X-ray fluorescence from the element of interest (in the case of S: the S  $K_{\alpha}$  fluorescence X-rays with  $\sim 100$  eV energy resolution). In the VLS-PGM, FY is collected with a multichannel plate. In XANES, the absorption was normalized by the simultaneously measured incident beam intensity,  $I_0$ , which was monitored by a refreshed Au mesh or a nickel mesh placed in front of the sample. All spectra were background removed and normalized to a flat region of the post edge to unity.

### 3.3 Results and Discussions

#### 3.3.1 Correlation of Initial Element Ratios to Photoresponse

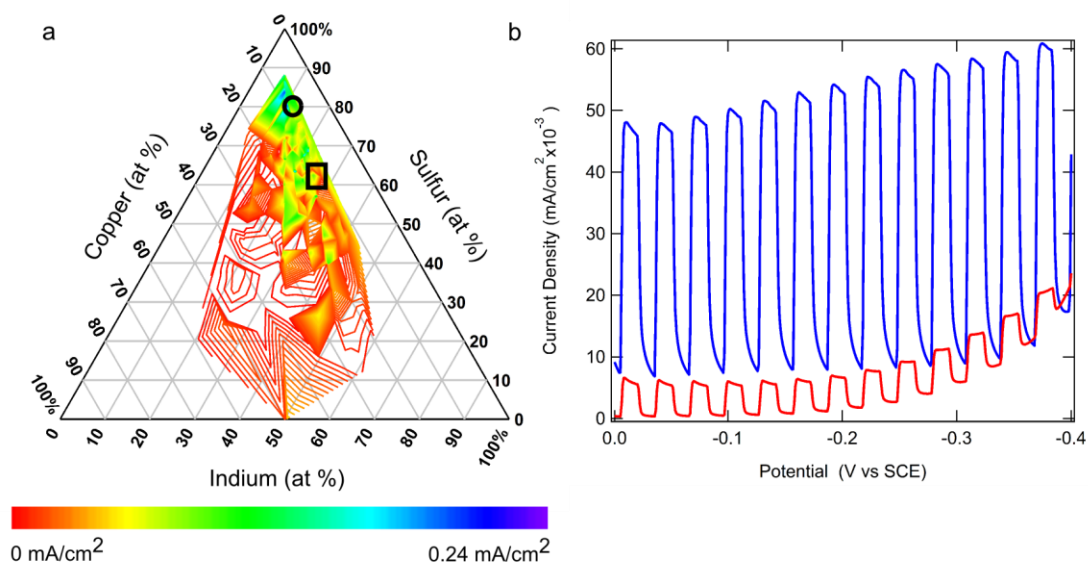


**Figure 3.1a) Ternary contour plot of the starting atomic percentages of copper, indium and sulfur for CIS with respect to the PEC measurements; and b) two sample PEC measurements of NCs that produced high (blue, sample A whose starting composition is indicated by the circle in the ternary contour plot) and low (red, sample B whose starting composition is indicated by the rectangle in the ternary contour plot) photocurrent density.**

PEC measurements were used as the foremost measure of the film quality: the larger the difference between the photocurrent and dark current the better the film.<sup>17, 37</sup> Over 200

permutations of starting molar ratios were attempted in order to optimize the recipe for CIS based on the PEC measurements. The contours in the plot shown in Figure 3.1a represent the photocurrent density measured from the resulting NCs with all the different attempted starting atomic ratios. Figure 3.1b shows the PEC measurements of two sample NC films used for comparison. Sample A (blue) exhibits a relatively large photocurrent difference which corresponds to the green/blue area highlighted in the circle on the contour plot, and sample B (red) has a relatively low photocurrent difference which corresponds to the red area highlighted in the rectangle on the contour plot. The major difference between these two samples is the initial ratio of Cu:In:S shown in Table 3.1. The final stoichiometry of the two samples obtained from EDX is depicted in Table 3.1 as well. These two samples were chosen to investigate which qualities of the films can be associated with the high- and low-photocurrent samples. Both samples began with indium-rich initial ratios, with sample B being much richer in In than sample A. The final compositions show that sample A was now indium-poor and sample B was still indium-rich, and a low Cu/In ratio negatively affects the photocurrent observed from the NCs. The starting ratios are required to be deficient in copper to prevent copper sulfide secondary phases forming, which is detrimental to the performance of CIS.<sup>9, 14</sup>

**Table 3.1 Relative molar ratios of Cu, In, and S before and after NC synthesis**

	Sample A			Sample B		
	Cu	In	S	Cu	In	S
<b>Initial</b>	1.0	3.1	4.0	1.0	6.0	8.7
<b>Final</b>	1.0±0.1	0.6±0.1	1.9±0.1	1.0±0.1	1.5±0.1	3.7±0.1

### 3.3.2 Determination of CIS Nanocrystal Band Gap

In an effort to correlate the composition of the NCs with their band gap, the optical band gap of the two samples were investigated using conventional UV-Vis spectroscopy of the

NC thin films. The band gap was obtained through the use of Tauc plots (Figure 3.2) that were transformed from the UV-vis absorption spectra using equation (3.1).<sup>38</sup>

$$(h\nu\alpha)^2 = A(h\nu - E_g) \quad (3.1)$$

Where A is a constant,  $E_g$  is the band gap,  $h\nu$  is the energy and  $\alpha$  is the absorption coefficient with the units  $\text{cm}^{-1}$ . Sample A's band gap (Figure 3.2a) was within the typical range for CIS at 1.43 eV, while sample B's (Figure 3.2b) was outside the range at 1.62 eV. The slight increase in the band gap has been previously attributed to the defects and poor crystallinity.<sup>12, 39, 40</sup> To better understand the intrinsic difference between those two samples other factors – for instance: the presence of secondary phases, as well as the coordination bonding of the capping ligand – are worth exploring since it has been previously reported that n-type CIS showed a similar band gap to that of p-type CIS.<sup>41</sup>

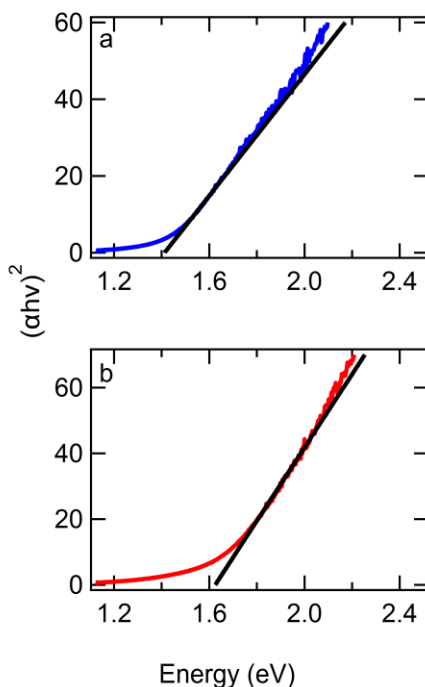


**Figure 3.2 Tauc plots of a) the high-photocurrent density sample A; and b) the low-photocurrent density sample B.**

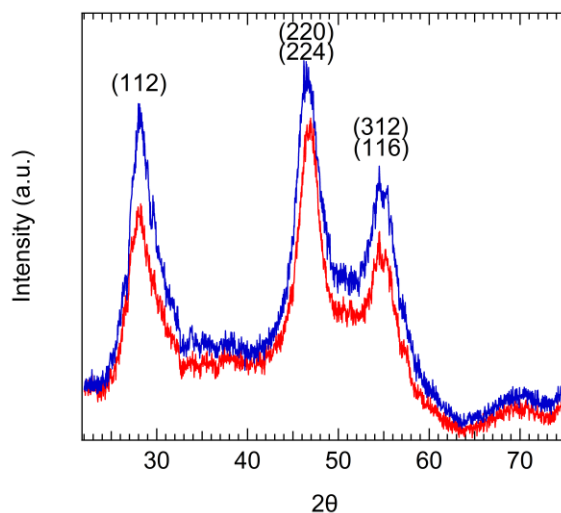
The structure of the CIS NCs was determined using XRD as seen in Figure 3.3. The diffractograms match the standard JCPDS No. 01-085-1575 card for chalcopyrite CIS. As



we reported recently, the broad peaks of the two samples made determining the presence of secondary phases impossible for  $\text{Cu}_2\text{ZnSnS}_4$ .<sup>42, 43</sup> Thus, in these systems, XRD alone cannot determine if the synthesized NCs are secondary phase free. The theoretical sizes of the NCs can be determined from XRD using the Debye-Scherrer equation shown in equation (3.2):<sup>17, 44</sup>

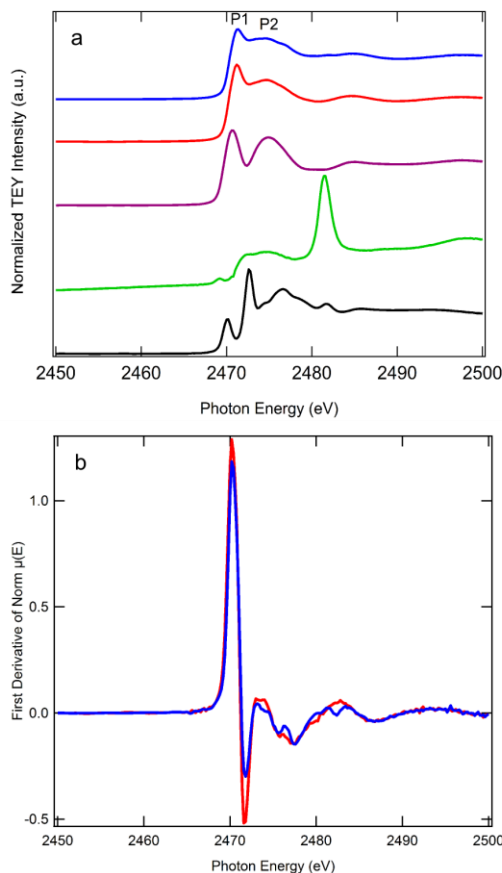
$$D = \frac{0.9\lambda}{B(2\theta)\cos\theta} \quad (3.2)$$

where  $\lambda$  is the incident X-ray wavelength,  $B(2\theta)$  is the full-width at half maximum and  $\theta$  is the Bragg angle. The NC range for both samples was determined from two separate XRD measurements. The low-photocurrent sample (red) had a NC size range of 3.8 to 5.0 nm and the high-photocurrent sample (blue) range was 3.1 to 3.2 nm. This disagrees with the particle size measured from TEM (Figures S3.1 and S3.2), which were measured to be  $44 \pm 7$  nm and  $48 \pm 7$  nm for samples A and B, respectively. This is due to the formation of clusters of NCs in the TEM measurements.<sup>43</sup> The clusters in sample B were often difficult to isolate, and their size distribution was estimated.



**Figure 3.3 XRD patterns of the high photocurrent sample (blue) and the low photocurrent sample (red).**

### 3.3.3 X-ray absorption near edge spectroscopy



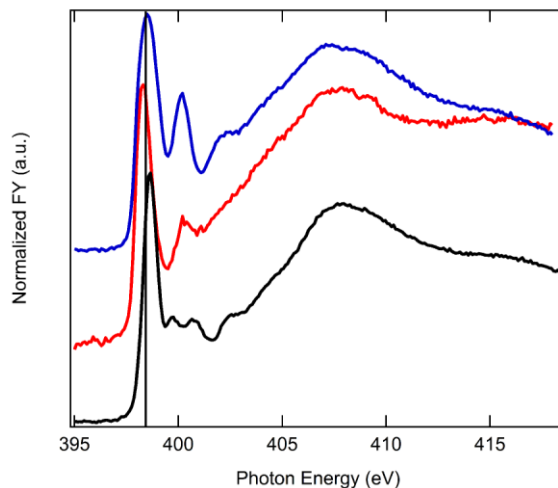
**Figure 3.4 Normalized XANES spectra in TEY mode of the sulfur K-edge for the a) high photocurrent sample A (blue), low photocurrent sample B (red),  $\text{In}_2\text{S}_3$  (purple),  $\text{Cu}_2\text{S}$  (green) and MPP (black). b) The first derivative of samples A and B.**

Figure 3.4a shows the S K-edge XANES of samples A and B together with those of standard samples for the possible secondary phases in CIS. The data was aligned as indicated by the lack of deviation in the first peaks in the first derivative spectra of A and B (Figure 3.4b). The XANES probes the S 3p character of the unoccupied states in the CB and the local symmetry. If a metal sulfide has pure ionic bonding between the metal and sulfur, then the S 3p orbital will be full when a formal valence state of -2 is obtained, and there will not be an intense S 1s to 3p transition. The existence of the intense absorption peaks (whiteline) in those metal sulfide samples clearly indicates the hybridization between the metal d orbitals and S 3p orbitals (band formation). The split

of the whitenline into two peaks (P1 and P2) in CIS could be attributed to the crystal field splitting; a phenomenon similar to that in the O K-edge XANES of metal oxides, where the oxygen 2p orbitals hybridize with the crystal field split metal 3d orbitals.<sup>45</sup>

Selenium K-edge P1 and P2 peak intensities have been found to be related to the relative amounts of copper and indium in  $\text{CuInSe}_2$  (CISe) and the Se coordination environment.<sup>46, 47</sup> CISe with a threefold coordinated Se and more Cu vacancies shows a higher P1 peak than that in CISe with fourfold coordinated Se and less Cu vacancies. Assuming S behaves similarly with Se, which is often the case in these systems, the more intense peak P1 in sample B in Figure 3.4a indicates a more distorted tetrahedral S. EDX has proven that the lower Cu/In ratio in sample B could also cause the enhanced peak P1 as being observed in CISe.<sup>46</sup> Similar to that in CISe,<sup>46</sup> sample B may have copper vacancies and indium substitutions in Cu site, antisites ( $\text{In}_{\text{Cu}}$ ). As discussed earlier, it is well established that a copper deficiency results in CIS that shows more n-type characteristics instead of the expected p-type, which would be detrimental to its performance in the solar cell.<sup>41, 48</sup> The  $\text{In}_{\text{Cu}}$  antisite defect, along with the lack of secondary phases  $\text{Cu}_2\text{S}$  and  $\text{In}_2\text{S}_3$ , is also confirmed due to a mismatch of the XANES spectra of the two samples with reference spectra of the standards of these possible species. This observation strongly indicates that the synthesized NCs are free of these secondary phases. Meaning the different band gaps and photoelectrochemistry between those two samples is not due to the effect of secondary phases, but rather to point defects distorting the crystal structure in sample B.

Another interesting observation is that the XANES of the MPP-capped CIS does not exhibit any features seen in a free MPP, which indicates strong covalent bonding between S in the MPP and the metals in CIS. As such, the S in MPP should behave as S in CIS in the S K-edge XANES.<sup>12, 39, 40</sup>



**Figure 3.5 Nitrogen K-edge in FY mode for the high photocurrent sample (blue), the low photocurrent sample (red) and MPP (black).**

The nitrogen K-edge XANES (Figure 3.5) was further explored to understand the interaction between MPP and CIS. The first peak in the spectra can be assigned to N 1s to  $\pi^*$  state transition of N in the pyrimidine ring. Both CIS samples present this signature feature that confirms the existence of MPP. Close examination of the spectra of CIS samples and free standing MPP shows that the  $\pi^*$  in sample B shifts to lower photon energy. Since the absorption edge is sensitive to the formal oxidation state of N, this shift could link with electron donation from CIS to the pyrimidine ring, and might be due to the chemical bonding between metals in CIS and S in MPP. In contrast, sample A only exhibits a shoulder on the lower energy side that broadens the  $\pi^*$  peak, while the main absorption peak stays in the same position as that of free standing MPP (marked by the vertical line). The difference between sample A and B could indicate the metal-thiol bonding strength difference in sample B bonds more strongly. Furthermore, both CIS NCs show a new peak emergence at  $\sim 400$  eV, which is absent in free-standing MPP. This is the spectroscopic evidence for the existence of chemical bonding between MPP and CIS. It is possible the strongly bonded MPP on the CIS surface has a high capping density which induces the formation of dimers,<sup>49</sup> which changes the N-C bonding geometry. Another possibility is the direct pyrimidine ring interaction with CIS; especially if the ring is parallel to CIS surface.<sup>48</sup> The more intense peak at this energy in sample A indicates a stronger pyrimidine ring-CIS interaction. It is worth emphasizing

that MPP interaction with CIS could be through the thiol group, the pyrimidine ring, or both.

Current N K-edge spectroscopy shows that sample A has stronger ring-CIS interaction but weaker thiol-CIS interaction. More interestingly, the associated electron relocation between those two types of interactions are different. Thiol-CIS interactions pull electrons from CIS, while ring-CIS interactions donate electrons to CIS. Therefore the interaction difference will contribute to the electronic structure difference at the CIS side especially on the surface. This possibility was confirmed by S L<sub>3,2</sub>-edge XANES presented below in Figure 3.6 where the interaction difference could correspond to electron loss and stronger N-metal interaction.<sup>50, 51</sup> Kelly *et al.* have shown the appearance of the 400 eV peak broadening, which they attribute to coordinating Cu<sup>2+</sup> with adenosine triphosphate, as well as charge transfer from the nitrogen to the metal, which was the cause of the broadening.<sup>51</sup>

### 3.3.4 Band structure and bonding interpretation

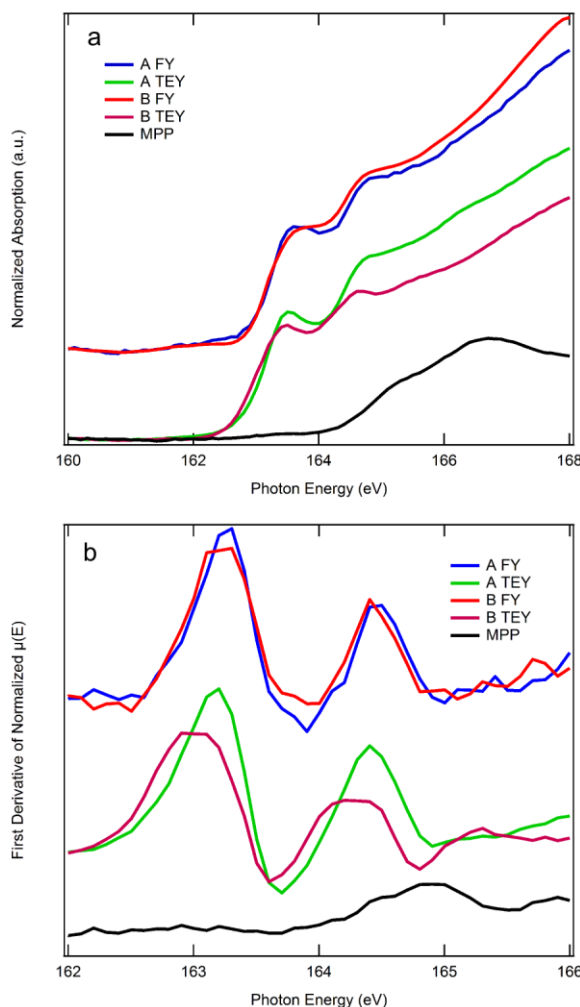


**Figure 3.6 a) The S  $L_{3,2}$ -edge spectra in TEY and FY modes, where “A” refers to the high photocurrent sample, “B” refers to the low photocurrent sample and the capping ligand reference in TEY, MPP, is in black for comparison. b) The first derivative spectra of samples A and B as well as MPP using the same color codes as in a).**

The S  $L_{3,2}$ -edge encompasses transitions from the S  $2p_{3/2,1/2}$  (with the spin orbit coupling of  $\sim 1.1$  eV) to the S 3s (dominant) and 3d orbitals. In CIS, this spectroscopy is also influenced by the  $\text{In}^{3+}$  valence and inner valence orbitals due to hybridization. The spectra shown in Figure 3.6a have two peaks corresponding to the  $L_3$  and  $L_2$  edges. It is plausible that MPP interacts with the surface of CIS via the S end, as the edge sharpens

and shifts to lower photon energy in both A and B. Let us focus on the first peak and compare the spectral features from the TEY (surface sensitive) with those of the FY (bulk sensitive). While there is no difference between peak energies in FY mode for the two samples, those of sample B in TEY mode are lower than the counterparts of sample A, Figure 3.6. Interestingly, the width of the resonance in FY is comparable to or less than those of the TEY indicating that there is no saturation effect in these thin samples and the bulk is more ordered. There is a downward shift in energy for peak 1 from the bulk (FY mode) to the surface (TEY mode) in both samples, as clearly indicated by the first derivative spectra in Figure 3.6b. This reflects the shift of the bottom of the CB of S character relative to the electron energy of the S  $2p_{3/2}$ , assuming the effect of the core hole is the same for both the bulk and the surface region.

Further examination of the S L-edge XANES in Figure 3.6 shows the same CB position in the bulk for both samples, while the surface CB bends to the Fermi level by  $\sim 0.1$  eV in sample A and 0.3 eV in sample B. These were estimated by the onsets of the XANES that was obtained by the linear extrapolation of the leading S  $L_3$  absorption edge as shown in Figure 3.6.<sup>52</sup>

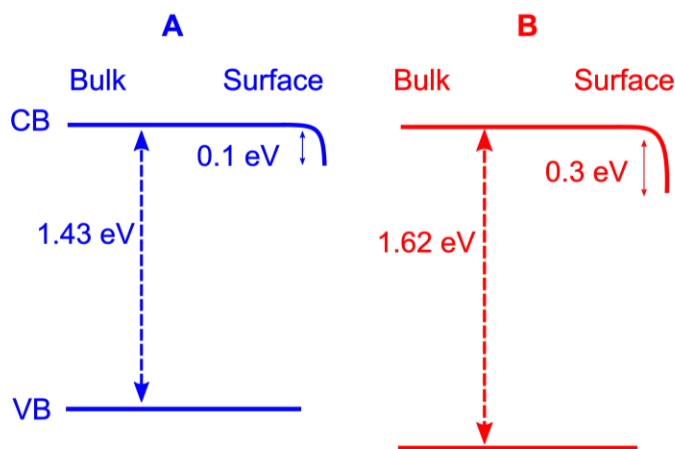


**Figure 3.7 Bulk band gap and surface conduction band gap bending for the high photocurrent sample (A); and the low photocurrent sample (B).**

An energy diagram of the band structure for each sample can be constructed as follows: the band gap values obtained from the Tauc plots in Figure 3.2 constitute the main frames

of the bands in Figure 3.7 where the top of the VB in the bulk can be determined by referring to the CB position. The energy for the bottom of the CB in the bulk of samples A and B is the same level as that determined by S L-edge XANES in FY mode (Figure 3.6). The surface band bending in CB can be visualized to a first approximation, assuming the TEY is surface sensitive and FY is bulk sensitive.<sup>53</sup> The band bending due to charge neutralization and the truncation of the lattice at the surface followed by MPP-surface interaction can be constructed from the energy shift in Figure 3.6 and is illustrated in Figure 3.7. The two samples are depicted in Figure 3.7a (sample A) and Figure 3.7b (sample B).

The amount of indium in sample B increases the amount of electrons in the system, making sample B have less p-type character than sample A. At the surface of sample B, the increased indium content causes surface states that inhibit the photogenerated electrons from transferring to the  $MV^{2+}$  couple due to recombination. A band gap gradient, however, has been well-established to increase the open circuit voltage ( $V_{oc}$ ) of a semiconductor film used in solar cells.<sup>54, 55</sup> This band gap gradient produces an electric field that aids in pushing photogenerated electrons in the bulk to the surface, increasing the photocurrent.<sup>55</sup> Band bending through defects, such as in B, only serves to hinder the photogenerated electrons. The MPP-CIS interaction is relevant to the difference in surface band bending between A and B observed here, although the stoichiometric effect cannot be excluded. While sample B has a larger surface band bending than A (Figure 3.7), the less p-type semiconducting nature (Fermi level moves towards the CB) and defect states in the band gap might hinder photogenerated electrons in the bulk from reaching the surface.

### 3.4 Conclusions

Using XANES spectroscopy, copper-rich CIS NCs that exhibit a high photocurrent density and copper-poor NCs with a low photocurrent density have been investigated. XANES provides distinctly different spectral features between good and poor performers. Both CIS samples are shown to be free of secondary phases, but the sample with a low photocurrent density had a distorted crystal structure and intrinsic defects. The band gap was initially measured using conventional methods, which gave the bulk band gaps of



1.43 eV for the high performance copper-rich (A) film and 1.62 eV for the low performance copper-poor (B) film. XANES at S L-edge were used to determine the CB bending at the surface region, which shows a shift in the bottom of the CB position from the bulk to the surface of the NCs. The shift in sample A with its p-type semiconducting feature is less dramatic, and would promote carrier collection and prevent recombination. The large surface band bending in Sample B prevents it from enhancing the photocurrent due to its n-type semiconducting feature, which makes this bending behave like a shallow surface state annihilating the electron hole pairs.

### 3.5 References

- (1) Jackson, P.; Hariskos, D.; Lotter, E.; Paetel, S.; Wuerz, R.; Menner, R.; Wischmann, W.; Powalla, M.; *Prog. Photovolt. Res. Appl.* **2011**, *19*, 894-897.
- (2) Siemer, K.; Klaer, J.; Luck, I.; Bruns, J.; Klenk, R.; Bräunig, D.; *Sol. Energy Mater. Sol. Cells* **2001**, *67*, 159-166.
- (3) Pan, D.; An, L.; Sun, Z.; Hou, W.; Yang, Y.; Yang, Z.; Lu, Y.; *J. Am. Chem. Soc.* **2008**, *130*, 5620-5621.
- (4) Panthani, M. G.; Akhavan, V.; Goodfellow, B.; Schmidtke, J. P.; Dunn, L.; Dodabalapur, A.; Barbara, P. F.; Korgel, B. A.; *J. Am. Chem. Soc.* **2008**, *130*, 16770-16777.
- (5) Xu, J.; Wang, Y.; *Mater. Lett.* **2013**, *99*, 90-93.
- (6) Scheer, R.; *Prog. Photovolt. Res. Appl.* **2012**, *20*, 507-511.
- (7) Liu, W.; Mitzi, D. B.; Yuan, M.; Kellock, A. J.; Chey, S. J.; Gunawan, O.; *Chem. Mater.* **2010**, *22*, 1010-1014.
- (8) Scheer, R.; Walter, T.; Schock, H. W.; Fearheiley, M. L.; Lewerenz, H. J.; *Appl. Phys. Lett.* **1993**, *63*, 3294-3296.
- (9) Tsai, C.-H.; Mishra, D. K.; Su, C.-Y.; Ting, J.-M.; *Int. J. Energ. Res.* **2014**, *38*, 418-428.
- (10) Sun, J.; Batabyal, S. K.; Tran, P. D.; Wong, L. H.; *J. Alloys Compd.* **2014**, *591*, 127-131.
- (11) Schneider, N.; Bouttemy, M.; Genevee, P.; Lincot, D.; Donsanti, F.; *Nanotechnology* **2015**, *26*, 054001.

- (12) Lee, S. H.; Shin, S. W.; Han, J. H.; Lee, J. Y.; Kang, M. G.; Agawane, G. L.; Yun, J. H.; Moon, J. H.; Kim, J. H.; *Electron. Mater. Lett.* **2012**, *8*, 191-197.
- (13) Ikeda, S.; Nonogaki, M.; Septina, W.; Gunawan, G.; Harada, T.; Matsumura, M.; *Catal. Sci. Tech.* **2013**, *3*, 1849-1854.
- (14) Ho, J. C.; Zhang, T.; Lee, K. K.; Batabyal, S. K.; Tok, A. I.; Wong, L. H.; *ACS Appl. Mater. Interfaces* **2014**, *6*, 6638-6643.
- (15) Graeser, B. K.; Hages, C. J.; Yang, W. C.; Carter, N. J.; Miskin, C. K.; Stach, E. A.; Agrawal, R.; *Chem. Mater.* **2014**, *26*, 4060-4063.
- (16) Tapley, A.; Hart, C.; Vaccarello, D.; Love, D. A.; Ding, Z.; *J. Electrochem. Soc.* **2014**, *161*, H725-H729.
- (17) Tapley, A.; Vaccarello, D.; Hedges, J.; Jia, F.; Love, D. A.; Ding, Z.; *Phys. Chem. Chem. Phys.* **2013**, *15*, 1431-1436.
- (18) Vaccarello, D.; Hedges, J.; Tapley, A.; Love, D. A.; Ding, Z.; *J. Electroanal. Chem.* **2015**, *738*, 35-39.
- (19) Lewerenz, H. J.; *Sol. Energy Mater. Sol. Cells* **2004**, *83*, 395-407.
- (20) Bär, M.; Klaer, J.; Weinhardt, L.; Wilks, R. G.; Krause, S.; Blum, M.; Yang, W.; Heske, C.; Schock, H.-W.; *Adv. Energ. Mater.* **2013**, *3*, 777-781.
- (21) Sham, T. K.; *Adv. Mater.* **2014**, *26*, 7896-7901.
- (22) Chen, C.-W.; Wu, D.-Y.; Chan, Y.-C.; Lin, C. C.; Chung, P.-H.; Hsiao, M.; Liu, R.-S.; *J. Phys. Chem. C* **2015**, *119*, 2852-2860.
- (23) Hines, D. A.; Becker, M. A.; Kamat, P. V.; *J. Phys. Chem. C* **2012**, *116*, 13452-13457.
- (24) Kan, Y. C.; Hu, Y.; Croy, J.; Ren, Y.; Sun, C. J.; Heald, S. M.; Bareno, J.; Bloom, I.; Chen, Z. H.; *J. Power Sources* **2014**, *266*, 341-346.
- (25) Jia, C. K.; Liu, Q.; Sun, C. J.; Yang, F.; Ren, Y.; Heald, S. M.; Liu, Y. D.; Li, Z. F.; Lu, W. Q.; Xie, J.; *ACS Appl. Mater. Interfaces* **2014**, *6*, 17920-17925.
- (26) Liu, X.; Yang, W.; Liu, Z.; *Adv. Mater.* **2014**, *26*, 7710-7729.
- (27) Álvarez-García, J.; Pérez-Rodríguez, A.; Barcones, B.; Romano-Rodríguez, A.; Morante, J. R.; Janotti, A.; Wei, S.-H.; Scheer, R.; *Appl. Phys. Lett.* **2002**, *80*, 562-564.
- (28) Johnson, B.; Klaer, J.; Merdes, S.; Gorgoi, M.; Höpfner, B.; Vollmer, A.; Lauermaun, I.; *J. Electron. Spectrosc. Relat. Phenom.* **2013**, *190*, 42-46.

- (29) Thomas, D.; Mainz, R.; Rodriguez-Alvarez, H.; Marsen, B.; Abou-Ras, D.; Klaus, M.; Genzel, C.; Schock, H. W.; *Thin Solid Films* **2011**, *519*, 7193-7196.
- (30) Mainz, R.; Klenk, R.; *J. Appl. Phys.* **2011**, *109*, 123515.
- (31) Fischereder, A.; Rath, T.; Haas, W.; Amenitsch, H.; Schenk, D.; Zankel, A.; Saf, R.; Hofer, F.; Trimmel, G.; *ACS Appl. Mater. Interfaces* **2012**, *4*, 382-390.
- (32) Zhou, X.; Heigl, F.; Ko, J.; Murphy, M.; Zhou, J.; Regier, T.; Blyth, R.; Sham, T.; *Phys. Rev. B* **2007**, *75*.
- (33) Regier, T.; Paulsen, J.; Wright, G.; Coulthard, I.; Tan, K.; Sham, T. K.; Blyth, R. I. R.; In *Commissioning of the Spherical Grating Monochromator Soft X-ray Spectroscopy Beamline at the Canadian Light Source*, AIP Conference Proceedings, 2007; pp 473-476.
- (34) Regier, T.; Krochak, J.; Sham, T. K.; Hu, Y. F.; Thompson, J.; Blyth, R. I. R.; *Nucl. Instrum. Methods Phys. Res., Sect. A* **2007**, *582*, 93-95.
- (35) Hu, Y. F.; Coulthard, I.; Chevrier, D.; Wright, G.; Igarashi, R.; Sitnikov, A.; Yates, B. W.; Hallin, E. L.; Sham, T. K.; Reininger, R.; In *Preliminary Commissioning and Performance of the Soft X-ray Micro-characterization Beamline at the Canadian Light Source*, AIP Conference Proceedings, Melbourne, Australia, Melbourne, Australia, 2010; pp 343-346.
- (36) Kasrai, M.; Yin, Z.; Bancroft, G. M.; Tan, K. H.; *J. Vac. Sci. Technol., A* **1993**, *11*, 2694-2699.
- (37) Ye, H.; Park, H. S.; Akhavan, V. A.; Goodfellow, B. W.; Panthani, M. G.; Korgel, B. A.; Bard, A. J.; *J. Phys. Chem. C* **2011**, *115*, 234-240.
- (38) Tauc, J.; *Mater. Res. Bull.* **1968**, *3*, 37-46.
- (39) Thai, T. T.; *Commun. Phys.* **2012**, *22*, 59-64.
- (40) Sebastian, T.; Jayakrishnan, R.; Kartha, C. S.; Vijayakumar, K. P.; *The Open Surface Science Journal* **2009**, *1*, 1-6.
- (41) Courtel, F. M.; Paynter, R. W.; Marsan, B. t.; Morin, M.; *Chem. Mater.* **2009**, *21*, 3752-3762.
- (42) Vaccarello, D.; Liu, L.; Zhou, J.; Sham, T.-K.; Ding, Z.; *J. Phys. Chem. C* **2015**, *119*, 11922-11928.
- (43) Khoshmashrab, S.; Turnbull, M. J.; Vaccarello, D.; Nie, Y.; Martin, S.; Love, D. A.; Lau, P. K.; Sun, X.; Ding, Z.; *Electrochim. Acta* **2015**, *162*, 176-184.
- (44) Wu, J. M.; Chen, Y.-R.; *J. Phys. Chem. C* **2011**, *115*, 2235-2243.

- (45) Zhou, J. G.; Fang, H. T.; Maley, J. M.; Murphy, M. W.; Peter Ko, J. Y.; Cutler, J. N.; Sammynaiken, R.; Sham, T. K.; Liu, M.; Li, F.; *J. Mater. Chem.* **2009**, *19*, 6804-6809.
- (46) Yamazoe, S.; Kou, H.; Wada, T.; *J. Mater. Res.* **2011**, *26*, 1504-1516.
- (47) Just, J.; Lützenkirchen-Hecht, D.; Frahm, R.; Schorr, S.; Unold, T.; *Appl. Phys. Lett.* **2011**, *99*, 262105.
- (48) Joachim, M. H., *Semiconductors for Solar Cells*. Boston, 1993.
- (49) Hohenstein, E. G.; Sherrill, C. D.; *J. Phys. Chem. A* **2009**, *113*, 878-886.
- (50) Liang, Y.; Wang, H.; Zhou, J.; Li, Y.; Wang, J.; Regier, T.; Dai, H.; *J. Am. Chem. Soc.* **2012**, *134*, 3517-3523.
- (51) Kelly, D. N.; Schwartz, C. P.; Uejio, J. S.; Duffin, A. M.; England, A. H.; Saykally, R. J.; *J. Chem. Phys.* **2010**, *133*, 101103.
- (52) Bär, M.; Nishiwaki, S.; Weinhardt, L.; Pookpanratana, S.; Fuchs, O.; Blum, M.; Yang, W.; Denlinger, J. D.; Shafarman, W. N.; Heske, C.; *Appl. Phys. Lett.* **2008**, *93*, 244103.
- (53) Hill, I. G.; Rajagopal, A.; Kahn, A.; Hu, Y.; *Appl. Phys. Lett.* **1998**, *73*, 662-664.
- (54) Gabor, A. M.; Tuttle, J. R.; Bode, M. H.; Franz, A.; Tennant, A. L.; Contreras, M. A.; Noufi, R.; Jensen, D. G.; Hermann, A. M.; *Sol. Energy Mater. Sol. Cells* **1996**, *41/42*, 247-260.
- (55) Woo, K.; Kim, Y.; Yang, W.; Kim, K.; Kim, I.; Oh, Y.; Kim, J. Y.; Moon, J.; *Sci. Rep.* **2013**, *3*, 3069.

## 4 Characterization of a $\text{CuInS}_2$ Monolayer Linked to FTO by Polarization Measurements and X-ray Absorption Spectroscopy

### 4.1 Introduction

Harnessing the sunlight that reaches the earth every day in a cost-effective, environmentally-friendly manner is no small feat. It requires highly-tuned materials capable of absorbing light and producing free charge-carriers that can be used to extract energy.  $\text{CuInS}_2$  (CIS) is a light-absorbing semiconductor that can be used for this purpose because it has a high absorption coefficient and a direct band gap well suited to the absorption of the solar spectrum.<sup>1-3</sup> There are a variety of ways CIS can be synthesized, some of which include: molecular precursors,<sup>4-10</sup> sulfurization of the metals,<sup>11</sup> atomic layer deposition,<sup>12</sup> and nanocrystal (NC) synthesis.<sup>1,3,13</sup> This work utilizes CIS NCs synthesized using a simple, low-cost, one-pot technique which uses relatively-low temperatures, non-toxic conditions, and is performed in ambient atmosphere.<sup>14-18</sup> It provides the potential to severely reduce the costs associated with the fabrication of CIS solar cells, thus making them suitable for commercialization.

The deposition of the NCs is an important step in the fabrication of solar cells, but it is not always a simple procedure. Achieving high solar cell device efficiency requires a uniform film devoid of cracks, pinholes, and irregularities.<sup>19</sup> Many of the reported techniques deposit films with a high electrical connectivity to the back contact using dangerous conditions<sup>7,8,20</sup> or high temperatures<sup>21</sup> in an attempt to achieve those requirements. These measures, however, increase both the financial and environmental costs of producing the solar cells. Furthermore, research regarding photoinduced electron transfer at the interface is limited. This work explored a novel method of chemically attaching the CIS NCs to the back contact using (3-mercaptopropyl)trimethoxysilane (MPTMS) as a linker molecule. The technique precludes the use of both toxic solvents and high temperatures.

MPTMS has been employed extensively to attach gold nanoparticles to an indium tin oxide (ITO) back contact for use in electrochemistry.<sup>22-29</sup> It is a short-chain molecule that

can attach to a metal oxide via a condensation reaction of its silane end, thereby leaving the thiol group available to bond to the gold nanoparticles. It has also been previously shown that the terminal sulfur in MPTMS can attach to copper metal.<sup>30</sup> In this work, a metal oxide back contact – fluorine tin oxide (FTO) coated glass – was functionalized with the MPTMS and then dipped in a dispersion of CIS NCs that spontaneously attached to the surface of the FTO via MPTMS's terminal sulfur group. This study has shown, for the first time, MPTMS's capability of adhering CIS NCs to the back contact. The ability of these monolayers to produce a photocurrent was tested and compared with a CIS NC thin film on FTO coated glass.

Further characterization of the CIS monolayer in comparison with the CIS thin film proved to be difficult, as the signal from the monolayer was too low to be detected by conventional techniques. X-ray absorption near edge structure (XANES) was able to overcome this issue because it is highly sensitive to local structure and the chemical environment of specific atoms.<sup>31</sup> As we reported elsewhere, the structure of CIS NCs has been proven to have no secondary phases, and the interactions with the capping ligand have been shown through the use of XANES.<sup>16</sup> In this study, XANES was used to probe the Cu L-edge as well as the S K- and L-edges of both the thin film CIS and the CIS monolayer to determine if there are any structural differences between the CIS monolayer and the thin film. XANES was also used to determine if there was a preferred orientation of the NCs on the surface of the FTO using polarization-resolved experiments.

## 4.2 Experimental

### 4.2.1 Nanocrystal Synthesis

The CIS NCs were synthesized using a pre-established one-pot synthesis published elsewhere.<sup>14</sup> Briefly, copper acetylacetonate (Aldrich Chemistry, 97%) and indium acetylacetonate (Aldrich Chemistry 99.99%) were dissolved in benzyl alcohol after which a solution of 2-mercapto-5-propylpyrimidine (MPP, Alfa Aesar 98%) and thiourea (Fluka 99.0%) pre-dissolved in benzyl alcohol was added. The elements were in a starting molar ratio of 1.00:0.99:8.33 for Cu:In:S. The solution was then heated to 180 °C for 10 mins, resulting in the CIS NCs. The NCs were centrifuged out of the solution and

washed with acetone and then isopropanol. Finally, the NCs were centrifuged out of solution and allowed to air dry.

#### 4.2.2 Nanocrystal Monolayer and Film Deposition

The procedure for the functionalization of MPTMS (Aldrich Chemicals, 95%) on ITO<sup>22, 27, 32-35</sup> was adapted to FTO. Briefly, cleaned FTO glass was placed in a vial containing 1 v/v% of MPTMS ethanol solution for 12 hours. It was then rinsed with ethanol and allowed to air dry. The MPTMS-FTO glass was then placed in a stirred dispersion of 2 g/L CIS NCs in isopropanol for 24 hours. For comparison, CIS thin films were fabricated by drop casting two 6  $\mu$ L drops of a 20 g/L CIS NCs dispersion in isopropanol onto a 10 mm<sup>2</sup> area of cleaned FTO coated glass substrates.

#### 4.2.3 Characterization

Photoelectrochemical measurements were carried out as published elsewhere<sup>14, 16</sup> using a saturated calomel reference electrode and a platinum counter electrode in a solution of 0.05 M methyl viologen dichloride (MV<sup>2+</sup>, Aldrich Chemicals, 98%) and 0.1 M potassium chloride. The working electrode was the CIS NC film or monolayer FTO substrates described above. A square wave light stimulus at a frequency of 0.167 Hz from a 150 W Newport lamp with an AM 1.5D filter and an electronic chopper was applied in conjunction with a linear potential sweep from 0 V to -0.4 V at a scan rate of 5 mV/s using a CHI 832a electrochemical analyzer. SEM images were performed on a Hitachi S-4500 field emission microscope (Toronto, ON). Contact angle measurements were carried out on a Krüss DSA 100 (Matthews, NC) using 2  $\mu$ L drops of water.

XANES measurements were carried out at three beamlines at the Canadian Light Source in Saskatoon, SK. The beamlines are the high resolution spherical grating monochromator (SGM, 11ID-1), the soft X-ray microcharacterization (SXRMB, 06B1-1) and the variable line space plane grating monochromator (VLS-PGM, 11ID-2). The SGM beamline provided soft X-ray energy from 250 to 2000 eV with a resolution ( $E/\Delta E$ ) of  $>5000$  that was used for the Cu L-edge measurements.<sup>36</sup> SXRMB had an energy range of 1.7-10 keV and a resolution of  $\sim 3000$  using Si(111) crystals in the double crystal monochromator and was used for the S K-edge.<sup>37</sup> Finally, the energy range for the VLS-

PGM was 5-250 eV for the S L-edge detection.<sup>38</sup> The samples were all mounted at 45° to the incident X-ray beam at all three beamline terminals. TEY was used at both the SGM and SXRMB beamlines, and measures the drain current from the samples, which consists of photoelectrons, Auger electrons, and secondary electrons. Fluorescence yield (FY) was collected using a channel plate detector at the VLS-PGM beamline. A Si drift detector from Bruker, Madison WI was used for FY measurements on the SXRMB and SGM beamlines. The XANES measurements were normalized by simultaneously measuring the incident beam intensity ( $I_0$ ), which was monitored by a refreshed Au or Ni mesh placed in front of the sample. All spectra had the background removed, the energy corrected, and were normalized by taking a flat region in the pre-edge and post edge and setting it to zero and unity respectively. While TEY mode is more surface sensitive due to the short escape distance of low kinetic energy electrons, FY mode is bulk sensitive.

#### 4.2.4 Polarization Measurements

The polarization dependent measurements were conducted at the SGM beamline at the CLS. The initial setup is shown in Figure 4.1, which is a schematic of the starting position of the sample. The sample is mounted so the X-ray beam hits it at a 45° angle and the X-ray beam corresponds to the y-axis in the figure. This angle is shown in red in the figure. There are four detectors surrounding the sample. The direct path from the sample to the detector is shown in dashed line to help with visualization. Detector 1 is along the x-axis, which is 90° from the X-ray beam and is directly above the sample. Similarly, detector 3 is 90° from the X-ray beam, but along the z-axis. The right angles for these two detector paths are shown in the figure in blue. Detector 2 is in the x-y plane and is at 45° with the beam while detector 4 is in the y-z plane and is also 45° from the beam. The sample is then rotated around the y-axis (or around the incident beam) toward detector 3 and 4 such that the angle between the incident X-ray beam and the sample does not change, but the angles between the sample and the detectors do. The sample was rotated to 23, 45, 67, and 90 degrees relative to its starting position. In fact, the rotations changed the incident polarization from 0 (parallel) to 90° (vertical) relative to the sample plane. In this way, the sample rotation is equivalent to changing the beam polarization via an elliptically polarizing undulator as reported by Arnold et al for Al complex



orientations.<sup>39</sup> In the final position (90° to its starting position), detector 3 is now directly above the sample and detector 1 is in the same plane as the sample. FY spectra were taken at each rotation.

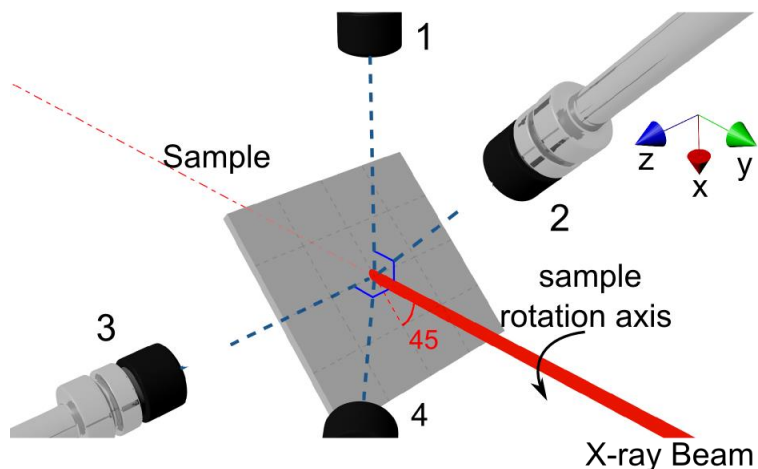


**Figure 4.1** Experimental schematic for the angular-dependent measurements

## 4.3 Results and Discussions

### 4.3.1 CIS Monolayer Linked to FTO

A procedure for attaching CIS NCs to the surface of FTO has been adapted from the silanization of ITO with MPTMS to attach metal nanoparticles to surfaces.<sup>22, 27, 32-35, 40-42</sup>

The attaching/linking mechanisms are highlighted in Figure 4.2. This process first involves the hydrolysis of one methoxy group resulting in a Si – O bond, which subsequently – through condensation – attaches to the FTO surface. There is some variation in the literature over exactly how the MPTMS attaches to the surface (it is through either crosslinked Si – O bonds or a single Si – O bond) so both extremes are shown in Figure 4.2 A and B.<sup>22, 27, 28, 41, 43, 44</sup> Regardless, this procedure creates a thiol

terminated monolayer over the FTO.

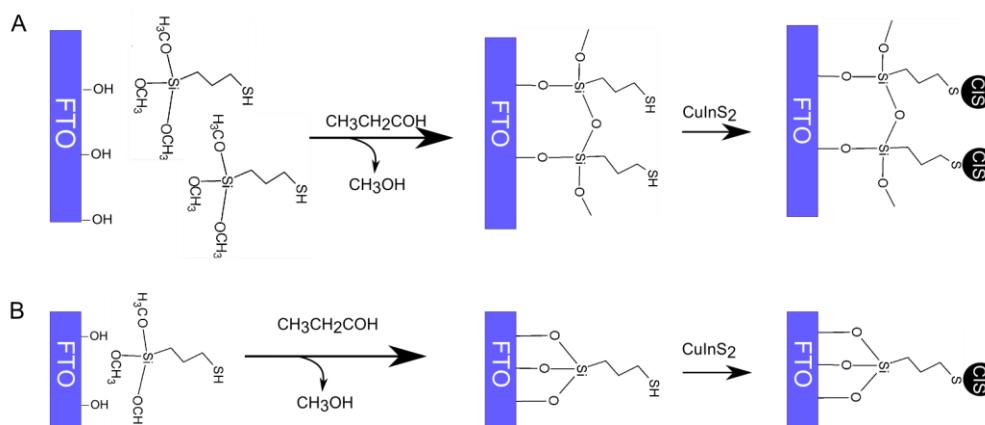


**Figure 4.2 Attachment of the linker and the CuInS<sub>2</sub> to the surface of the metal oxide via single Si – O bond (A) or multiple Si – O bonds (B).**

There have also been various studies on the orientation of the MPTMS molecules at the surface. Previously, angle-dependant X-ray photoelectron (XPS) studies have determined that the MPTMS film can have a minor amount of polymerization and some variation in the orientation of the MPTMS on the surface, which would change the head group (a methyl group instead of the thiol), however it is generally uniform.<sup>45</sup> In an effort to determine the coverage of the NCs, contact angle measurements were performed. The contact angle was  $38 \pm 8^\circ$  for the FTO alone, and  $18 \pm 4^\circ$  for the MPTMS coated FTO. The surface is more hydrophilic with the MPTMS on it. The thiol group might decrease the contact angle because of its hydrophilic nature. The lowered contact angle with the MPTMS suggested that there are many thiol head groups.

The thiol groups can attach to the CIS NCs and form a CIS NC head monolayer on the FTO. As previously mentioned, this method is most often used to attach gold nanoparticles to an ITO surface for use as an electrode for electrochemistry.<sup>23, 24, 26, 27, 43, 44, 46</sup> It has been demonstrated in this work, for the first time, that MPTMS linked to a FTO surface can be employed to attach CIS NCs for use in photoelectrochemistry. The short carbon chain of MPTMS allows for electron transfer via tunneling.<sup>25</sup> MPTMS has a significantly lower tunneling energy barrier (2 to 2.5 eV) than that of longer alkyl chains, which makes it a good candidate to attach CIS NCs to the FTO surface.<sup>25</sup>

### 4.3.2 Photoelectrochemical Measurements

The PEC measurements for the CIS monolayer and the drop cast CIS are shown in Figure 4.3. Figure 4.3A is the PEC measurement of the linked CIS (L-CIS), Figure 4.3B is the PEC measurement of the FTO without MPTMS that was dipped in a CIS dispersion (NL-CIS), and Figure 4.3C is the PEC measurement of drop cast CIS (DC-CIS) NC films with a thickness of 1 to 2  $\mu\text{m}$ . The photocurrent density range for each sample is 3.49 to 13.3  $\mu\text{A}/\text{cm}^2$ , 0.634 to 2.06  $\mu\text{A}/\text{cm}^2$ , and 13.3 to 14.5  $\mu\text{A}/\text{cm}^2$  for L-CIS, NL-CIS and DC-CIS, respectively. The NL-CIS in Figure 4.3B had a very small photocurrent density indicating that some CIS NCs may adhere to the surface of the FTO due to its roughness, but without a linker molecule there is nothing securing the NCs to the FTO. The L-CIS current density difference is on the same order of magnitude as that of the approximately 1  $\mu\text{m}$  DC-CIS film sample. This is remarkable because the L-CIS uses significantly less material than the DC-CIS and yet a similar photocurrent is obtained.

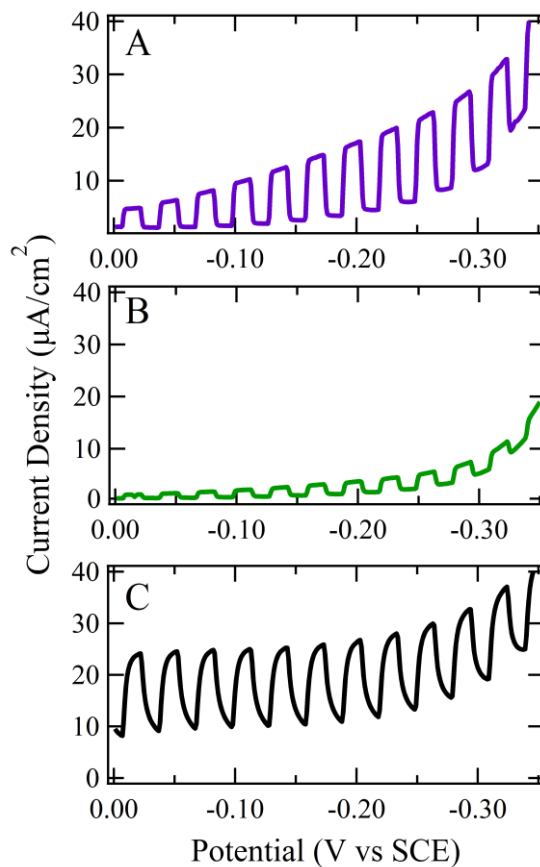
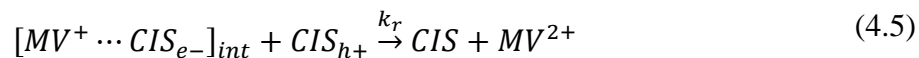
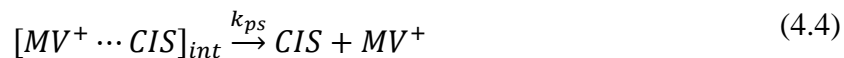


**Figure 4.3 PEC measurements in a 0.05 M  $MV^{2+}$  of A) MPTMS linked FTO with  $CuInS_2$  B) FTO without MPTMS after being dipped in  $CuInS_2$  and C) 1-2  $\mu m$  thick  $CuInS_2$  film.**

One feature of the PEC measurements is that at higher negative bias the L-CIS and NL-CIS voltammograms have a dark current that increases with time. This can be explained by the high negative bias pushing more electrons through the film or the partial coverage of the CIS over the back contact. A lack of full coverage of the CIS (due to a methyl head group rather than a thiol head group) would cause the back contact to be exposed to the  $MV^{2+}$ . The FTO could then transfer electrons directly to the  $MV^{2+}$ , and cause the rise in dark current observed at more negative potentials.

The shape of the photocurrent transients offers an explanation as to the cause of the high photocurrent observed from the L-CIS. Square oscillations are observed for the L-CIS and NL-CIS (Figure 4.3A and B) with a steady rise in the photocurrent upon illumination. This can be explained by Figure 4.4 and equations (4.1) through (4.5). In the first step of Figure 4.4, the incoming light creates an electron hole pair which is found in equation (4.1). This photogenerated electron/hole pair then either immediately recombines (equation (4.2)) leading to no photocurrent, or the electron and hole separate (equation (4.3)) and the reaction proceeds to step 2 in Figure 4.4. In this step, the electron reduces the  $MV^{2+}$  to  $MV^+$  causing the current that is observed in the PEC measurement (equation (4.4)), or it can undergo recombination (equation (4.5)) which detracts from the photocurrent. If product separation does occur, the photogenerated hole is then filled through electron tunneling with an electron from the FTO which is under negative bias. Electron tunneling is possible due to the short length, 0.8 nm, of the MPTMS molecule.<sup>25</sup>



The  $k_R$  and  $k_{PS}$  are the recombination and product separation rates, respectively. Their relative ratios can be observed qualitatively in the PEC measurements in the shape of the photocurrent rise and decay.<sup>47, 48</sup> The initial sharp rise in current observed in all the PEC measurements is due to the injected photons causing a surge of electrons available to couple with the  $MV^{2+}$ . The square oscillations of the L-CIS and the NL-CIS indicate a large  $k_{PS}/k_R$  ratio.<sup>48</sup> The CIS monolayer has a decreased number of traps and other

opportunities for the photogenerated electron to be lost. This increases the amount of electrons available to be scavenged by the  $MV^{2+}$ , which increases the  $k_{PS}$  rate to much larger than that of  $k_R$ . The photocurrent also does not show a negative overshoot when the light is switched off, which again suggests a small recombination rate.

In the PEC measurement of the DC-CIS (Figure 4.3C), a different phenomenon was observed: after the initial surge, the current slowly rises and never plateaus. This signifies that slow charge carrier diffusion is the dominant process.<sup>48, 49</sup> The electrons that are generated deeper in the film upon illumination take time to reach the surface to react with the  $MV^{2+}$ , which increases the likelihood of them being lost in traps and holes. This overall decrease in available photogenerated electrons would be reflected in a smaller  $k_{PS}/k_R$  ratio and the slow rise in the photocurrent, as described in the intensity-modulated photocurrent spectroscopy reported elsewhere.<sup>48</sup>

The L-CIS film would be producing the same amount of photogenerated electrons at the surface as the bulk film. The high photocurrent is the result of very few electrons being lost to recombination or traps as they can be readily scavenged by the  $MV^{2+}$  (Figure 4.4). The photogenerated electrons are collected more effectively in the L-CIS/ $MV^{2+}$  system which makes the L-CIS promising for fabricating high efficiency solar cells.

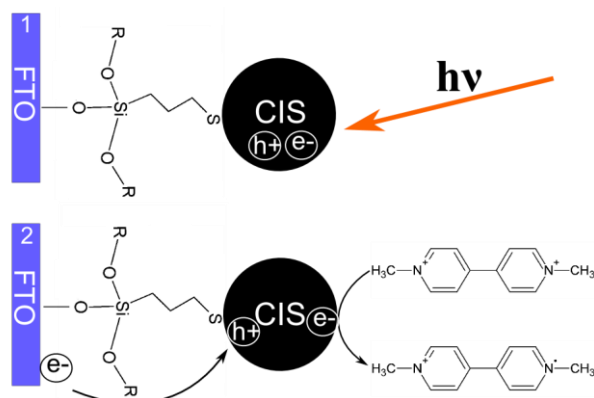


**Figure 4.4 Schematic demonstration of the PEC measurements of the CIS monolayer with  $MV^{2+}$  1) An incoming photon creates an electron hole pair in the CIS that is linked to the surface of the FTO with MPTMS; 2) The photogenerated electron reduces the methyl viologen and the photogenerated hole is filled with an electron from the FTO.**

### 4.3.3 X-ray Absorption Near-Edge Structure (XANES)

Elucidation of the structure of the CIS monolayer was carried out to further determine if there were any changes to it – or other important characteristics – that caused the increased photocurrent. Synchrotron radiation provided a convenient method of characterizing the structures of the CIS NCs, the MPTMS, and the CIS head group, due to its sensitivity to changes in the local electronic environment.

#### 4.3.3.1 Sulfur

In the structure of the one-pot synthesis CIS NCs, there are two different sulfur atoms involved: the sulfur directly in the chalcopyrite CIS structure and the sulfur present in the capping ligand, MPP. The bonding of the MPP to the CIS NCs was previously determined to be through the sulfur atom.<sup>16</sup> The MPTMS in the L-CIS adds yet another sulfur atom to the system: the thiol group on the end of a short aliphatic chain meant to bind the CIS NCs to the surface. The MPP and MPTMS linked to FTO are shown along with the L-CIS spectra for comparison when possible.

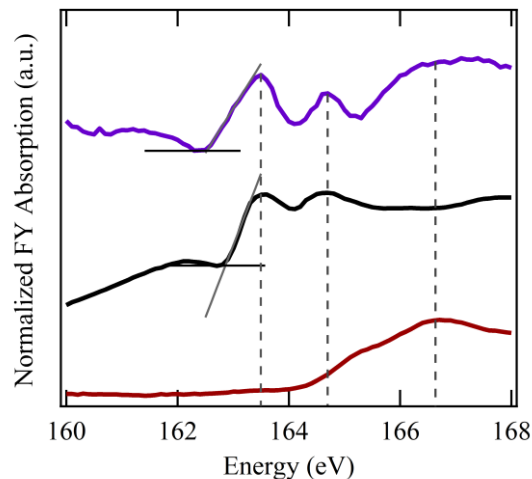


**Figure 4.5** The sulfur L<sub>3,2</sub>-edge of CIS linked to FTO with the MPTMS (purple) spin coated CIS (black) and the capping ligand, 2-mercapto-5-propylpyrimidine (red).

The S L<sub>3,2</sub> edge for the L-CIS, DC-CIS, and MPP are depicted in Figure 4.5. The L<sub>3</sub> and L<sub>2</sub> peaks occurred at 163.5 eV and 164.6 eV for both L-CIS (purple) and for DC-CIS (black). These peaks represent the electron transitions from the S 2p<sub>3/2</sub> and 2p<sub>1/2</sub> orbitals to the S 3s and 3d orbitals, with some contribution from In<sup>3+</sup> due to hybridization.<sup>16</sup> The two peaks for both the L-CIS and DC-CIS are, characteristically, 1.1 eV apart, and not very intense because this energy range removes shallow electrons. The peak positions and the lack of peaks in the 166 to 183 eV range confirm the oxidation state for sulfur as -2 for the L-CIS and the DC-CIS.<sup>50</sup> In the L-CIS spectrum there is also a broad peak at 166.5 eV, which corresponds to the contribution from the capping ligand (MPP, the red trace in Figure 4.5). The spectrum of MPTMS linked to the FTO without the CIS NCs could not be obtained due to low signal.

The conduction band can be determined using the linear extrapolation of the leading L<sub>3</sub> absorption edge back to the x-axis.<sup>16, 51</sup> The extrapolations are shown in grey on both the L-CIS (purple) and the DC-CIS (black) in Figure 4.5. These give values of 162.5 eV for the L-CIS and 163.5 eV for the DC-CIS. This means that there is a conduction band shift down by 1 eV in the L-CIS compared to the DC-CIS. The lowered conduction band is due to electron donation from the sulfur atom on the MPTMS to the CIS NC. The



MPTMS is not formally bonded as there are no major deviations between the DC-CIS and L-CIS spectra. The sulfur does donate electron density to the CIS NC.

The lowered conduction band can also explain the features from the PEC measurements. The conduction band of the L-CIS will lie closer to the energy band of the  $MV^{2+}$ . When they are in contact, the band bending that occurs is less than that of the DC-CIS. The easy band-bending makes the charge separation of the photogenerated electrons more efficient. This would be reflected in the increased  $k_{PS}/k_R$  ratio, and thus the square oscillations were observed.

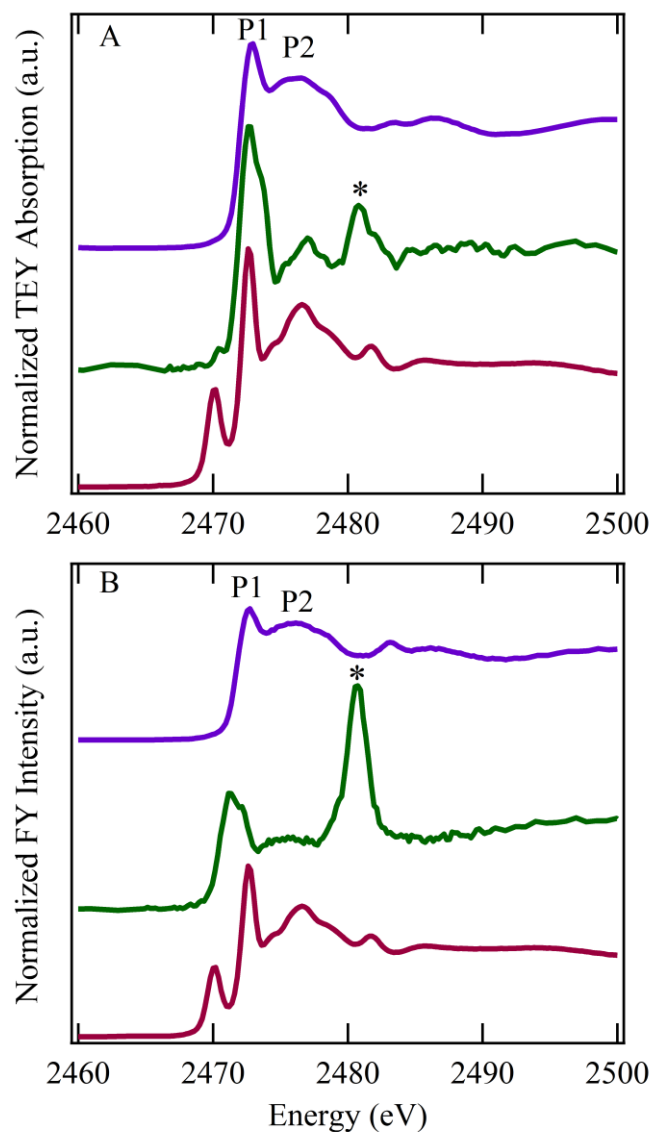


**Figure 4.6** The sulfur K-edge of the CIS linked to the FTO (purple), the MPTMS linked to FTO (green) and the capping ligand 2-mercapto-5-propylpyrimidine (red) for A) TEY mode and B) FY mode \* denotes a sulfate peak present in the glass substrate.

The S K-edge spectra of L-CIS, MPTMS linked to FTO, and MPP alone are presented in TEY mode (Figure 4.6A) and FY mode (Figure 4.6B). All spectra had an intense absorption edge at 2472 eV. There is a 2 eV blue shift the for L-CIS peak in comparison

with that for the CIS NCs as we reported previously.<sup>16</sup> This is due to the significant contribution to the spectrum from the MPTMS linker molecule.

The S K-edge for CIS involved probing the unoccupied 3p states in the conduction band.<sup>16</sup> The intense absorption edge that is observed in the spectra is indicative of hybridization between the metal d and S 3p orbitals. This means a formal oxidation state of -2 for sulfur was confirmed.<sup>14, 16, 50</sup> The L-CIS (purple) absorption edge is split into two smaller peaks for both FY and TEY which are labelled P1 and P2 in the figure. The split in the whiteness (absorption edge) in both the L-CIS and MPTMS on FTO can be attributed to crystal field splitting.<sup>16, 52, 53</sup>

Sulfur – in the -2 oxidation state in CIS – is in a tetrahedral arrangement which is subject to crystal field splitting. A distortion of the tetrahedral arrangements, or local defects in the structure, would cause an alteration of the electron density surrounding the sulfur which would manifest as a change in the P1 and P2 intensities. A change in the coordination number (CN) around the sulfur would change the specific electron density around the sulfur atom and could be causing the whiteness split.<sup>53</sup> There is a small increase in the intensity in the TEY P1 peak compared to the FY P1 peak. This shift in intensity is indicative of a small distortion in the tetrahedral arrangement of the sulfur in at the interface, a lower CN on the sulfur, or both.

The MPTMS linked to FTO (green) has a large increase in intensity when going from FY to TEY. The peak is sharper in the surface sensitive TEY mode because the terminal sulfur atoms may only have a CN of 3 or there is a distortion in the atoms surrounding the sulfur. The split in the MPTMS spectrum (green), which is less pronounced in the TEY mode, suggests fewer S–H bonds at the surface. Regardless, when the CIS is introduced to the system, any indication of an S–H bond disappears leaving sulfur in the -2 oxidation state, but now associated with a metal. The L-CIS exhibits very little structural change compared with the S K-edge of bulk CIS that has been obtained previously.<sup>16</sup> The structure of CIS is conserved when it is present in the monolayer.

The peak that appears at approximately 2480 eV (marked with an asterisk) in the FY and TEY spectra of the MPTMS is attributed to oxidized sulfurs in the form of sulfates.<sup>54, 55</sup>

The oxidized sulfur peak is caused by impurities in the glass itself rather than being present in the L-CIS layer. S K-edge scans were performed on unaltered FTO glass (SI Figure S4.1). These TEY and FY spectra also have a peak at ~2480 eV, which is confirmations that this peak is due to sulfates in the glass.<sup>54, 55</sup>

#### 4.3.3.2 Copper

The Cu L-edge spectra for the DC-CIS and the L-CIS are displayed in Figure 4.7 in TEY (Figure 4.7A) and FY (Figure 4.7B) modes. The whiteness for both modes occurred at 932.5 eV. The absorption edge energy for all four spectra indicate that copper is present as Cu(I) which agrees with previous studies done on the CIS NCs.<sup>14, 56-58</sup> This fact is further confirmed by the absorption edge occurring at a relatively high energy and the lack of a significant peak at 930 eV.<sup>59, 60</sup> There is, however, a very small pre-edge peak at approximately 930 eV in all four spectra. The copper L-edge involves the transitions of the electrons in the 2p state to the vacant 3d orbitals.<sup>59, 60</sup> Since Cu(I) has a filled d shell, no peaks should appear before the edge, as no transitions into the d band are possible. These small peaks are due to the copper in chalcopyrite showing a mix of d<sup>10</sup> and d<sup>9</sup> characteristics.<sup>56, 59, 61</sup> Previous studies have confirmed that there is no Cu(II) present in the CIS NCs,<sup>14</sup> thus the observed d<sup>9</sup> character is due to dipoles from local crystal defects.

The TEY L-CIS spectrum matched closely with that of the DC-CIS, with the exception of broadening in the FY spectrum. The broadening of the FY spectrum in the DC-CIS compared to the L-CIS is due to the thickness of the DC-CIS, which would increase self-absorption, thereby broadening the peak in the FY spectrum. Otherwise, this, combined with the sulfur edges, is concrete proof that the structure of the CIS is conserved in the monolayer.

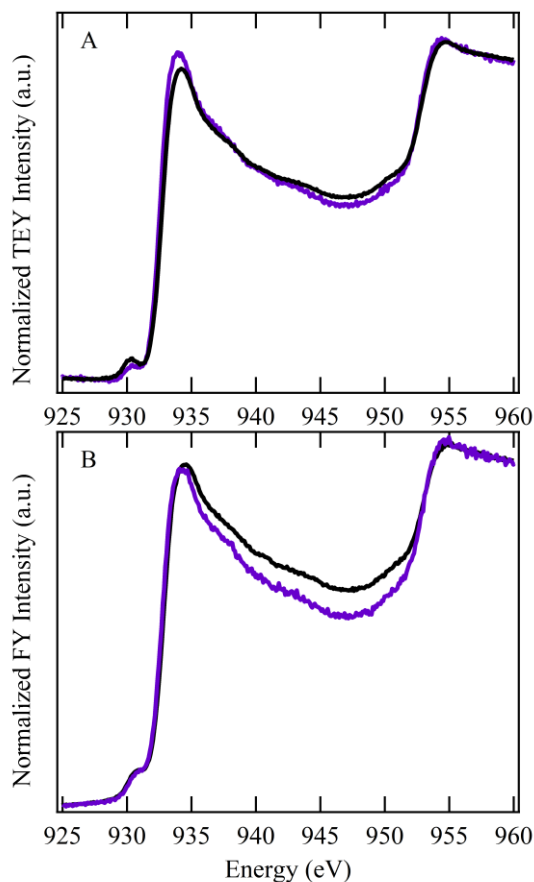


**Figure 4.7** Cu  $L_3$ -edge measurement of bulk CIS (black) and CIS linked to FTO with MPTMS (purple) in A) TEY mode and B) FY mode.

#### 4.3.3.3 Angular Dependent Measurements

The FY spectra obtained from the four detectors at the starting position of the sample as described by Figure 4.1 are displayed in Figure 4.8. The intention of these experiments was to probe the polarization dependence of the CIS NCs attached to the surface of FTO with MPTMS. Molecular orientation experiments have previously been performed on semiconducting polymers,<sup>62</sup> and a system with a CN adsorbed on the surface of Pt.<sup>63</sup> The incident X-ray beam is horizontally polarized due to the highly collimated nature of synchrotron radiation and as such can be used to determine if the CIS NCs have polarization dependence, based on their orientation. The four spectra in Figure 4.7

display identical features, because the four detectors are measuring the same unpolarized fluorescence from various positions. Different spectrum intensities can be observed.

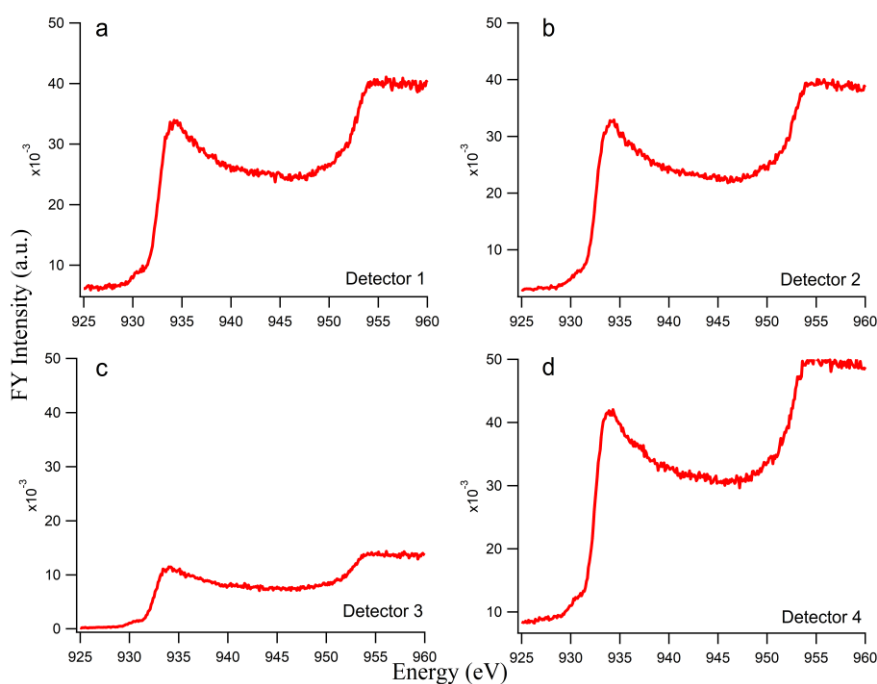


**Figure 4.8 Cu L-edge FY measurements at the starting position of the angular-dependent measurement set up for a) detector 1, b) detector 2, c) detector 3, and d) detector 4.**

If the NCs were all in the same orientation their atomic orbitals would align. These alignments would pervade the film and would be reflected in shift in the absorption edge. If the incident X-ray beam's polarization is aligned with the orbitals it would cause the FY signal to blue shift as the electrons are held more tightly due to the interaction between the electric field produced by the beam and the one in the atomic orbital causing them to rise in energy. This phenomenon can be described by using the analogous system of crystal field theory. In the case of a metal with an octahedral arrangement of the ligands, the metal d-orbitals that lie on the axis increased in energy due to an increased repulsion from the ligand electron density. In this system, the incoming polarized X-ray beam acts like the ligand. When it is aligned with the atomic orbitals of the copper, it causes the orbital energies to increase due to the repulsion of the electric field of the beam. This would manifest in the FY spectra as a blue shift in the white line energy as it

would take more energy to remove the electrons.<sup>64</sup> In order to determine if there is polarization dependence in the monolayer, the FY spectrum would change when polarization of the X-ray beam is changed by 90 ° relative to the sample. The sample was therefore rotated in three increments between 0 ° and 90 ° around the axis of the beam.

The FY spectra for the four rotations are shown in Figure 4.9. In the case where all the molecular orbitals of the CIS NCs were aligned throughout the entirety of the film, a shift in the  $E_0$  would be observed. However, no shift in any of the absorption edges from any rotation/polarization is observed. There are several explanations for this observation. The first might be a lack of alignment in the molecular orbitals. If the orbitals were all oriented randomly, then the signals would all average out and no polarization dependence would be observed. The lack of shift could also arise from electrons from the ligand (in this case sulfur) filling the X-ray ejected electron hole on the copper (rather than an electron from the copper itself) through shake down transitions.<sup>65</sup> In such a case, regardless of the orbital alignment with the beam, electron-transitions would occur throughout the film and cause a delocalized fluorescence. This would result in broadening the signal, and obscure any shifts due to angular dependence.

Finally, the copper in CIS is in a tetrahedral arrangement and the incoming polarized X-ray beam may interact with more than one orbital. The contributions from the combined orbital interactions would also serve to alter the peak in a more additive way, and obscure individual angular-dependent signals. It is therefore likely that the NCs are either oriented randomly and there is no polarization dependence or individual orbital angular dependencies exist, but are obscured by the competing angular dependencies of other orbitals within the film.

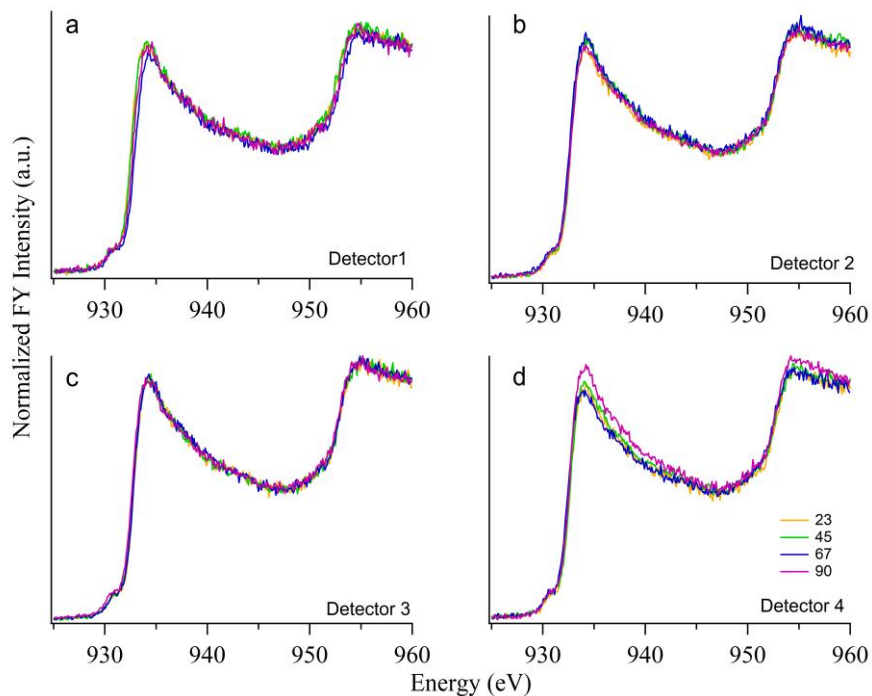


**Figure 4.9 Cu L-edge FY measurements at four different angles relative to the starting sample position for angular-dependent measurements for a) detector 1, b) detector 2, c) detector 3 and d) detector 4.**

## 4.4 Conclusion

CIS NCs were successfully – and for the first time – linked to the FTO surface using MPTMS. The PEC measurement from the L-CIS demonstrated a photocurrent on the same order of magnitude as that from a much thicker drop-cast CIS film. The photogenerated electrons produced in the monolayer were more effectively scavenged by the  $MV^{2+}$  as there was less opportunity for them to recombine or be lost to traps in the film. The sulfur in the MPTMS donated electron density to the CIS head group which lowered the conduction band making charge separation more favourable, and increasing the product separation rate. The XANES studies confirmed that the structure of the CIS NCs is conserved. The polarization-dependent XANES of the Cu L-edge suggested that there is possibly no preferred orientation of the NCs linked to the FTO surface.



The CIS monolayer that is chemically attached to the FTO surface is a good model to be incorporated into full devices to understand losses due to recombination from cracks and pinholes possibly present in a thicker film of CIS. It will dramatically reduce the material costs associated with solar cells, and has the potential to be scaled up. The NC dispersion requires no additives that need to be removed, and no toxic conditions are employed. This new monolayer shows great promise in making the commercialization of CIS solar cells a reality.

## 4.5 References

- (1) Panthani, M. G.; Akhavan, V.; Goodfellow, B.; Schmidtke, J. P.; Dunn, L.; Dodabalapur, A.; Barbara, P. F.; Korgel, B. A.; *J. Am. Chem. Soc.* **2008**, *130*, 16770-16777.
- (2) Xu, J.; Wang, Y.; *Mater. Lett.* **2013**, *99*, 90-93.
- (3) Huang, W. C.; Tseng, C. H.; Chang, S. H.; Tuan, H. Y.; Chiang, C. C.; Lyu, L. M.; Huang, M. H.; *Langmuir* **2012**, *28*, 8496-8501.
- (4) Chung, C.-H.; Bob, B.; Lei, B.; Li, S.-H.; Hou, W. W.; Yang, Y.; *Sol. Energy Mater. Sol. Cells* **2013**, *113*, 148-152.
- (5) Chung, C.-H.; Lei, B.; Bob, B.; Li, S.-H.; Hou, W. W.; Duan, H.-S.; Yang, Y.; *Chem. Mater.* **2011**, *23*, 4941-4946.
- (6) Chung, C.-H.; Li, S.-H.; Lei, B.; Yang, W.; Hou, W. W.; Bob, B.; Yang, Y.; *Chem. Mater.* **2011**, *23*, 964-969.
- (7) Liu, W.; Mitzi, D. B.; Yuan, M.; Kellock, A. J.; Chey, S. J.; Gunawan, O.; *Chem. Mater.* **2010**, *22*, 1010-1014.
- (8) Hou, W. W.; Bob, B.; Li, S.-h.; Yang, Y.; *Thin Solid Films* **2009**, *517*, 6853-6856.
- (9) Heo, J.; Kim, G. H.; Jeong, J.; Yoon, Y. J.; Seo, J. H.; Walker, B.; Kim, J. Y.; *Sci. Rep.* **2016**, *6*, 36608.
- (10) Tiwari, D.; Koehler, T.; Lin, X.; Sarua, A.; Harniman, R.; Wang, L.; Klenk, R.; Fermin, D. J.; *ACS Appl. Mater. Interfaces* **2017**, *9*, 2301-2308.
- (11) Huang, Q.; Reuter, K.; Amhed, S.; Deligianni, L.; Romankiw, L. T.; Jaime, S.; Grand, P. P.; Charrier, V.; *J. Electrochem. Soc.* **2011**, *158*, D57-D61.
- (12) Schneider, N.; Bouttemy, M.; Genevée, P.; Lincot, D.; Donsanti, F.; *Nanotechnology* **2015**, *26*, 054001.
- (13) Zeng, T.; Ni, H.; Chen, Y.; Su, X.; Shi, W.; *Mater. Lett.* **2016**, *172*, 94-97.

- (14) Tapley, A.; Vaccarello, D.; Hedges, J.; Jia, F.; Love, D. A.; Ding, Z.; *Phys. Chem. Chem. Phys.* **2013**, *15*, 1431-1436
- (15) Vaccarello, D.; Tapley, A.; Ding, Z.; *RSC Adv.* **2013**, *3*, 3512-3515.
- (16) Tapley, A.; Liu, L.; Cui, X.; Zuin, L.; Love, D. A.; Zhou, J.; Sham, T.-K.; Ding, Z.; *J. Phys. Chem. C* **2015**, *119*, 20967-20974.
- (17) Tapley, A.; Hart, C.; Vaccarello, D.; Love, D. A.; Ding, Z.; *J. Electrochem. Soc.* **2014**, *161*, H725-H729.
- (18) Guo, Q.; Kim, S. J.; Kar, M.; Shafarman, W. N.; Birkmire, R. W.; Stach, E. A.; Agrawal, R.; Hillhouse, H. W.; *Nano Lett.* **2008**, *8*, 2982-2987.
- (19) Huang, Y.; Tang, Y.; Yuan, W.; Wang, Q.; Zhang, S.; *Mater. Sci. Semicond. Process.* **2017**, *57*, 227-232.
- (20) Ishikawa, R.; Oya, T.; Yamada, T.; Nomoto, T.; Tsuboi, N.; *Thin Solid Films* **2017**, *634*, 1-5.
- (21) Lee, S. M.; Ikeda, S.; Yagi, T.; Harada, T.; Ennaoui, A.; Matsumura, M.; *Phys. Chem. Chem. Phys.* **2011**, *13*, 6662-6669.
- (22) Tseng, J.-Y.; Lin, M.-H.; Chau, L.-K.; *Colloids Surf., A* **2001**, *182*, 239-245.
- (23) Cheng, W.; Dong, S.; Wang, E.; *Langmuir* **2002**, *18*, 9947-9952.
- (24) Zhang, J.; Kambayashi, M.; Oyama, M.; *Electrochem. Commun.* **2004**, *6*, 683-688.
- (25) Aswal, D. K.; Lenfant, S.; Guerin, D.; Yakhmi, J. V.; Vuillaume, D.; *Small* **2005**, *1*, 725-729.
- (26) Chen, Z.; Zu, Y.; *Langmuir* **2007**, *23*, 11387-11390.
- (27) Ballarin, B.; Cassani, M. C.; Scavetta, E.; Tonelli, D.; *Electrochim. Acta* **2008**, *53*, 8034-8044.
- (28) Muthurasu, A.; Ganesh, V.; *J. Colloid Interface Sci.* **2012**, *374*, 241-249.
- (29) Sheen Mers, S. V.; Umadevi, S.; Ganesh, V.; *ChemPhysChem* **2017**, *18*, 1358-1369.
- (30) Sui, W.; Zhao, W.; Zhang, X.; Peng, S.; Zeng, Z.; Xue, Q.; *J. Sol-Gel Sci. Technol.* **2016**, *80*, 567-578.
- (31) Sham, T. K.; *Adv. Mater.* **2014**, *26*, 7896-7901.
- (32) Doron, A.; Katz, E.; Willner, I.; *Langmuir* **1995**, *11*, 1313-1317.
- (33) Baker, B. E.; Natan, M. J.; Zhu, H.; Beebe Jr, T. P.; *Supramol. Sci.* **1997**, *4*, 147-154.

- (34) Gu, Z.; Jing, C.; Ying, Y. L.; He, P.; Long, Y. T.; *Theranostics* **2015**, *5*, 188-195.
- (35) Jing, C.; Gu, Z.; Ying, Y. L.; Li, D. W.; Zhang, L.; Long, Y. T.; *Anal. Chem.* **2012**, *84*, 4284-4291.
- (36) Regier, T.; Krochak, J.; Sham, T. K.; Hu, Y. F.; Thompson, J.; Blyth, R. I. R.; *Nucl. Instrum. Methods Phys. Res., Sect. A* **2007**, *582*, 93-95.
- (37) Hu, Y. F.; Coulthard, I.; Chevrier, D.; Wright, G.; Igarashi, R.; Sitnikov, A.; Yates, B. W.; Hallin, E. L.; Sham, T. K.; Reininger, R.; *AIP Conference Proceedings* **2010**, *1234*, 343-346.
- (38) Kasrai, M.; Yin, Z.; Bancroft, G. M.; Tan, K. H.; *J. Vac. Sci. Technol., A* **1993**, *11*, 2694.
- (39) Altman, A. B.; Pemmaraju, C. D.; Camp, C.; Arnold, J.; Minasian, S. G.; Prendergast, D.; Shuh, D. K.; Tyliczszak, T.; *J. Am. Chem. Soc.* **2015**, *137*, 10304-10316.
- (40) Tremont, R. J.; Cruz, G.; Cabrera, C. R.; *J. Electroanal. Chem.* **2003**, *558*, 65-74.
- (41) Singh, J.; Whitten, J. E.; *J. Phys. Chem. C* **2008**, *112*, 19088-19096.
- (42) Lin, L.-H.; Wu, C.-C.; Lai, C.-H.; Lee, T.-C.; *Chem. Mater.* **2008**, *20*, 4475-4483.
- (43) Niedziolka, J.; Palys, B.; Nowakowski, R.; Opallo, M.; *J. Electroanal. Chem.* **2005**, *578*, 239-245.
- (44) Masitas, R. A.; Khachian, I. V.; Bill, B. L.; Zamborini, F. P.; *Langmuir* **2014**, *30*, 13075-13084.
- (45) Hu, M.; Suguru, N.; Okubo, T.; Yamaguchi, Y.; Komiyama, H.; *Appl. Surf. Sci.* **2001**, *181*, 307-316.
- (46) Oyama, M.; Orimo, A.; Nouneh, K.; *Electrochim. Acta* **2009**, *54*, 5042-5047.
- (47) Khoshmashrab, S.; Turnbull, M. J.; Vaccarello, D.; Nie, Y.; Martin, S.; Love, D. A.; Lau, P. K.; Sun, X.; Ding, Z.; *Electrochim. Acta* **2015**, *162*, 176-184.
- (48) Vaccarello, D.; Hedges, J.; Tapley, A.; Love, D. A.; Ding, Z.; *J. Electroanal. Chem.* **2015**, *738*, 35-39.
- (49) Schaming, D.; Hojeij, M.; Younan, N.; Nagatani, H.; Lee, H. J.; Girault, H. H.; *Phys. Chem. Chem. Phys.* **2011**, *13*, 17704-17711.
- (50) Jalilehvand, F.; *Chem. Soc. Rev.* **2006**, *35*, 1256-1268.
- (51) Bär, M.; Nishiwaki, S.; Weinhardt, L.; Pookpanratana, S.; Fuchs, O.; Blum, M.; Yang, W.; Denlinger, J. D.; Shafarman, W. N.; Heske, C.; *Appl. Phys. Lett.* **2008**, *93*, 244103.

- (52) Zhou, X.; Heigl, F.; Ko, J.; Murphy, M.; Zhou, J.; Regier, T.; Blyth, R.; Sham, T.; *Phys. Rev. B* **2007**, *75*, 125303 125301-125308.
- (53) Yamazoe, S.; Kou, H.; Wada, T.; *J. Mater. Res.* **2011**, *26*, 1504-1516.
- (54) Figueiredo, M. O.; Da Silva, T. P.; *Eur. J. Mineral.* **2009**, *21*, 79-83.
- (55) Pin, S.; Huthwelker, T.; Brown, M. A.; Vogel, F.; *J. Phys. Chem. A* **2013**, *117*, 8368-8376.
- (56) Grioni, M.; Goedkoop, J. B.; Schoorl, R.; de Groot, F. M. F.; Fuggle, J. C.; Schäfers, F.; Koch, E. E.; Rossi, G.; Esteva, J. M.; Karnatak, R. C.; *Phys. Rev. B* **1989**, *39*, 1541-1545.
- (57) Van der Laan, G.; Patrick, R. A. D.; Henderson, C. M. B.; Vaughan, D. J.; *J. Phys. Chem. Solids* **1992**, *53*, 1185-1190.
- (58) Vegelius, J. R.; Kvashnina, K. O.; Hollmark, H.; Klintonberg, M.; Kvashnin, Y. O.; Soroka, I. L.; Werme, L.; Butorin, S. M.; *J. Phys. Chem. C* **2012**, *116*, 22293-22300.
- (59) Pearce, C. I.; Patrick, R. A. D.; Vaughan, D. J.; Henderson, C. M. B.; van der Laan, G.; *Geochim. Cosmochim. Acta* **2006**, *70*, 4635-4642.
- (60) Todd, E. C.; Sherman, D. M.; Purton, J. A.; *Geochim. Cosmochim. Acta* **2003**, *67*, 2137-2146.
- (61) Johnson, B.; Klaer, J.; Merdes, S.; Gorgoi, M.; Höpfner, B.; Vollmer, A.; Lauer mann, I.; *J. Electron. Spectrosc. Relat. Phenom.* **2013**, *190*, 42-46.
- (62) Collins, B. A.; Cochran, J. E.; Yan, H.; Gann, E.; Hub, C.; Fink, R.; Wang, C.; Schuettfort, T.; McNeill, C. R.; Chabiny, M. L.; Ade, H.; *Nat. Mater.* **2012**, *11*, 536-543.
- (63) Bondino, F.; Vesselli, E.; Baraldi, A.; Comelli, G.; Verdini, A.; Cossaro, A.; Floreano, L.; Morgante, A.; *J. Chem. Phys.* **2003**, *118*, 10735-10740.
- (64) Tomson, N. C.; Williams, K. D.; Dai, X.; Sproules, S.; DeBeer, S.; Warren, T. H.; Wieghardt, K.; *Chem. Sci.* **2015**, *6*, 2474-2487.
- (65) Penner-Hahn, J. E., *X-ray Absorption Spectroscopy*. Elsevier: 2003; Vol. 2, p 159-18

## 5 Effect of Annealing on the Photoelectrochemical Behaviour of CuInS<sub>2</sub> Nanocrystal Films

(A version on this work is presented in Journal of Electrochemical Society. Tapley, A.; Hart, C.; Vaccarello, D.; Love, D. A.; Ding, Z.; *J. Electrochem. Soc.* **2014**, *161*, H725-H729)

### 5.1 Introduction

The demand for a renewable, cost-effective, green energy source is constantly increasing. Solar energy has the potential to aid in meeting the demand if the cost of solar cell fabrication can be kept down without sacrificing efficiency. Inorganic thin-film based photovoltaics may be able to overcome the high cost of their silicon counterparts while maintaining a comparable efficiency.<sup>1-3</sup> One such material is CuInS<sub>2</sub> (CIS) which is under investigation here. It has a high absorption coefficient ( $10^5 \text{ cm}^{-1}$ ), an optimal band gap of approximately 1.5 eV, and has shown laboratory efficiencies as high as 12 %.<sup>4-6</sup>

CIS devices with higher efficiencies often require the nanocrystals (NCs) to undergo a high-temperature treatment at roughly 500 °C; often accompanied by a H<sub>2</sub>S atmosphere.<sup>1, 7, 8</sup> These procedures not only increase the energy input required to manufacture solar cells and drive up the monetary cost of the devices, but are also hazardous to implement. Work is being done to remove these steps while preserving efficiency, but it appears the annealing step may be unavoidable.<sup>1, 4, 6</sup> Solution-based processing such as inks and precursor solutions are being employed to keep the sulfur content high.<sup>5-7, 9</sup> However, it often necessitates the high-temperature annealing step, which requires an inert atmosphere, a H<sub>2</sub>S gas flow, a Schlenk line, and/or toxic solvents.<sup>4, 5, 8, 9</sup>

Annealing is such an ingrained step in CIS device making that it is often not a topic of discussion, but rather an accepted practice. The cost of the CIS absorber layer could be reduced by either lowering the annealing temperature or removing it completely.<sup>9-11</sup> CIS NCs were synthesized here using a one-pot method that involved no post processing other than an acetone rinse,<sup>12</sup> but one cannot disregard the benefits of a high temperature treatment. Removing the capping ligand, impurities, and/or increasing crystallinity of the

CIS might benefit the device efficiency.<sup>13</sup> Annealing the NCs, although expensive in industry, may be a necessity if it increases the photocurrent of the absorber layer significantly. This study explored the effects of annealing based on photoelectrochemical (PEC) measurements. The CdS buffer layer is typically added after annealing because temperatures above 300 °C will degrade optical properties.<sup>14</sup> The addition of the CdS buffer layer along with the annealing on the photoconversion of the NC films was also investigated.

The surface morphology, crystallinity, and elemental ratios were inspected using scanning electron microscopy (SEM), thin film X-ray diffraction (XRD), energy dispersive x-ray spectroscopy (EDX), and X-ray photoelectron spectroscopy (XPS). Intensity modulated photocurrent spectroscopy (IMPS) was used to investigate the relative photoreaction rates.

## 5.2 Experimental

CIS was synthesized using the previously reported one-pot synthesis.<sup>12</sup> Briefly, the metal precursor salts were copper(II) acetylacetonate (97%, Sigma-Aldrich, St. Louis, MO) and indium(III) acetylacetonate (99.99%, Sigma-Aldrich, St. Louis, MO) in a molar ratio of 0.98 Cu/In. Thiourea (99.0%, Fluka, Mississauga, ON) was the source of sulfur with a molar ratio of 8.5 S/Cu. The capping ligand 2-mercapto-5-propylpyrimidine (MPP, 98%, Alfa Aesar, Ward Hill, MA) was added in a ratio of 3.31 to Cu. The CIS NCs dispersion in acetone was dropcast onto a 10.02 mm<sup>2</sup> area of a conductive substrate in two 6 µL drops allowing for the dispersion to dry in between drops.

CdS was deposited on the CIS NC film via chemical bath deposition. The bath employed was based on a previous method.<sup>15</sup> It involved 1.5 mM CdSO<sub>4</sub> (Fischer Scientific, Fair Lawn, NJ), 1.5 M NH<sub>4</sub>OH (Caledon, Georgetown, ON) and 7.5 mM thiourea in water. The CdSO<sub>4</sub> and NH<sub>4</sub>OH were stirred for approximately 30 mins at room temperature, placed in a 60 °C bath, and allowed to heat for 5 mins before the addition of thiourea. After allowing the solution to react for 8 mins, the NC films on indium tin oxide (ITO) were lowered into the bath for 8 mins. The resulting film was gently rinsed with DI water and allowed to air dry.

PEC measurements were carried out by immersing the conductive substrate coated with the NC film in 0.03 M methyl viologen ( $MV^{2+}$ ) dichloride, (Sigma-Aldrich, 98%) and 0.1 M KCl (Sigma-Aldrich, 99.0%) solution. A saturated calomel electrode and a platinum coil were used as the reference and counter electrode, respectively. The light source was a 150 W Newport lamp with an AM 1.5D filter. A ThorLabs SC10 shutter was used to produce a square wave light stimulus to the system. Electrochemistry was performed using a CHI 832a electrochemical analyzer. A linear potential sweep was applied from 0.0 to -0.4 V at a scan rate of 5 mV/s.<sup>12, 15</sup>

CIS NCs dropcast onto ITO, molybdenum glass, or plain glass were annealed using a Thermoscientific Lindberg Blue M Tube Furnace under an inert argon atmosphere. XRD patterns of the NC films drop cast on plain glass were obtained using an Inel CPS Powder Diffractometer with an Inel XRG 3000 Cu X-ray generator, and an Inel CPS 120 detector. IMPS was performed on the film in a similar electrochemical cell as in the PEC measurements using an IVIUM CompactStat instrument and a 4.0 V IVIUM ModuLight light source (LED), which emitted 488 mW white light with a frequency sweep from 10000 Hz to 0.01 Hz. SEM was performed using a Hitachi S-4500 field emission microscope with an EDX system at 10.0 kV. The CIS NCs were placed in a vacuum oven at 60 °C for four hours, and the thermogravimetric analysis (TGA) was carried out in a nitrogen atmosphere using a Mettler Toledo TGA/SDTA851<sup>e</sup> analyzer with a temperature sweep from 25 to 500 °C at a rate of 10 °C/min.

### 5.3 Results and Discussions

Our previously optimized recipe and synthetic strategy of CIS NCs involved no post-processing and only employed an acetone rinse as a means of removing impurities.<sup>12</sup> This produced a material that showed a relatively large photocurrent. Annealing was avoided in an effort to reduce the costs of possible industrial fabrication. However, upon annealing, NCs produced a film with a significantly higher photocurrent. It may be worthwhile for the annealing to be included as a post-processing step.

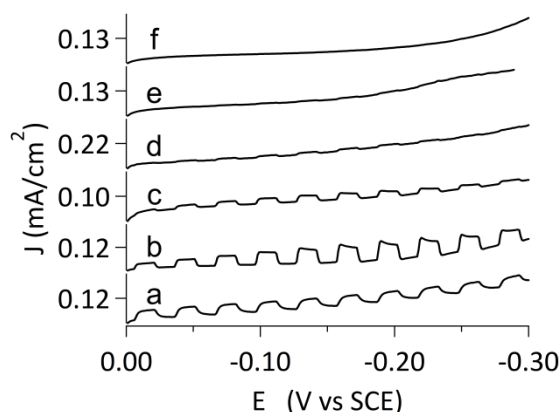


**Figure 5.1 Photoelectrochemical measurements in 0.03 M methyl viologen of annealed CIS NCs films at a) unaltered, b) 250 °C, c) 300 °C, d) 350 °C, e) 400 °C and f) 500 °C.**

The optimal annealing temperature was investigated by heating samples in 50 °C intervals between 250 and 500 °C (Figure 5.1). The effect of the heat treatment on the quality of the NCs was judged using PEC measurements. A large difference between the dark current and photocurrent was the deciding factor on what conditions were beneficial for the NCs. The NCs were synthesized, dispersed in acetone, and dropcast on to ITO glass or molybdenum coated glass. There was a photocurrent enhancement at 250 °C (as shown in Figure 5.1) from 0.03 mA/cm<sup>2</sup> to 0.08 mA/cm<sup>2</sup> at -0.13 V. After this initial increase the photocurrent decreased with increasing temperature. The literature value for a CIS NC film using the same PEC measurement technique described here puts the photocurrent density at -0.13 V as 0.05 mA/cm<sup>2</sup>.<sup>3</sup> Photocurrent was still produced by the films annealed at 300 and 350 °C, but the photocurrent density was less than that produced by the unaltered film. CIS films annealed at temperatures above 350 °C produced no photocurrent in the PEC measurement. The decreased photocurrent at temperatures above 300 °C is contradictory to those in other reports where temperatures ranging from 400 to 550 °C were used.<sup>15, 16</sup> In fact, it was reported that heat treatment was needed to remove carbon impurities, increase crystal size, and sinter (or in some cases actually form) CIS from a mixture of individual salts.<sup>4, 10, 17</sup> The removal of the oleyamine (OLA) capping ligand used in typical syntheses is largely the reason why



annealing was employed. OLA is an insulating ligand, but it caps the NCs to produce and facilitate in size control.<sup>6</sup> Its removal is integral to achieving a worthwhile efficiency.<sup>6, 13</sup> The synthesis used by Ye et al. involved an oxygen-free atmosphere, OLA as a capping ligand, temperatures of 240 °C to form the NCs, and annealing temperatures of 400 °C to remove the OLA. The one-pot method utilized here, however, used a different capping ligand: MPP. This relatively short-chain ligand contains a pyrimidine ring and an exposed sulfur atom, which can coordinate to the surface of the NCs.<sup>13</sup> It has previously been postulated that the pyrimidine ring in the MPP helped to facilitate electron transport in the material, which renders its removal unnecessary.<sup>12, 13</sup> In light of the annealed CIS PEC measurements, it is apparent that not only is the removal of MPP not necessary, but actually detrimental to the quality of the materials. This may be due to the incomplete degradation of the organic material leading to increased surface resistance.<sup>9</sup> The one-pot synthesis produced NCs with photocurrent densities that are similar to that of Ye *et. al.* while avoiding high-cost techniques that were used to produce their films.

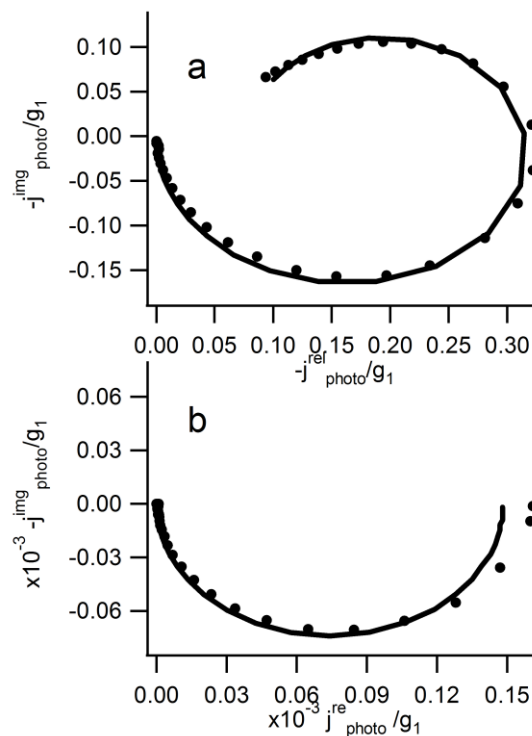


**Figure 5.2 IMPS at open circuit potential of a) the unaltered film and b) the film annealed at 250 °C**

Photocurrent enhancement was not the only positive effect annealing had on the CIS films. IMPS was used to investigate the relative rate constants associated with the recombination or separation of the photogenerated electron. Based on the recombination rate ( $k_r$ ) to product separation rate ( $k_{ps}$ ) ratio, a full circle is seen for a very high  $k_r$ , a semicircle for a high  $k_{ps}$ , and a spiral for ratios in between.<sup>18</sup> IMPS of the unaltered and annealed films at open circuit potential are shown in Figure 5.2 and indicated that annealing severely reduced the film's recombination rate. The unaltered film has an intermediate  $k_r/k_{ps}$  value, whereas the annealed film has a very small  $k_r/k_{ps}$  value. Not only did annealing at 250 °C increase the photocurrent, but also the favourability of the photoreaction rates between the film and the electrolyte.

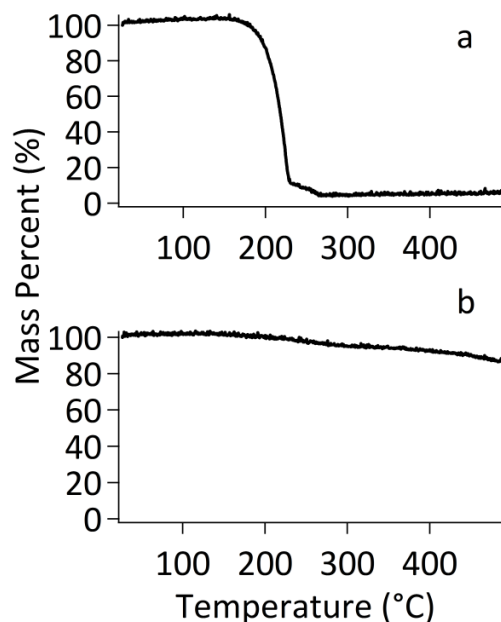


**Figure 5.3 Thermogravimetric analysis of a) the capping ligand MPP and b) CIS**

The relationship between MPP loss and temperature was investigated further to give insight into why 250 °C was the optimal temperature. The TGA results shown in Figure 5.3a is the analysis of MPP alone. The mass loss began slightly above 200 °C and ceased just above 250 °C. The significant mass loss onset corresponds to the melting point of MPP (207-211 °C). These results do not initially correlate with the PEC-measurement-determined optimal-annealing temperature of 250 °C, as all the capping ligand (and its associated benefits) would be gone. The TGA of the one-pot CIS was performed to investigate the stability of the MPP-capped NCs during the heat treatment and can be seen in Figure 5.3b. The overall mass loss was 14 %, and the start of mass loss for the NCs began around 208 °C, which also corresponds with the melting point of MPP. The loss was over a larger temperature range than that of MPP alone suggesting that MPP's interaction with the NCs may provide stabilization at higher temperatures. Loss of some MPP is inevitable at temperatures higher than its melting point although its interaction with the CIS NCs may slow its loss, especially at the lower optimal annealing temperature determined here. The annealing temperature of 250 °C does cause some MPP loss, but balances it out with other benefits that will be described later.

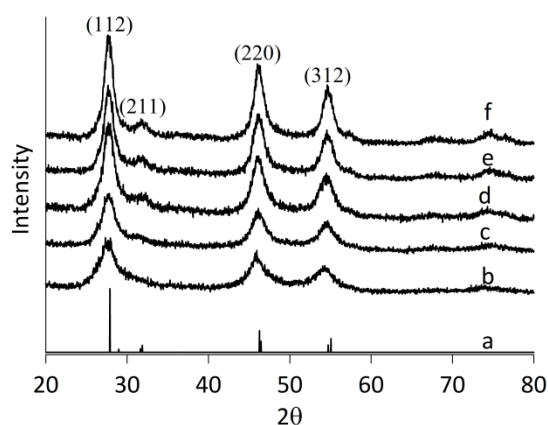


**Figure 5.4 XRD of the CIS NC films a) JCPDS card No. 01-085-1575 for CIS b) unaltered, c) 250 °C, d) 300 °C, e) 400 °C, f) 500 °C.**

The loss of MPP was also investigated with XPS and EDX. The respective surface and bulk sensitive techniques were used to probe the elemental composition of the films. The results of the nitrogen and carbon content determined by both EDX and XPS are listed in Table 5.1. The Cu, In and S ratios all remained similar. Nitrogen content was probed because it is exclusive to MPP. A loss of MPP in the bulk is supported by the roughly linear drop in the carbon weight percent revealed by the EDX results as the annealing temperature was increased. Similar trends are seen in the nitrogen and carbon content at the surface. The carbon content at the surface was larger than in the bulk because of the air contaminants; another reason why carbon was not solely used to track the MPP content. The surface carbon on an NC film that exhibits photocurrent remains roughly the same, while the nitrogen content decreased with increasing temperature. The loss of nitrogen suggested the removal of MPP from the NCs and thus a decreased photocurrent from the films.

**Table 5.1 Carbon and nitrogen weight percent results for the annealed films**

<b>Anneal temperature (°C)</b>	<b>EDX Carbon weight (%)</b>	<b>XPS Carbon weight (%)</b>	<b>XPS Nitrogen weight (%)</b>	<b>NC Size from XRD (nm)</b>
<b>No anneal</b>	11.1	16.2	2.6	3.8
<b>250</b>	10.3	16.4	1.3	4.4
<b>300</b>	8.02	16.6	1.8	4.5
<b>400</b>	7.7	12.5	1.2	5.6
<b>500</b>	6.5	11.2	0.7	6.4

The effects of annealing on the NC size and crystallinity were investigated using XRD. The XRD patterns at the varied furnace temperatures are shown in Figure 5.4. The observed peaks matched well with the chalcopyrite structure of CIS (JCPDS card No. 01-085-1575). The intensity of the peaks increased, and the peak widths decreased, as the temperature of annealing was augmented. These observations are caused by several different factors including an elevated crystallinity, an increase in NC size, and/or an overall increase in the order of the NCs.<sup>5</sup> Increased order and crystallinity were further supported by the appearance of the less intense (211) peak at  $2\theta = 32^\circ$ . Decreased peak width is also indicative of an increased NC size. The Debye-Scherrer equation (equation 6.1) allowed the theoretical NC sizes to be calculated, which are shown in Table 5.1. The NCs increased in size with increased annealing temperature.

$$D = \frac{0.9\lambda}{B(2\Theta)\cos\Theta} \quad (6.1)$$

Before annealing, the calculated size was approximately 3.8 nm, which then increased to 6.4 nm when annealed at 500 °C. The general findings of this work have been reported

before for CIS prepared from a precursor paste.<sup>5</sup> However, the annealing temperature that produced a film with the best photovoltaic properties was 450 °C<sup>5</sup>, which is significantly higher than the 250 °C optimized temperature discovered here.

The morphology of the different NC films were imaged using SEM. Low-magnification images revealed that, the frequency and severity of cracks in the film increased dramatically with the annealing temperature. Cracks greatly inhibit electron flow throughout the material, and likely contribute to the diminished photocurrent.<sup>11</sup> With samples heated to 250 °C, attempts were made to fill the cracks with additional CIS by dropcasting another layer of CIS onto the surface after heating and annealing a second time. A PEC measurement of each step was taken, some of which are shown in Figure 5.5. When a second layer of CIS was added to the annealed NCs, the photocurrent returned to the current density of the original unaltered CIS (Figure 5.5d, blue). It was discovered that annealing a second time only reduced the photocurrent and increased the resistivity of the film (Figure 5.5c, green). Dropcasting another layer of CIS on the annealed film may have filled the cracks, but it blocked annealed film from contact with the redox species returning the photocurrent density to that of unaltered CIS, and canceling out any benefits annealing had on the film. Annealing the film a second time may have increased the photocurrent density, but it also dramatically increased the film's resistivity making it unsuitable for use in a solar cell.

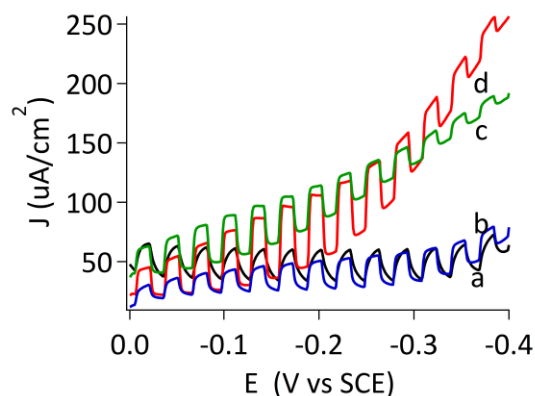


**Figure 5.5** Photoelectrochemical measurements of a) unaltered CIS (black), b) annealed CIS with a second CIS layer (blue) c) annealed CIS with a second layer of CIS annealed again (green) and d) annealed CIS (red).

Higher magnification SEM images (Figure 5.6) illustrate little difference between the NC clusters at the two different furnace temperatures. When compared to the unannealed CIS (Figure 5.6a) the clusters decreased in size and, the density of the clusters appeared to increase after annealing. The above observations from the SEM images coincided with those made by others upon annealing  $\text{CuInSe}_2$ .<sup>5, 19</sup> The increased cluster density can account for the photocurrent enhancement obtained from annealing. Closer NC cluster packing would decrease the gaps between the neighbouring clusters, which would otherwise hinder electrons from passing through the material easily. The density of the clusters between the 250 °C and 500 °C samples does not appear to increase significantly. Temperatures greater than 250 °C do not affect the packing or size of the one-pot unaltered NCs appreciably and thus offer no benefits to the film's performance in this way. Morphologically speaking, the benefits of annealing the film are outweighed by the severe cracks that occur when the NC film is annealed at temperatures above 250 °C.

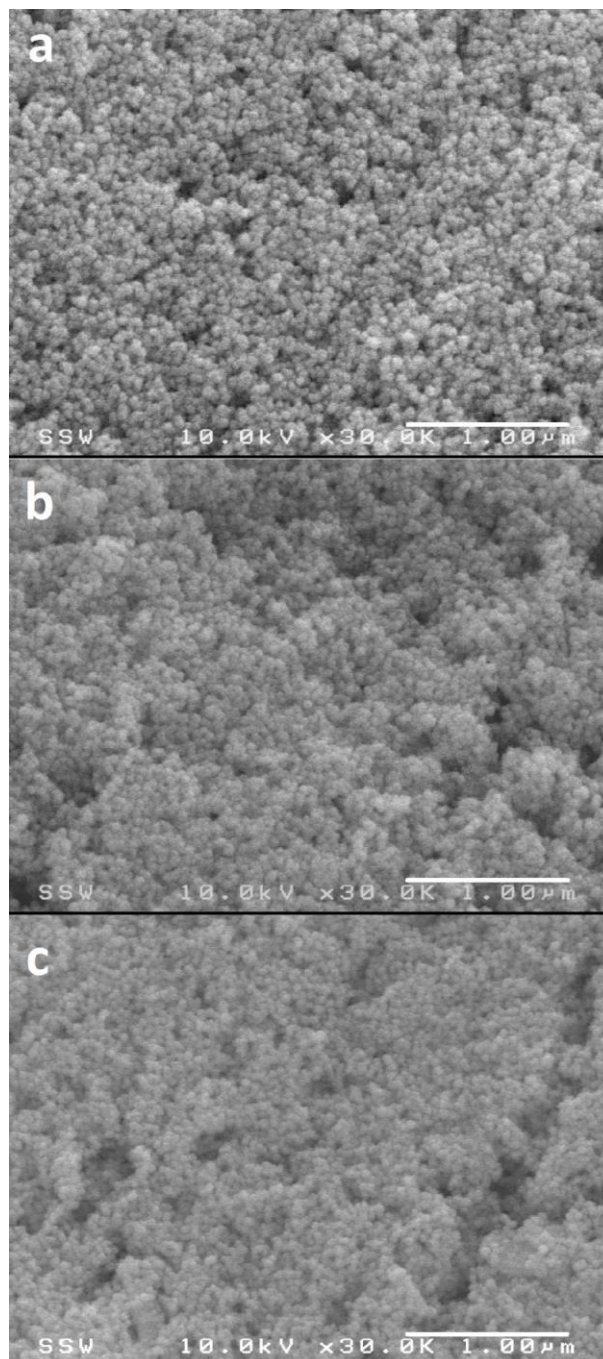


**Figure 5.6 SEM images of a) unaltered CIS, b) annealed at 250 °C c) annealed at 500 °C.**

Annealing at 250 °C also allows for the heat processing of CIS and CdS layers to be performed simultaneously. The low temperature also enabled the use of ITO on glass as a substrate since it does not degrade at that temperature. Both ITO and CdS performance



have been shown to worsen when subject to temperatures at or above 300 °C.<sup>14, 20</sup> The PEC measurements in Figure 5.7 show an enhancement after annealing the two layers together, as well as a small value for the dark current. The causes of the enhancement could be attributed to increased lattice matching of the two layers, Cd diffusion into the CIS film, or the development of Cd-In-S phases.<sup>21, 22</sup> When a second layer of CdS was deposited after annealing, a significant enhancement was obtained. The largest photocurrent enhancement occurred at -0.22 V.

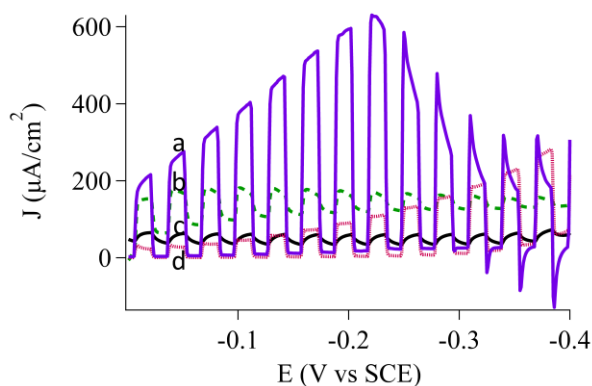


**Figure 5.7 Photoelectrochemical measurements of thin films of a) CIS/CdS (A)/CdS (purple), b) CIS/CdS (green), c) CIS (black), d) CIS/CdS(A) (red) where (A) denotes an annealed sample.**

The photocurrent density of the CIS/CdS(A)/CdS champion sample was measured at that point to be approximately 14.7 times larger than that of the original CIS layer alone. This second CdS layer may have filled in any cracks that occurred during the heat treatment, as well as deposited CdS onto areas that may have been initially lacking in thickness. Subsequent heating of the material also caused a diminished photocurrent.

## 5.4 Conclusion

A 250 °C annealing step provided a photocurrent enhancement as well as increased the  $k_{ps}$  for the CIS NC thin films. Higher annealing temperatures reduced the photocurrent. The reduction of the photocurrent could have been due to cracking and a loss of the electron flow support provided by the capping ligand. The low-temperature annealing

enabled the CdS layer to be added to the CIS before heating, which produced enhancement when compared to only adding CdS. A second layer of CdS deposited after the heat treatment increased the photocurrent further. This may be the result of crack filling and more even distribution of the CdS layer.

Annealing the one-pot synthesized CIS alone does not provide a sufficient photocurrent enhancement to justify its incorporation into the post-synthesis. However, low-temperature annealing of the CIS NC and CdS layers together, along with the deposition of a secondary CdS layer, yielded a 14.7 times increase in the photocurrent. This layer-by-layer approach of constructing a thin-film CIS solar cell gives insight into the conditions for optimal, scalable, absorbing layer and buffer layer deposition at low costs. The marked increase in photocurrent justifies the use of a low-temperature annealing post-process. These findings can further reduce fabrication costs on multiple levels making CIS a more viable option for dealing with the ongoing energy crisis.

## 5.5 References

- (1) Cho, J. W.; Park, S. J.; Kim, J.; Kim, W.; Park, H. K.; Do, Y. R.; Min, B. K.; *ACS Appl. Mater. Interface* **2012**, *4*, 849-853.
- (2) Chassaing, E.; Grand, P. P.; Ramdani, O.; Vigneron, J.; Etcheberry, A.; Lincot, D.; *J. Electrochem. Soc.* **2010**, *157*, D387-D395.
- (3) Huang, Q.; Reuter, K.; Amhed, S.; Deligianni, L.; Romankiw, L. T.; Jaime, S.; Grand, P. P.; Charrier, V.; *J. Electrochem. Soc.* **2011**, *158*, D57-D61.
- (4) Liu, W.; Mitzi, D. B.; Yuan, M.; Kellock, A. J.; Chey, S. J.; Gunawan, O.; *Chem. Mater.* **2010**, *22*, 1010-1014.
- (5) Xu, J.; Wang, Y.; *Mater. Lett.* **2013**, *99*, 90-93.
- (6) Panthani, M. G.; Akhavan, V.; Goodfellow, B.; Schmidtke, J. P.; Dunn, L.; Dodabalapur, A.; Barbara, P. F.; Korgel, B. A.; *J. Am. Chem. Soc.* **2008**, *130*, 16770-16777.
- (7) Guo, Q.; Ford, G. M.; Hillhouse, H. W.; Agrawal, R.; *Nano Lett.* **2009**, *9*, 3060-3065.
- (8) Guo, Q.; Kim, S. J.; Kar, M.; Shafarman, W. N.; Birkmire, R. W.; Stach, E. A.; Agrawal, R.; Hillhouse, H. W.; *Nano Lett.* **2008**, *8*, 2982-2987.

- (9) Lim, Y. S.; Jeong, J.; Kim, J. Y.; Ko, M. J.; Kim, H.; Kim, B.; Jeong, U.; Lee, D.-K.; *J. Phys. Chem. C* **2013**, *117*, 11930-11940.
- (10) Hou, W. W.; Bob, B.; Li, S.-h.; Yang, Y.; *Thin Solid Films* **2009**, *517*, 6853-6856.
- (11) Weil, B. D.; Connor, S. T.; Cui, Y.; *J. Am. Chem. Soc.* **2010**, *132*, 6642-6643.
- (12) Tapley, A.; Vaccarello, D.; Hedges, J.; Jia, F.; Love, D. A.; Ding, Z.; *Phys. Chem. Chem. Phys.* **2013**, *15*, 1431.
- (13) Talapin, D. V.; Lee, J.-S.; Kovalenko, M. V.; Shevchenko, E. V.; *Chem. Rev.* **2009**, *110*, 389-458.
- (14) Mahdi, M. A.; Kasem, S. J.; Hassen, J. J.; Swadi, A. A.; l-Ani, S. K. J. A.; *Int. J. Nanoelectron. Mater.* **2009**, *2*, 163-172.
- (15) Ye, H.; Park, H. S.; Akhavan, V. A.; Goodfellow, B. W.; Panthani, M. G.; Korgel, B. A.; Bard, A. J.; *J. Phys. Chem. C* **2011**, *115*, 234-240.
- (16) Brini, R.; Kanzari, M.; Rezig, B.; J.Werckmann; *Eur. Phys. J. Appl. Phys.* **2005**, *30*, 153-158.
- (17) Huang, W.-C.; Tseng, C.-H.; Chang, S.-H.; Tuan, H.-Y.; Chiang, C.-C.; Lyu, L.-M.; Huang, M. H.; *Langmuir* **2012**, *28*, 8496-8501.
- (18) Fermin, D.; Duong, H.; Ding, Z.; Brevet, P.; Girault, H.; *Phys. Chem. Chem. Phys.* **1999**, *1*, 1461-1467.
- (19) Lee, J. Y.; Ryu, S. O.; Lee, T. J.; Ryu, S. O.; *Mol. Cryst. Liq. Cryst.* **2012**, *564*, 147-154.
- (20) Li-jian, M.; Maçarico, A.; Martins, R.; In *Study of annealed indium tin oxide films prepared by rf reactive magnetron sputtering*, MRS Spring Meeting, Monte da Caparica, Portugal, Elsevier Science Ltd: Monte da Caparica, Portugal, 1995.
- (21) Lei, B.; Hou, W. W.; Li, S.-H.; Yang, W.; Chung, C.-H.; Yang, Y.; *Sol. Energy Mater. Sol. Cells* **2011**, *95*, 2384-2389.
- (22) Ramanathan, K.; Bhattacharya, R.; Granata, J.; Webb, J.; Niles, D.; Contreras, M.; Wiesner, H.; Hasoon, F.; Noufi, R.; In *Advances in the CIS Research at NREL*, 26th IEEE PVSC, Anaheim, California, Anaheim, California, 1997.

## 6 Electrochemical Deposition of Light-absorbing $\text{CuInSe}_2$ for use in Solar Cells

### 6.1 Introduction

$\text{CuInSe}_2$  (CISE) is a light-absorbing semiconductor that can be utilized in thin-film inorganic solar cells. Its high absorption coefficient and direct band gap make it an ideal candidate for solar cells.<sup>1</sup> The major goal in commercializing solar cells is to achieve a high efficiency while keeping the associated costs low. CISE solar cells have achieved efficiencies of 14.5 %, but this efficiency requires a multi-step, high-temperature process.<sup>2</sup> To commercialize CISE-based solar cells an inexpensive and scalable technique is required.

Electrochemical deposition (ECD) is an inexpensive, scalable, low-waste process that is already used commercially.<sup>3</sup> If it can be optimized to produce CISE films that are free of defects and secondary phases it would drastically reduce the cost associated with CISE solar cells. ECD also may have advantage over CISE nanocrystal-based solar cells as it directly forms the light-absorbing film, whereas two steps are needed for the nanocrystals: preparation and film formation.<sup>4-6</sup> Typically, the co-deposition of Cu, In, and Se is carried out simultaneously to form the CISE film.<sup>7-12</sup> However, this technique needs a complexing agent to adjust the reduction potential of the elements, which can be difficult to tune and can increase impurities in the film.<sup>10-15</sup> Sequential deposition of the metals followed by a selenization/annealing process is beneficial to the films. The optimal conditions for the deposition of each metal and the subsequent selenization are more easily obtained to form the ideal CISE light-absorbing layer.

In this work, the starting ratio of the metallic Cu/In stack and subsequent selenization were optimized using photoelectrochemical (PEC) measurements. Samples that exhibited the best properties were then fully characterized to elucidate further their feasibility for creating a high-efficiency solar cell. They were characterized with respect to morphology, composition, and structure to determine if selenization of the metallic stacks

could produce CISE films with all the necessary qualities to be an ideal light-absorbing layer for solar cells.<sup>13</sup>

The inclusion of sulfur to form  $\text{CuIn}(\text{S}_x\text{Se}_{1-x})_2$  (CISSe) can tune the band gap of the CISE to a higher value, making it closer to the ideal 1.4 eV.<sup>16</sup> This can increase the open circuit potential and the efficiency of the solar cell.<sup>16</sup> CISSe is a quaternary compound, so there is great potential for deviations in stoichiometry and variance in the conductivity.<sup>13</sup> Preliminary results were obtained on the CISE samples annealed with selenium and some residual sulfur from the furnace tube. In addition to conventional characterizations, synchrotron radiation was used to investigate how the sulfur incorporates into the CISE. X-ray absorption fine structure (XAFS) using synchrotron radiation is a powerful tool for determining coordination chemistry, oxidation state, distances, and species of the neighbours to the absorbing atom.<sup>17</sup> X-ray absorption near edge structure (XANES) and extended X-ray absorption fine structure (EXAFS) were both used to determine the effect the sulfur has on the CISE lattice and film upon incorporation.

## 6.2 Experimental

### 6.2.1 $\text{CuInSe}_2$ Fabrication

CISE thin films were fabricated using sequential electrochemical bath deposition of the copper and indium followed by a selenization process. Copper was deposited from a solution containing 25 g/L  $\text{CuSO}_4 \cdot 5\text{H}_2\text{O}$  (99.995%, Sigma Aldrich), 120 g/L NaOH (97% pellets, Sigma Aldrich) and 37.5 g/L D-sorbitol ( $\geq 98\%$ , Sigma Aldrich).<sup>18</sup> Indium was deposited from an indium sulfamate solution purchased from the Indium Corporation (Clinton, NY). The manufacturer recommended deposition parameters for a film with small nucleation sites were used.

Mo-coated glass was purchased from University Wafer (Boston, MA) with a 500 Å Mo-thickness. It was cleaned with 2% Hellmanex, DI water, acetone and ethanol sonicating for 5 mins at each step. Copper was deposited using an alkaline/mercurous oxide as the reference electrode, Pt mesh for the counter, and the Mo-coated glass as the working electrode. The deposition was carried out using an EG&G Princeton Applied Research Model 363 Potentiostat (Oakridge, TN) at 2.5 mA/cm<sup>2</sup> for 90 sec. Indium was deposited

using 11 mA/cm<sup>2</sup> applied to the copper-coated Mo-glass as the working electrode and indium as the counter electrode. The deposition times of indium were varied between 24 to 110 sec to achieve different Cu/In ratios between 0.3 and 1.4.<sup>19</sup> These ratios were calculated using Faraday's law and assuming 100 % efficiency for the copper deposition and 90 % efficiency for the indium deposition.

The annealing and selenization processes were carried out on the stacked precursor films in a quartz tube in a Thermoscientific Lindberg Blue M tube furnace (Asheville, NC). The samples were placed on a graphite stage next to an open graphite box with the selenium powder. Three amounts of Se were chosen: 3 mg/cm<sup>2</sup>, 5mg/cm<sup>2</sup> and 10 mg/cm<sup>2</sup>. These values were chosen based on previous work on the related compound Cu<sub>2</sub>ZnSn(S,Se)<sub>4</sub>.<sup>20</sup> The tube was then purged of oxygen via five vacuum and refill cycle with argon. The pressure of the argon was set at 0.62 bar. The annealing and selenization processes were based on previous work reported by Lee *et al.*<sup>21</sup> The temperature was ramped up to 250 °C and held there for 20 mins, and then it was increased to 550 °C for 10 mins. The ramp rate was 60 °C/min, and the system was then allowed to cool naturally.

## 6.2.2 Fabrication of Full Solar Cells

CdS was added via a chemical bath deposition. The solution was prepared using Milli-Q water (Millipore Corporation, 18.2 MΩ cm), 1.8 mM of CdCl<sub>2</sub> (Sigma-Aldrich, 99.99%), 1.02 M NH<sub>4</sub>OH (Caledon, ≥99 %) , and 7.3 mM of thiourea (Sigma-Aldrich, ≥99%). The CdCl<sub>2</sub>, NH<sub>4</sub>OH, and water were allowed to stir for 30 mins. The solution was then heated to 70 °C. The thiourea and CISE film samples were added to the bath. The solution was allowed to react for 8 minutes. The samples were then removed from the bath and rinsed thoroughly with Milli-Q water. They were then placed in the tube furnace and heated to 60 °C under vacuum for 12 hours to remove any water.

ZnO and Al-doped ZnO (Al:ZnO) were added using an Ultratech/Cambridge Nanotech Savannah S200 atomic layer deposition (ALD) instrument (Waltham, MA). The deposition processes used were based on the manufacturer's recommended processes. The sample chamber was pumped down to 2.6 x 10<sup>-4</sup> atm following a purge with 5 sccm

of medical grade N<sub>2</sub> (Praxair, 99.999 %), and then allowed to equilibrate for 5 minutes. The ZnO deposition was done at 200 °C, and was completed using 0.15 s pulses of diethylzinc (Strem Chemical, min 95 %) and Milli-Q water with an 8 s wait time between pulses. This created a rate of 1.6 Å growth/cycle, and 50 nm of ZnO was deposited. For the Al:ZnO, the aluminium source was trimethylaluminium (Strem Chemicals, min. 98%). This involved a macrocycle of three smaller cycles all performed at 200 °C. Within the macrocycle, the first step was depositing 10 cycles of ZnO using the procedure described above. Then there was a 0.15 s pulse of the trimethylaluminium followed by a 0.15 s pulse of Milli-Q water, and then an 8 s delay. Then another 10 cycles of ZnO were deposited. The growth rate of the macrocycle was 33.1 Å / cycle. The macrocycle was repeated 75 times which corresponds to an aluminium doping concentration of 4.7 %, and 250 nm of Al:ZnO. These parameters were optimized by measuring sheet resistance. All ALD procedures were controlled by a LabVIEW program developed by Ultratech/Cambridge Nanotech.

### 6.2.3 Characterization

PEC measurements were carried out in a solution containing 0.05 M methyl viologen (MV<sup>2+</sup>) dichloride (Sigma-Aldrich, 98%) and 0.1 M KCl (Sigma-Aldrich, 99.0%) as previously described.<sup>22,23</sup> Using a saturated calomel reference electrode and a Pt counter electrode a potential sweep at 5 mV/s from 0 to – 0.4 V using a CHI 832a electrochemical analyzer (Austin, TX) was carried out while a square-wave light stimulus was applied from a 150 W Newport Xe lamp with an AM 1.5D filter (Irvine, CA).

Scanning electron microscopy (SEM) was performed on the ECD CISE films using a Hitachi S-4500 field emission microscope (Toronto, ON) with an EDX system at 15.0 kV. XRD patterns were obtained from an Inel CPS Powder Diffractometer with an Inel XRG 3000 Cu X-ray generator, and an Inel CPS 120 detector. The scans were taken for 10 mins.

XAFS measurements of the Cu and In K-edges were performed at the PNC/XSD 20-BM beamline at Argonne National Laboratory in Argonne, IL, using the Advanced Photon Source (APS). CISE films were capped by Kapton tape. The beam was set in focused

mode, meaning that the measured area was small. A sample area of 200  $\mu\text{m}$  by 500  $\mu\text{m}$  was measured with an energy resolution ( $\Delta E/E$ ) of  $1.4 \times 10^{-4}$ . The incident chamber was filled with 50%  $\text{N}_2$  / 50% He by weight, while the transmission and reference chambers were filled with 100%  $\text{N}_2$ . A harmonic rejection mirror was set to  $< 5$  mrad, and the incident beam was detuned 15% at 9.8 keV. The samples were scanned using a Si (111) monochromator to modulate the incoming energy, with a 400  $\mu\text{m}$  and 700  $\mu\text{m}$  vertical slit for the Cu and In edges respectively. Samples were scanned over a 8.78 to 9.52 keV range for the Cu K-edge, and 27.744 to 28.786 keV for the In K-edge. Samples were placed  $45^\circ$  to the incident photons, and the 13-element Canberra detector was placed perpendicular to the beam. Detector saturation was set to 50,000 cps, and replicates were taken to a sum of 2 million total counts per element, ensuring that a significant edge jump ( $> 0.5$  a.u.) was obtained for each replicate. Multiple measurements further ensured the fine oscillations of the EXAFS region were reproducible. Spectra were normalized to the incident photon flux ( $I_o$ ) using the Athena software package, and calibrated against a reference foil (EXAFS Materials Inc.) using the first inflection point of the derivative spectra. The standards used included a 7.5  $\mu\text{m}$  thick copper foil, and 10  $\mu\text{m}$  indium foil.

All fittings were carried out using the Artemis software package, from which simulated spectra were generated. An ab initio method was utilized for calculating real-space multiple scattering pathways, including the effects of core-holes, real-space relativistic Green's function, and full multiscattering of the wavefunction. The atomic input file was based on the chalcogenide crystal structure of  $\text{Cu}_2\text{Se}$ , and generated using FEFF8.2 code to ensure the calculation contained self-consistency checks. This produced theoretical phase and scattering paths for the X-Se, X-S, X-Cu, and X-In pathways, where X was either Cu or In. The energy threshold ( $E_0$ ) was assigned to the peak maximum of the first derivative spectrum for each sample.<sup>24, 25</sup> The true  $E_0$  will differ from the experimentally calculated  $E_0$  in each sample.<sup>24</sup> Due to the unique  $E_0$  dependence of the phase shift function ( $\phi(k)$ ) this deviation needs to be corrected prior to distance determination.<sup>17, 26</sup> The inter-dependence of  $r$ ,  $\phi$ , and  $k$ , as seen in equation 6.1 below was manipulated to obtain matching phase shift functions:

$$\Delta\phi = -2(\Delta k)r - 2k(\Delta r) \quad (6.1)$$



where  $k$  is the momentum space wavenumber in  $\text{\AA}^{-1}$ , and  $r$  is the distance between two atoms in the model. This can be expanded through  $k$  as defined in equation 6.2, whereby we see the dependence of  $k$  on the assignment of  $E_0$ .

$$\Delta k = -\frac{0.2625(\Delta E_0)}{2k} \quad (6.2)$$

Combining equations 6.1 and 6.2 demonstrates the dependence of  $\phi(k)$  on  $E_0$ .

$$\phi(k) = \frac{0.2625(\Delta E_0)}{k} r - 2k(\Delta r) \quad (6.3)$$

To rectify  $\phi(k)$  of the experimental and model CIS,  $E_0$  was permitted to vary at the fitting stage. Refining  $E_0$  in this manner allows for phase transferability, and thus reduces error in the distance determinations by ensuring that the fitting is based on equal  $\phi(k)$ . All  $E_0$  shift values were correlated with each other to reduce the number of variables within the fit. By applying this concept to equation 6.3,  $\Delta r$  will be directly related to the experimental and theoretical  $k$  values, and thus  $\phi(k)$ , thereby eliminating additional uncertainty from deviations in the energy threshold term.

The solar cells were tested using an IVIUM CompactStat (Eindhoven, NL) potentiostat and the Newport lamp with and AM 1.5 D filter operating at 0.7 suns.

## 6.3 Results and Discussions

### 6.3.1 Optimization of ClSe Films

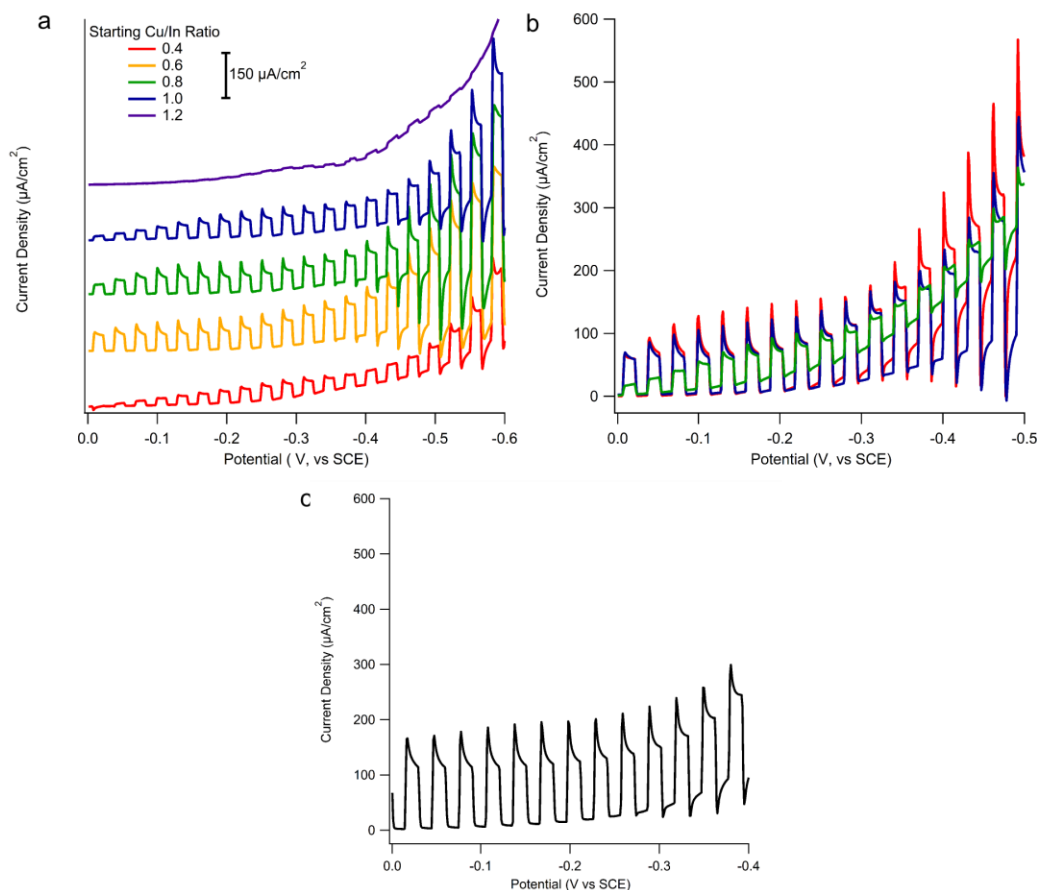


**Figure 6.1** Photoelectrochemical measurements in 0.05 M methyl viologen of a)  $\text{CuInSe}_2$  films made from a starting Cu/In ratio of 0.4 (red), 0.6 (orange), 0.8 (green), 1.0 (blue) and 1.2 (purple) and selenized with  $5 \text{ mg/cm}^2$  of selenium. b)  $\text{CuInSe}_2$  films fabricated with the starting ratio of 0.6 selenized with 3 (red), 5 (blue), and 10 (green)  $\text{mg/cm}^2$  of selenium. c)  $\text{CuInSe}_2$  film with the starting ratio of 0.6 with  $5 \text{ mg/cm}^2$  of selenium and some sulfur residue on the furnace tube.

The PEC measurements for a variety of starting Cu/In ratios are shown in Figure 6.1a. The ClSe films were obtained by selenizing and annealing with  $5 \text{ mg/cm}^2$  selenium content at  $550 \text{ }^\circ\text{C}$ , and the resulting photocurrent ranges for the different starting ratios of

Cu/In are shown in Table 6.1. In general, the lower starting Cu/In ratios exhibited higher photocurrent density than the higher starting Cu/In ratios. This trend is most likely due to the potential for secondary phases to form. When the starting metallic stacks are copper-rich,  $\text{Cu}_2\text{Se}$  and  $\text{CuSe}$  deposits might be formed in the CISE where extra copper reacts with selenium. It may also have to do with the formation mechanism of the CISE. In this case there is an annealing step of  $250\text{ }^\circ\text{C}$  for 20 mins before the CISE formation step at  $550\text{ }^\circ\text{C}$ . This step might allow the indium to diffuse into the copper, and for the selenium to begin permeating into the film. During this time, copper and indium selenide phases form along with copper indium phases.<sup>27,28</sup> When the temperature is increased to  $550\text{ }^\circ\text{C}$  CISE begins to develop via a reaction between the copper and indium selenide phases. If the Cu/In starting ratio is too high, copper selenide phases remain in the film and detract from the photocurrent. The opposite can be true as well; if the Cu/In starting ratio is too low the indium selenide phases are left unreacted and cause a decrease in the photocurrent.

The starting ratio of 0.6 (Figure 6.1a, orange, 0.6CISE) had the largest photocurrents during the entire scan, followed by the starting ratio of 1.0 (Figure 6.1a, blue 1.0CISE). The two CISE films are actually quite similar in their photocurrent density for having such radically different starting ratios. These two samples are chosen for further characterization to determine why samples with two different starting ratios would show such similar photocurrent densities.

**Table 6.1 Photocurrent Ranges for different starting ratios of CISe determined from photoelectrochemical measurements**

Starting Ratio of Cu/In	Photocurrent Range ( $\mu\text{A}/\text{cm}^2$ )
0.4	8 - 296
0.6	59 - 574
0.8	34 - 474
1.0	13 - 482
1.2	10 - 24

The selenium concentration was also optimized using PEC measurements, shown in Figure 6.1b. Three different amounts of selenium are shown: 3, 5 and 10  $\text{mg}/\text{cm}^2$  for CISe films with the starting Cu/In ratio of 0.6. These values were chosen based on previous selenization treatments on the related compound CZTS.<sup>20</sup> The photocurrent difference range was 60 to 116  $\mu\text{A}/\text{cm}^2$  for 3  $\text{mg}/\text{cm}^2$ , 59 to 574  $\mu\text{A}/\text{cm}^2$  for 5  $\text{mg}/\text{cm}^2$ , and finally 16 to 62  $\mu\text{A}/\text{cm}^2$  for 10  $\text{mg}/\text{cm}^2$ . Using 5  $\text{mg}/\text{cm}^2$  selenium to generate CISe films consistently showed larger differences between the dark current and photocurrent. There must be enough selenium present to fully form the copper and indium selenide phases that react to form the CISe, but an excess causes poor adhesion to the back contact and forms deposits on the surface.

The PEC measurement in Figure 6.1c is that of a CISe film that was contaminated with sulfur, forming CISSe instead of CISe. This sample offered the chance to determine the effect that sulfur incorporation has on the crystal structure of the CISe. Even with the sulfur incorporation, the photocurrent observed from the CISSe was in the mid-range of those observed from the pure phase CISe: varying between 110 and 171  $\mu\text{A}/\text{cm}^2$ .

The PEC measurements from Figure 6.1 also gave insight into the relative rates of the photoreactions occurring in solution upon illumination. At more negative potentials, in almost all of the PEC measurements, the current initially rapidly rises to a high

photocurrent value, followed by an exponential decay to an eventual plateau. When the light is turned off there is also a negative overshoot in the current that then increases back to a plateau. As the potential becomes less negative this behavior is suppressed to the point where only the photocurrent decrease during illumination is observed and then finally at potentials closer to 0, a nearly square wave occurred.

The shape of the transients are based on the photoreactions which have been discussed extensively in Chapters 2 and 4 as well as in literature.<sup>29</sup> Briefly, upon the injection of a photon an electron hole pair is created at the pseudo p-n junction created between the  $MV^{2+}$  solution and the CISE film. If the electron hole pair does not immediately decay, the photogenerated electron can associate with the  $MV^{2+}$  to form an intermediate species of  $MV^+$  and CISE. This intermediate species can either recombine at rate  $k_r$ , and no current flows; or the intermediate can separate at rate  $k_{ps}$ , and a photocurrent is observed. The relative rates of these two reactions ( $k_r/k_{ps}$ ) can be observed in the shape of the transients in the PEC measurements described earlier. The shape of the transients at the higher negative potentials corresponds to a large  $k_r/k_{ps}$ . This is due to the highly negative potentials shrinking the pseudo p-n junction. This makes the internal potential weaker, and the electrons are less likely to remain associated with the  $MV^{2+}$ . At the lower potentials, the pseudo p-n junction internal bias can push the electrons away. However, the push from the external bias is lower, and has the adverse effect of making the overall photocurrent lower.

### 6.3.2 Composition

The compositions of the final CISE films as determined by EDX are in Table 6.2. As expected, the 1.0CISE film had a final ratio very close to 1.0, and was slightly copper-rich. The 0.6CISE film also had a final ratio close to that of stoichiometric CISE, but slightly copper-poor. Typically, copper-rich films have shown the optimal traits for the light-absorbing layer and pure phase CISE chalcopyrite structure.<sup>30, 31</sup> Unfortunately, these films often have to be treated with KCN to remove excess CuSe phases.<sup>31, 32</sup> The method used here produced CISE while avoiding KCN completely.

**Table 6.2 Relative molar ratios of CuInSe<sub>2</sub> and CuIn(S,Se)<sub>2</sub>**

Sample	Cu	In	Se	S
CISE with Starting Ratio of 0.6	0.903	1.00	1.53	-
CISE with Starting Ratio of 1.0	1.03	1.00	1.63	-
CISSe with Starting Ratio 0.6	1.09	1.00	0.824	0.317

The increase in the Cu/In ratio for the original 0.6 to 0.9 may be due to the loss of indium during the high-temperature selenization. The pre-annealing step at 250 °C is meant to convert the copper indium stack to form Cu<sub>11</sub>In<sub>9</sub>, as well as copper and indium selenide phases.<sup>28</sup> The excess indium can remain un-reacted and vaporize, as the melting point of indium metal is approximately 157 °C. This would cause the final film made from the 0.6CISE sample to have a higher Cu/In ratio. The 1.0CISE had less indium so the amount of selenium was sufficient to react fully, and as such no indium was lost.

All three films are deficient in selenium (or sulfur) based on their EDX molar ratios relative to the stoichiometric value of 2. This explains why the samples with 3 mg/cm<sup>2</sup> of selenium showed lower photocurrents, as not enough selenium was present to fully form the CISE across the entire film. On the other hand, when more selenium was added to the furnace – as mentioned earlier – it significantly affected the adhesion of the CISE to the molybdenum substrates.

### 6.3.3 Morphology

The morphology of the two CISE films was investigated using SEM (Figure 6.2). The larger image displays that of the surface morphology of the CISE films and the inset shows the morphology at lower magnification. At a large scale the film appears quite smooth and uniform which is ideal for solar cell fabrication. Upon magnification it is

observed that both CISE films had very similar surface morphologies consisting of larger structures sitting on top of a more dense film. The dominant features – the larger granular structures – vary in size between the two films. The 0.6CISE (Figure 6.2a) had much smaller granular sizes ranging from 0.73 to 1.1  $\mu\text{m}$  with an average size of  $0.9 \pm 0.1 \mu\text{m}$ , while the 1.0CISE (Figure 6.2b) had granular sizes ranging from 0.44 to 0.74  $\mu\text{m}$  with an average size of  $0.6 \pm 0.1 \mu\text{m}$ . As the selenization conditions were kept constant between these two samples, the change in grain size is attributed to the variance in the Cu/In starting ratio.

The other feature that is observed from these images is the structures that lie beneath the granular structures. It is circled in red in Figure 6.2. This dense sublayer CISE film appears smoother than the surface structures. The dense part of the films is exposed to the surface more so in the 0.6CISE sample than the 1.0CISE sample, which may account for the high photocurrent observed from the non-stoichiometric starting ratio 0.6CISE sample. This potentially more compact film would be ideal for full device development as it would have a greater electrical connectivity than that of the looser surface morphology.

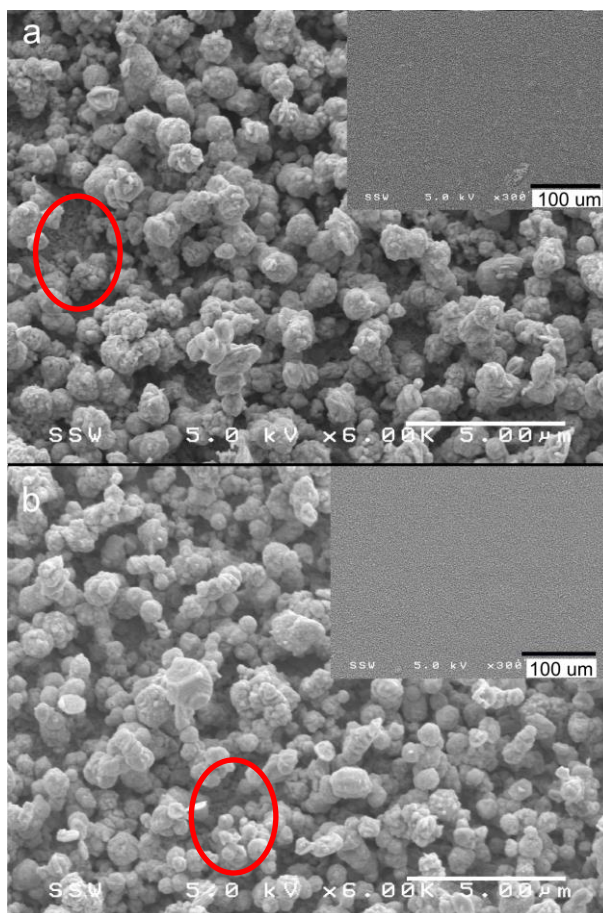


**Figure 6.2 SEM images of a) CISe with a starting ratio of 0.6 and b) CISe with a starting ratio of 1.0**

The EDX analysis has already suggested that these two films are similar, and the morphology adds further evidence to that statement. The increased grain size of the 0.6CISe is ideal for full device development.<sup>32</sup> The porous surface morphology, however, may be detrimental to achieving an efficient full device, as the rough surface can increase recombination sites.<sup>32, 33</sup>

#### 6.3.4 Structure of the CISe Films

XRD was utilized to determine the crystal structure of the CISe films. The XRD patterns for each of the three samples are shown in Figure 6.3. The 0.6CISe and 1.0CISe (Figure 6.3 a and b) samples matched well with the CISe standard card (JCPDS card no. 40-1487), which has its three most intense peaks at 26.57 °, 44.23 °, and 52.38 °. These are



the characteristic intense chalcopyrite peaks corresponding to the planes (112), (220), and (312), which are shown pictorially in Figure 6.3d. There were no other peaks from common secondary phases such as CuSe, Cu<sub>2</sub>Se, or In<sub>2</sub>Se<sub>3</sub>, suggesting that the CISE is pure phase. The above observations agree well with those from a study on a self-assembled lateral In<sub>2</sub>Se<sub>3</sub>/CISE heterojunction.<sup>34</sup> Interestingly, the CISSe sample's (Figure 6.3c) three most intense chalcopyrite peaks were shifted to higher angle values when compared to the standard CISE card. The standard peaks for CIS (JCPDS card no. 85-1575) are at larger angle values than those of CISE. The lack of dual peaks suggests that sulfur atoms present in the film are intercalated into the CISE through sulfur substitutions at the selenium sites. It has been previously determined that when there is replacement of Se with S in CISSe and CuInGa(S,Se)<sub>2</sub> compounds the peaks will appear somewhere between the two peak values.<sup>19, 35-37</sup>

The peak at 31° that is present in both the 0.6CISE and 1.0CISE samples indicates that MoSe<sub>2</sub> is present between the CISE and the molybdenum. In a similar system of Cu(In,Ga)Se<sub>2</sub> it has previously been discovered that MoSe<sub>2</sub> forms between the light-absorbing layer and the back contact.<sup>38</sup> A thin film of p-type MoSe<sub>2</sub> can increase device efficiency for several reasons: it forms a proper ohmic back contact, it can improve adhesion of the CISE with the back contact, the wider band gap of MoSe<sub>2</sub> (1.4 eV) can reduce recombination at the back contact, and finally its presence can prevent further reactions between the CISE and the molybdenum.<sup>15</sup>

The lattice parameters of the unit cell are  $a$ ,  $b$  and  $c$ . In the chalcopyrite system  $a$  and  $b$  are equal. The parameters can be calculated using equation (6.4) where  $a$  and  $c$  are the crystal lattice parameters;  $h$ ,  $l$ , and  $k$  are the miller indices; and  $d$  is the d-spacing.

$$\frac{1}{d^2} = \frac{h^2+k^2}{a^2} + \frac{l^2}{c^2} \quad (6.4)$$

The 0.6CISE lattice parameters were determined as 5.79 Å and 11.64 Å and the 1.0CISE parameters were 5.83 Å and 11.69 Å for  $a$  and  $c$ , respectively. Both matched well to the parameters for the standard CISE which are 5.78 Å and 11.62 Å (JCPDS card no. 40-1487). The lattice parameters for the CISSe sample were calculated as:  $a$  equal to 5.74 Å

and  $c$  equal to 11.49 Å. These values are smaller than the standard CISE lattice parameters. They are, in fact, an intermediate value between the CIS and CISE standard values. The shrinking of the lattice parameters is indicative of selenium being substituted with sulfur, and since sulfur is a smaller atom than selenium, it is expected that the crystal unit cell decreases as it gains more and more sulfur. This observation agrees well with that of solution growth CISSe films.<sup>36</sup>

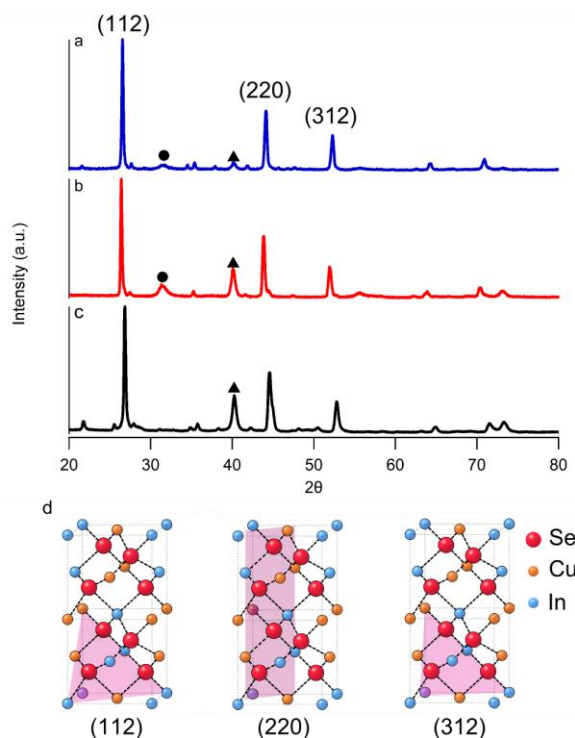


**Figure 6.3 X-ray Diffraction patterns of a) CISe with a starting ratio of 0.6 b) CISe with a starting ratio of 1.0 and c) CuInSSe with a starting ratio of 0.6 and d) the planes for the three most intense chalcopyrite peaks. The peaks marked with a ▲ are the molybdenum back contact and the peaks marked with a ● are MoSe<sub>2</sub>**

**Table 6.3 Major peaks from the XRD patterns, their full width at half maximum and the related crystal size**

Sample	2 $\Theta$ (°)	FWHM (rad)	D (nm)
<b>CISE Starting Ratio 0.6</b>	26.58	0.00349	40.8
	44.17	0.00515	29.1
	52.33	0.00566	27.3
<b>CISE Starting Ratio 1.0</b>	26.43	0.00331	43.0
	43.88	0.00497	30.1
	51.99	0.00619	24.9
<b>CISSe Starting Ratio 0.6</b>	26.86	0.00391	36.5
	44.60	0.00718	20.9
	52.85	0.00715	21.7

The crystal sizes for the three films were calculated using the Debye-Scherrer equation (equation 6.5), and are listed in Table 6.3. Where D is the particle size,  $\lambda$  is the X-ray source wavelength, B(2 $\Theta$ ) is the full width at half maximum, and  $\Theta$  is the angle at which the peak occurred. The average calculated crystal sizes were  $33 \pm 9$  nm for the 1.0CISE and  $32 \pm 7$  nm for the 0.6CISE. The two CISE films had significantly smaller crystal sizes than those reported from the SEM images. It is common for the crystal sizes to be smaller than the grain sizes. The sizes for the CISSe films were smaller with an average of  $26 \pm 9$  nm. This is consistent with literature in that a material with higher selenium content will have a narrower peak and thus larger crystals.<sup>36</sup>

$$D = \frac{0.9\lambda}{B(2\Theta)\cos\Theta} \quad (6.5)$$

### 6.3.5 XANES of the Cu and In K-edges

The XANES spectra of the Cu and In K-edges of 0.6CISe sample and the CISSe are presented in Figure 6.4. The Cu K-edge (Figure 6.4a) absorption peak occurred at 8986 eV which is indicative of a Cu(I) state as summarized by Solomon *et al.* from many Cu(I) and Cu(II) model complexes.<sup>25</sup> There is a very small feature at 8983.7 eV (which is more apparent in the inset in Figure 6.4a) in the absorption edge. Typically, the absorption – from edge to peak – should occur over 2 to 3 eVs. This absorption, however, occurs over 7 eVs. Using a XANES spectra study in which a large variety of copper compounds in various oxidation states, orientations, and coordination numbers were compared,<sup>25</sup> it was determined that this small feature at 8983.7 eV corresponds with the  $1s \rightarrow 4p$  transition commonly associated with Cu(I). None of the spectra show a pre-edge structure around 8979 eV, and the principle absorption peak does not show splitting or twinning, which strongly suggests the film is devoid of Cu(II).<sup>25</sup> The positioning of the feature at 8983.7 eV in the absorption edge and the energy at which the main peak occurred are both indicative of Cu(I) that has a coordination number of 4 in a tetrahedral formation, based on comparison with Solomon *et al.*'s findings.<sup>25</sup> When the energy is greater than 8993 eV both samples' absorption spectra are very similar in shape and intensity. This is suggestive of long-range order and will be discussed in more detail in the EXAFS section 6.3.6.

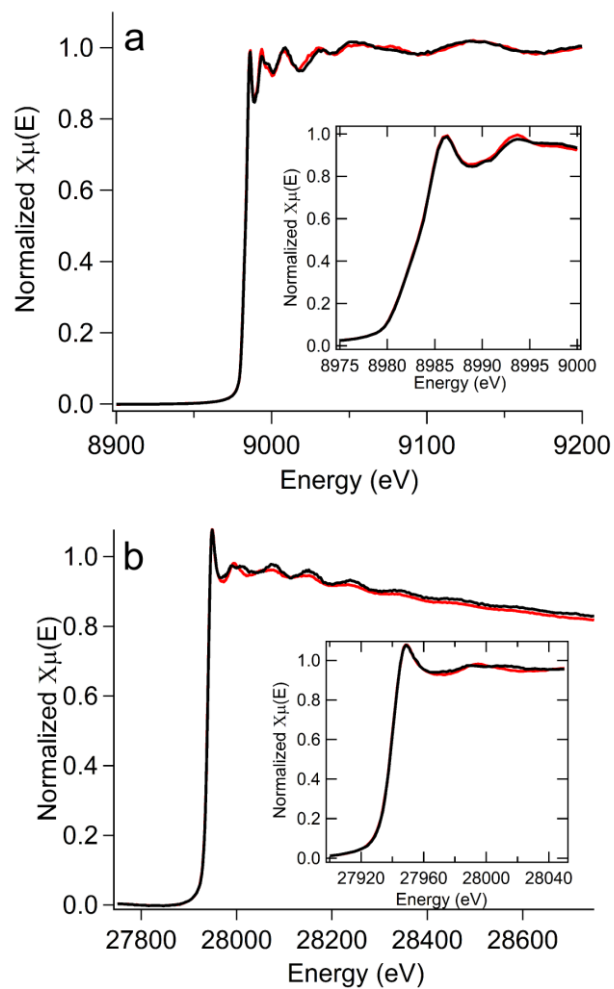


**Figure 6.4 XANES absorption spectra for pure phase CISE (red) and CISSe (black)**  
**a) Cu K-edge and b) In K-edge**

The In K-edge XANES (Figure 6.4b) absorption peak for both films occurred at 27949 eV. Drawing from XANES data for systems involving  $\text{In}_2\text{O}_3\text{-Al}_2\text{O}_3$  and Zn-In-Sn it was determined that the indium present in the CISE is In(III).<sup>39, 40</sup> The extended regions between the CISE and CISSe deviate from each other, unlike in the Cu K-edge. The energy required to obtain the In K-edge is quite high, which scatters the X-ray beam. This increases contributions from core-hole and instrumental broadening, which can obscure broadening caused by disorder.<sup>40, 41</sup> There are significant deviations after the absorption edge between the two films. Further investigation into the copper and indium edges was carried out with EXAFS analysis as described below.

### 6.3.6 EXAFS Cu and In K-edge

EXAFS is a powerful technique that is used to accurately determine local structural information on the absorbing atoms, as demonstrated by Zhang *et al.* with Au nanoclusters.<sup>42</sup> In this work, EXAFS was used to determine the effects that sulfur substituting for selenium has on the CISE structure.

The first step for EXAFS analysis involves transforming the absorption spectrum to a “k-space” spectrum via a well-established method that changes the x-axis from energy (eV) to photoelectron wavenumber  $k$  ( $k = \hbar^{-1}(2m_e(E - E_0))^{1/2}$ ).<sup>24, 42</sup> The result is an oscillating spectrum with amplitudes and phase shifts that reveal contributions from the interactions of the other atoms relative to the absorption atom.<sup>24</sup>

The EXAFS oscillations of both the CISE and CISSe samples were converted to k-space (using a  $k^3$ -weighting factor) for directly comparing the local structure of the Cu or In absorber centers. The  $k^3$ -weighting factor was chosen over the more typical  $k^2$ -weighting so that information pertaining to structure at greater distances from the absorbing atom were not lost. The k-space spectrum transformed from the copper K-edge is shown in Figure 6.5a. The first major difference is the oscillation in early k-space between 4 and 5  $\text{\AA}^{-1}$ . The CISE sample had a disruption in the oscillation while the CISSe did not. Deviations at lower wavenumbers are indicative of defects and irregularities in the first and second shell nearest neighbours (the atom directly next to, or one atom removed from the copper).<sup>43</sup> So in the immediate vicinity to the copper atom, there are already

deviations from the pure phase CISE as the sulfur substitutes into the crystal lattice, thus short-range disorder is observed.

The oscillations at higher wavenumbers ( $> 6 \text{ \AA}^{-1}$ ) in the CISSe deviate from the CISE spectrum as well. There is a loss in the intensity of the oscillations in the CISSe spectrum. The CISE, however, has a relatively low loss of intensity at higher wavenumbers, which indicates long range order. The  $k^3$  weighting has a larger influence on the higher wavenumbers, so it would be expected that there would be no loss of signal if there was consistent interatomic distances and long-range order.<sup>17</sup> The degradation of the amplitude in the CISSe sample confirms that it lacks the long range order shown by the CISE sample. However, the extent of the deviations suggests that the sulfur substitutions are random, and thus a hindrance to long-range film quality.

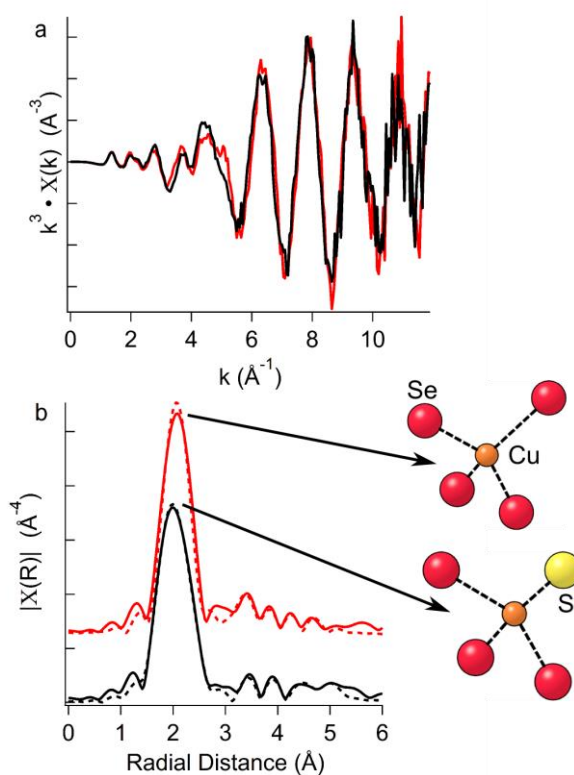


**Figure 6.5 Cu K-edge EXAFS for pure CISE (red) and CISSe (black) a) measured  $k$ -space oscillations and b) Fourier transform spectra of the  $k$ -space spectra. The solid line is the experimental data and the dashed line is the multishell fit. The structures in the figure illustrate the atoms that contribute to the most intense peak.**

A Fourier transformation (FT) of the k-space spectrum produces a pseudo radial space or “R-space” spectrum, and this is where the most useful information can be obtained.<sup>42</sup> The R-space spectrum is fitted to a theoretical model for the system, and by obtaining the best fit possible information on the distance between the atom of interest and its neighbouring atoms can be obtained.<sup>24, 42</sup> This involves generating the idealized crystal structure complete with the coordinates of the atoms in the structure. Then running all the possible scattering paths, selecting the most likely paths and optimizing the parameters until the simulated spectra best portrays that which was observed in the experimental. This information can pertain to how temperature,<sup>44</sup> coordination number,<sup>45</sup> ligand identity,<sup>43</sup> and size<sup>42</sup> of the particles in the system affect the atomic interactions. The theoretical fit is often a multishell fit (or a fit that includes the effects of atoms further away from the atom of interest) to give a more in-depth understanding of the structural changes.<sup>42</sup> The multi-shell fit uses many scattering pathways so more information can be elucidated from the spectra. The FT of the k-space oscillations between 2.8 and 11 Å<sup>-1</sup> was carried out to extract the R-space spectrum for the copper K-edge. A multishell fitting was used to fit this data, as this extended region increases the spatial resolution to allow for contributions from multiple scattering shells: X – Cu, and X – In, where X is Cu or In. The result of the FT of the Cu k-space is shown in Figure 6.5b, and is not phase corrected. A multishell fit was used to fully elucidate the structure and how it changes at the copper site when sulfur is intercalated into the CISE crystal lattice.

The theoretical multishell fit matched well with the experimental spectrum. The most intense peak occurred at 2.086 Å for the CISE and 1.994 Å for the CISSe. The CISSe peak is broader and shifted to a lower wavenumber in the CISSe when compared to the CISE spectrum. CISSe peak onset occurred 0.03 Å earlier than the CISE spectrum, and the peak is shifted down by 0.092 Å. The most intense peak originates from the Cu – Se bond, and in the case of CISSe it has contributions from both Cu – S and Cu – Se bonds. The Cu – S and Cu – Se contributions in the peak are not equal. In fact, the exact ratio between selenium and sulfur can be determined based on the fit to the R-space. The selenium and sulfur coordination numbers were varied until an optimal fit was acquired. The resulting Se:S ratio for this fit was 7.5:1. This ratio was obtained by altering the crystal structure with the sulfur substituted by sulfur which was then followed by



obtaining the different possible scattering pathways and creating the simulated spectrum. The amount of sulfur in the starting crystal structure was optimized to the reported 7.5:1 based on the fit between the experimental and simulated spectra. The peaks to the right of the intense peak are due to the metal-metal interactions. These two features in the CISSe are caused by the S substitution in the Se sites, which is more apparent when the bond lengths are considered.

To help visualize the bonds being discussed, the chalcopyrite crystal structure of CISe is shown in Figure 6.6. The calculated values for the interatomic distances for copper are reported in Table 6.4. The atoms of interest and their nearest neighbours are highlighted in Figure 6.6. The Cu – Se distance (circled in pink) for the CISe sample is 2.39 Å, and in the CISSe is 2.45 Å and the Cu – S distance in the CISSe is 2.21 Å. The increase in Cu – Se bond length in the CISSe sample is due to sulfur substituting for the selenium. Sulfur is a smaller atom than selenium, and as a result the bond length is shorter than the one observed for Cu – Se in the pure phase CISe. The Cu – Se bond in the CISSe then has to lengthen to compensate for the shortened bond length of the Cu – S. This further explains the shift observed in the XRD pattern and the loss of intensity in the CISSe k-space oscillation.

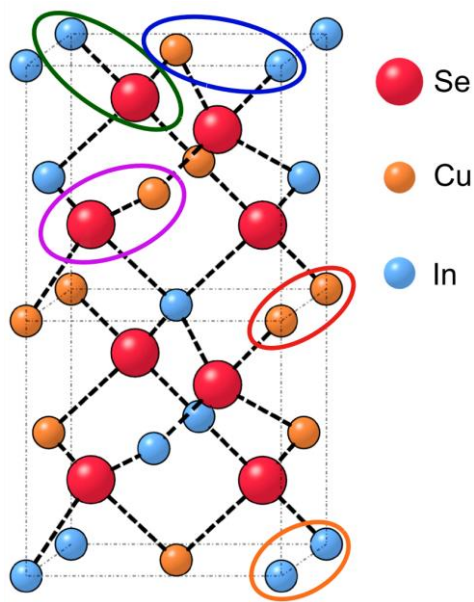


**Figure 6.6 Chalcopyrite structure of CISe with the following bonds circled: Cu – Se (S) in pink, Cu – In in blue, Cu – Cu in red, In – Se (S) in green and In – In in orange.**

Figure 6.7 contains the k- and R-space spectra calculated using the absorption spectrum for the In K-edge. As in the copper spectra, a  $k^3$  weighting was employed for the k-space, and a multishell theoretical fit was used for the R-space spectrum. The In K-edge k-space oscillations (Figure 6.7a) had many of the same characteristics as the Cu spectra. There is a deviation in the amplitude between the two spectra between 4 and 5  $\text{\AA}^{-1}$ . The CISSe oscillation is again more defined and larger than that of the CISe. As previously mentioned, the  $k^3$  weighting gives more weight to the oscillations at higher wavenumbers so when such a large peak is seen in the low wavenumber region it is expected that there is again deviation in the first and second shell neighbours. The diminished amplitude in the CISSe films is observed again in the oscillations at higher wavenumbers indicating long-range disorder in the CISSe film compared to the CISe film.

The deviations observed between the two spectra imply there is a significant amount of disorder in the CISSe. The high energy required to obtain the indium K-edge EXAFS obscures changes resulting from disorder in the films, due to core-hole, and instrumental broadening. Since differences between the two spectra are observed, this is indicative of

a significant amount of structural changes in the CISSe. The deviations between the two k-space spectra would be due to heavy metal defects pertaining to indium such as Cu vacancies or In substitutions at Cu sites. These defects would create the significant changes seen in the spectrum. Sulfur substitutions would not be observed easily in such a high energy spectrum. The heavy metal defects, however, revealed how the lattice compensates for the sulfur substitutions.

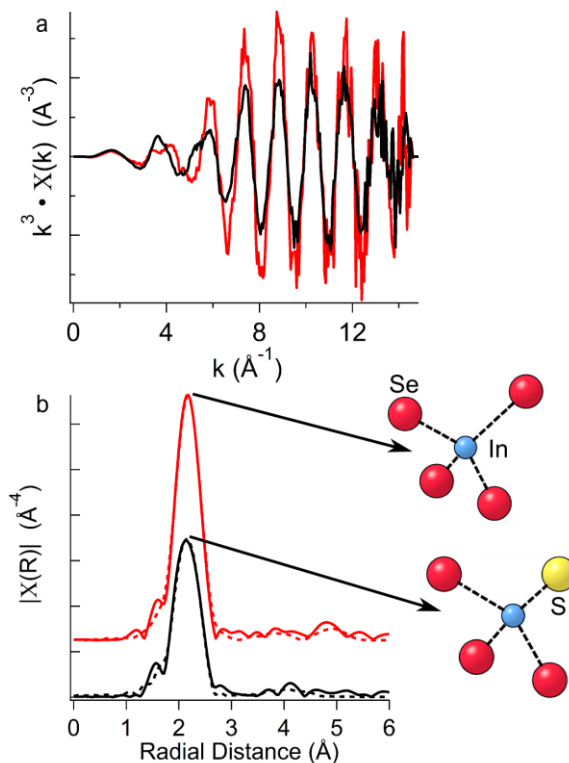


**Figure 6.7 Indium K-edge EXAFS for pure CISE (red) and CISSe (black) a) measured k-space oscillations and b) Fourier transform of the k-space spectra. The solid line is the experimental data and the dashed line is the multishell fit. The structures in the figure illustrate the atoms that contribute to the most intense peak.**

The R-space spectra calculated from the FT of the k-space oscillations between 2.8 and 13  $\text{\AA}^{-1}$ <sup>45</sup> are in Figure 6.7b. CISE and CISSe both had intense peaks that were the same width and had no peak shift. The most intense peak is due to the In – Se, or again in the case of CISSe, the In – S and In – Se bonds. The bonds to the right are the metal-metal bond lengths. The theoretical multishell fit does not match as well as what was presented for the Cu. This confirms that the indium appears to be the primary source of the structural deviations resulting from the sulfur substitutions at selenium sites. The increase in the deviations from the theoretical fit is indicative that some indium centers are not in the expected crystallographic locations.

The In – Se (Figure 6.6, circled in green) distance for both samples is 2.57  $\text{\AA}$ . The Cu – In (Figure 6.6, circled in blue) distance gave more insight into how the crystal structure

compensates for the sulfur substitution. In the CISE samples, the Cu – In distance was calculated at 4.32 Å by both the indium and copper spectra. The CISSe sample had conflicting Cu – In distances. When calculated by the copper FT spectrum, the distance between the Cu – In was 4.00 Å, and when calculated from the indium spectrum the In – Cu distance was 4.29 Å. The indium compensates for the lattice distortion caused by the sulfur substitutions more so than copper. An indium replacing a copper in the crystal structure is the most common way the lattice compensates for the distortion caused by the sulfur substitution. This causes significant changes in all the bond lengths including the Cu – Cu (Figure 6.6, circled in red) and the In – In (Figure 6.6, circled in orange) when compared to the CISE.

**Table 6.4 EXAFS R-space spectrum results from multishell fitting procedure of CISE and CISSe**

<b>Cu K-edge</b>	<b>CISE Distance to nearest neighbor (Å)</b>	<b>CISSe Distance to nearest neighbor (Å)</b>
Cu - Se (1)	2.39 ± 0.01	2.45 ± 0.01
Cu- Cu (1)	4.18 ± 0.01	4.02 ± 0.01
Cu - In (1)	4.32 ± 0.01	4.00 ± 0.01
Cu - S (1)	-	2.21 ± 0.02
<b>In K-edge</b>		
In - Se (1)	2.57 ± 0.01	2.57 ± 0.01
In -Cu (1)	4.32 ± 0.01	4.30 ± 0.02
In- In (1)	4.02 ± 0.01	4.18 ± 0.02
In - S (1)	-	2.49 ± 0.03

The incorporation of this CISSe into full solar cells may need more improvement on the control of the sulfur incorporation into the films before its potential to generate a high-efficiency solar cell can be realized. The disorder induced by the sulfur substitutions –

especially in the indium – may cause recombination sites and electron loss in the full device. The long-range lattice disorder may cause further lattice mismatching between the CISSe and the CdS films, thus detracting from the overall current from the solar cell devices.

### 6.3.7 Solar Cell

The addition and optimization of the CdS buffer layer was the next step in the solar cell fabrication. The PEC measurement for the two-layer system compared to the single-layer system is in Figure 6.8. There is a photocurrent enhancement in the PEC measurement upon the addition of the cadmium sulfide layer. This enhancement has been demonstrated in the past.<sup>23</sup>

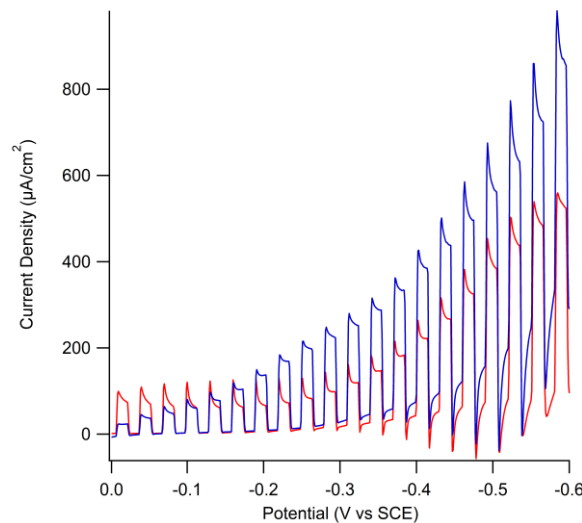


**Figure 6.8** PEC measurement of  $\text{CuInSe}_2$  with a starting ratio of  $\text{Cu/In} = 0.6$ , selenized with  $5 \text{ mg/cm}^2$  of selenium (red) and a PEC measurement of that same film coated with CdS (blue).

A full device was fabricated by using the ALD to deposit 50 nm of ZnO and 250 nm of Al:ZnO films. The resulting J-V curves are shown in Figure 6.9. For the calculation of the fill factor and the efficiency of the solar cells equations (6.6) and (6.7) were used.

$$\text{Fill Factor} = \frac{V_{MP} I_{MP}}{V_{oc} I_{sc}} \quad (6.6)$$

$$\eta = \frac{V_{OC}I_{SC}FF}{P_{in}}$$

Where  $V_{MP}$  and  $I_{MP}$  are the potential and current at the maximum power,  $V_{OC}$  is the open circuit potential,  $I_{SC}$  is the short circuit current FF is the fill factor and  $P_{in}$  is the input power.

The low efficiency solar cell (Figure 6.9a) had a  $J_{sc}$  of 0.236 mA/cm<sup>2</sup>, a  $V_{OC}$  of 0.017 V, a fill factor of 0.262, and an efficiency of 0.0013 %. The higher-efficiency solar cell (Figure 6.9b) had a  $J_{sc}$  of 0.135 mA/cm<sup>2</sup>, a  $V_{OC}$  of 0.15 V, a fill factor of 0.350, and an efficiency of 0.010 %. This low efficiency may be due to the diffuse surface morphology shown in the SEM images of the CISE. It is porous and non-compact which would increase electron losses due to recombination. The current produced over time by the full device can be seen in the inset in Figure 6.9a. The light was alternated between on and off to produce a square wave in the current produced by the solar cell. The current difference produced by the solar cell was 0.219 mA/cm<sup>2</sup>, while the open-circuit voltage was very low. If the loose surface layer above the dense CISE film is removed the efficiency observed from these solar cells might increase further.

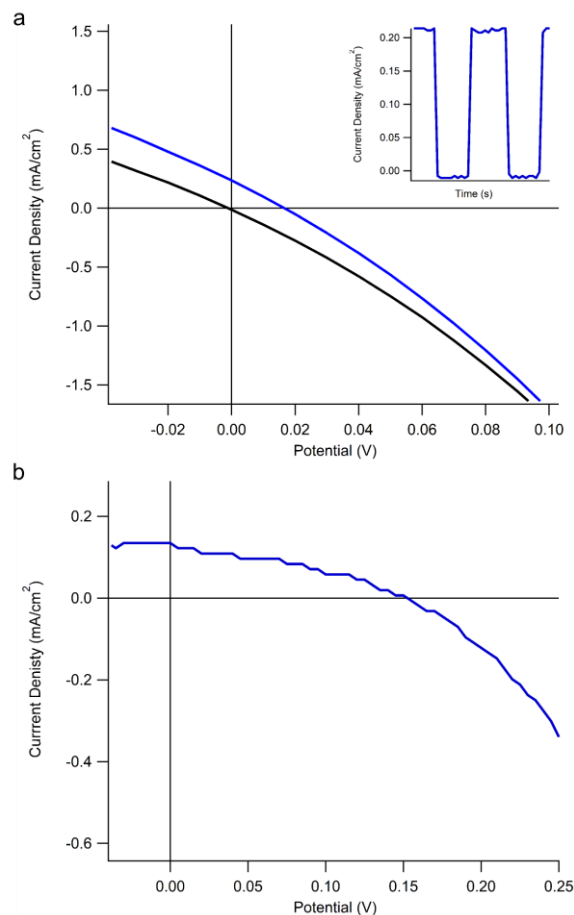


**Figure 6.9** The J-V curve of  $0.5 \text{ cm}^2$  CuInSe<sub>2</sub> solar cell in the light (blue) and dark (black). The inset is the current produced by the cell at 0 V and b) high efficiency J-V curve of  $0.12 \text{ cm}^2$  CuInSe<sub>2</sub> in the light (blue).

## 6.4 Conclusion

In summary, CISE films on Mo substrates were synthesized by the selenization of the successively electrodeposited metallic stacks of Cu/In. A starting ratio of Cu/In of 0.6 selenized with  $5 \text{ mg/cm}^2$  of selenium produced a pure phase CISE with a final ratio of 0.903:1.00:1.53. It had granular surface structures that were approximately a micrometer in size, and the film contained no secondary phases. The oxidation states of the copper and indium were confirmed as Cu(I) and In(III) using XANES. The copper and indium were also determined as being in 4-coordinate tetrahedral systems.



A CISE film that had been contaminated by sulfur was also investigated. The CISSe final composition ratio was found to be 1.09:1.00:0.824:0.317 for Cu:In:Se:S. The XRD and EXAFS data through the k- and R-space revealed that the sulfur intercalates into the CISE crystal structure to form CISSe in a ratio of 7.5:1 for Se:S. Sulfur substitutes selenium in the crystal structure which shrinks the lattice parameters from the 5.79 Å and 11.64 Å in the CISE sample to 5.83 Å and 11.69 Å in the CISSe. The sulfur substitutions are compensated by the lattice in two ways: first, the Cu – Se bond lengthens from 2.39 Å to 2.45 Å, and second, indium is substituted for copper. This was determined by the mismatch of the Cu – In bond length determined between copper and indium's FT spectra (Cu – In, 4.00 Å and In- Cu, 4.29 Å). This means indium is more disordered as it substitutes at copper sites in the crystal lattice, and is the primary compensator for the sulfur substitution. The formation of CISSe is still uncontrollable, and more work may need to be done on controlling how the sulfur incorporates into the lattice so that the highest possible efficiency can be achieved.

Finally, a full device was fabricated using the structure of Mo/CISE/CdS/ZnO/Al:ZnO/In. The efficiency was low; possibly due to the morphology of the CISE film. If this issue can be fixed then this method has great potential in commercializing CISE solar cells

## 6.5 References

- (1) Tuttle, J.; Goral, D. A.; Kennedy, C.; Noufi, R.; *Solar Cells* **1988**, *24*, 67-79.
- (2) AbuShama, J., A. M.; Johnston, S.; Moriarty, T.; Teeter, G.; Ramanathan, K.; Noufi, R.; *Prog. Photovolt: Res. Appl.* **2004**, *12*, 39-45.
- (3) Hodes, G.; Cahen, D.; *Solar Cells* **1986**, *16*, 245-254.
- (4) Wu, L.; Chen, S.-Y.; Fan, F.-J.; Zhuang, T.-T.; Dai, C.-M.; Yu, S.-H.; *J. Am. Chem. Soc.* **2016**, *138*, 5576-5584.
- (5) Kim, J.-Y.; Yang, J.; Yu, J. H.; Baek, W.; Lee, C.-H.; Son, H. J.; Hyeon, T.; Ko, M. J.; *ACS Nano* **2015**, *9*, 11286-11295.
- (6) Thomas, S. R.; Chen, C.-W.; Date, M.; Wang, Y.-C.; Tsai, H.-W.; Wang, Z. M.; Chueh, Y.-L.; *RSC Adv.* **2016**, *6*, 60643-60656.
- (7) Lee, B. S.; Park, S. Y.; Lee, J. M.; Jeong, J. H.; Kim, J. Y.; Chung, C. H.; Lee, D. K.; *ACS Appl. Mater. Interfaces* **2016**, *8*, 24585-24593.

- (8) Chiang, C.-S.; Lee, W. H.; Chang, T. W.; Su, Y. H.; *J. Appl. Electrochem.* **2015**, *45*, 549-556.
- (9) Li, L.; Ma, Y.; Gao, G.; Wang, W.; Guo, S.; You, J.; Xie, J.; *J. Alloys Compd.* **2016**, *658*, 774-779.
- (10) Sun, J.; Batabyal, S. K.; Tran, P. D.; Wong, L. H.; *J. Alloys Compd.* **2014**, *591*, 127-131.
- (11) Saidi, H.; Boujmil, M. F.; Durand, B.; Bouaïcha, M.; *J. Alloys Compd.* **2017**, *695*, 779-786.
- (12) Cheng, Y.-S.; Wang, N.-F.; Tsai, Y.-Z.; Lin, J.-J.; Houn, M.-P.; *Appl. Surf. Sci.* **2017**, *396*, 631-636.
- (13) Yeh, M.-H.; Hsu, H.-R.; Wang, K.-C.; Ho, S.-J.; Chen, G.-H.; Chen, H.-S.; *Solar Energy* **2016**, *125*, 415-425.
- (14) Londhe, P. U.; Rohom, A. B.; Lakhe, M. G.; Bhand, G. R.; Chaure, N. B.; *Semicond. Sci. Technol.* **2016**, *31*, 125009.
- (15) Kemell, M.; Ritala, M.; Leskelä, M.; *Crit. Rev. Solid State Mater. Sci.* **2005**, *30*, 1-31.
- (16) Adurodija, F. O.; Song, J.; Asia, I. O.; Yoon, K. H.; *Sol. Energy Mater. Sol. Cells* **1999**, *58*, 287-297.
- (17) Newville, M.; *Rev. Mineral. Geochem.* **2014**, *78*, 33-74.
- (18) Barbosa, L. L.; de Almeida, M. R. H.; Carlos, R. M.; Yonashiro, M.; Oliveira, G. M.; Carlos, I. A.; *Surf. Coat. Technol.* **2005**, *192*, 145-153.
- (19) Lai, Y.; Kuang, S.; Liu, F.; Yuan, Z.; Zhang, Z.; Li, Y.; Liu, J.; Wang, B.; Tang, D.; Li, J.; Liu, Y.; *Appl. Surf. Sci.* **2011**, *257*, 8360-8365.
- (20) Jiang, C.; Hsieh, Y. T.; Zhao, H.; Zhou, H.; Yang, Y.; *J. Am. Chem. Soc.* **2015**, *137*, 11069-11075.
- (21) Lee, S. M.; Ikeda, S.; Yagi, T.; Harada, T.; Ennaoui, A.; Matsumura, M.; *Phys. Chem. Chem. Phys.* **2011**, *13*, 6662-6669.
- (22) Tapley, A.; Vaccarello, D.; Hedges, J.; Jia, F.; Love, D. A.; Ding, Z.; *Phys. Chem. Chem. Phys.* **2013**, *15*, 1431.
- (23) Ye, H.; Park, H. S.; Akhavan, V. A.; Goodfellow, B. W.; Panthani, M. G.; Korgel, B. A.; Bard, A. J.; *J. Phys. Chem. C* **2011**, *115*, 234-240.
- (24) Teo, B. K., *EXAFS: Basic Principles and Data Analysis*. Springer: Berlin, 1986.

- (25) Kau, L. S.; Spira-Solomon, D. J.; Penner-Hahn, J. E.; Hodgson, K. O.; Solomon, E. I.; *J. Am. Chem. Soc.* **1987**, *109*, 6433-6442.
- (26) Koningsberger, D. C.; Prins, R., *X-Ray Absorption: Principles, Applications, Techniques of EXAFS, SEXAFS, and XANES*. Blackwell: Eindhoven, The Netherlands, 1988.
- (27) Rastogi, A. C.; Balakrishnan, K. S.; Sharma, R. K.; Jain, K.; *Thin Solid Films* **1999**, *357*, 179-188.
- (28) Bhattacharyya, D.; Forbes, I.; Adurodija, F. O.; Carter, M. J.; *J. Mater. Sci.* **1997**, *32*, 1889-1894.
- (29) Vaccarello, D.; Hedges, J.; Tapley, A.; Love, D. A.; Ding, Z.; *J. Electroanal. Chem.* **2015**, *738*, 35-39.
- (30) Nakamura, S.; Yamamoto, A.; *Sol. Energy Mater. Sol. Cells* **2003**, *75*, 81-86.
- (31) Lee, S. M.; Ikeda, S.; Harada, Y. O. T.; Matsumura, M.; *J. Non-Cryst. Solids* **2012**, *358*, 2424-2427.
- (32) Tsai, C.-H.; Mishra, D. K.; Su, C.-Y.; Ting, J.-M.; *Int. J. Energy Res.* **2014**, *38*, 418-428.
- (33) Kim, S. D.; Kim, H. J.; Yoon, K. H.; Song, J.; *Sol. Energy Mater. Sol. Cells* **2000**, *62*, 357-368.
- (34) Zheng, Z.; Yao, J.; Yang, G.; *ACS Appl. Mater. Interfaces* **2017**, *9*, 7288-7296.
- (35) Mueller, B. J.; Zimmerman, C.; Huang, V.; Hergert, F.; Koehler, T.; Zweigart, S.; Herr, U.; *J. Appl. Phys.* **2014**, 174503.
- (36) Chavhan, S.; Sharma, R.; *J. Phys. Chem. Solids* **2006**, 767-773.
- (37) Zaretskaya, E. P.; Gremenok, V. F.; Zalesski, V. B.; Bente, K.; Schorr, S.; Zukotynski, S.; *Thin Solid Films* **2007**, 5848-5851.
- (38) Wada, T.; Kohara, N.; Nishiwaki, S.; Negami, T.; *Thin Solid Films* **2001**, *387*, 118-122.
- (39) Haneda, M.; Kintaichi, Y.; Bion, N.; Hamada, H.; *Appl. Catal., B* **2003**, *42*, 57-68.
- (40) Proffit, D. E.; Buchholz, D. B.; Chang, R. P. H.; Bedzyk, M. J.; Mason, T. O.; Ma, Q.; *J. Appl. Phys.* **2009**, *106*, 113524.
- (41) Proffit, D. E.; Ma, Q.; Buchholz, D. B.; Chang, R. P. H.; Bedzyk, M. J.; Mason, T. O.; *J. Am. Ceram. Soc.* **2012**, *95*, 3657-3664.
- (42) Zhang, P.; *J. Phys. Chem. C* **2014**, *118*, 25291-25299.

(43) Chevrier, D. M.; Meng, X.; Tang, Q.; Jiang, D.-e.; Zhu, M.; Chatt, A.; Zhang, P.; *J. Phys. Chem. C* **2014**, *118*, 21730-21737.

(44) MacDonald, M. A.; Chevrier, D. M.; Zhang, P.; Qian, H.; Jin, R.; *J. Phys. Chem. C* **2011**, *115*, 15282-15287.

(45) Chevrier, D. M.; MacDonald, M. A.; Chatt, A.; Zhang, P.; Wu, Z.; Jin, R.; *J. Phys. Chem. C* **2012**, *116*, 25137-25142.

## 7 Concluding Remarks and Future Outlook

### 7.1 Concluding Remarks

This research focused on creating low-cost and environmentally-friendly methods to produce CuInS<sub>2</sub> (CIS) and CuInSe<sub>2</sub> (CISe) films for use in solar cells. The development of two distinct methods of fabricating the light-absorbing layer were explored: electrochemical deposition of Cu and In followed by an annealing/selenization process, and nanocrystal (NC) fabrication and deposition.

Photoelectrochemical (PEC) measurements were employed as a measure of the quality of the films based on the amount of photocurrent produced. In this way, the films were optimized to produce the largest amount of photocurrent possible.

CIS NCs were fabricated using a simple solvothermal method that was performed at a low temperature in ambient atmosphere. These NCs produced a high photocurrent without any toxic conditions or post-processing at high temperatures. This was due to the use of a short-chain capping ligand with a pyridimine ring that could facilitate electron movement. Using PEC measurements, the starting conditions were optimized for both the amount of photocurrent produced, and the relative speed of the photoreactions. The CIS NCs were found to be in the chalcopyrite phase, and the atoms were in the following oxidation states: Cu(I), In(III) and S<sup>2-</sup>. The NCs sizes were around 2 nm, but they conglomerated into larger structures promoting electron transport through the film.

The CIS NCs were probed with synchrotron radiation. It was concluded that they were free from secondary phases, and that the NCs that produced the highest photocurrent had a uniform crystal lattice with less intrinsic defects. The capping ligand bonded to the NCs via its terminal sulfur, the pyrimidine ring, or both. The bond through the thiol cannot be too strong as this was observed to decrease the photocurrent produced by the NCs. The pyrimidine ring donated electron density to the high-photocurrent CIS NCs and the interaction was much stronger in NCs that demonstrated a large photocurrent.

A CIS NC monolayer on a metal oxide back contact was created to explore the photoelectrochemistry of the CIS NCs. Using a linker molecule (3-mercaptopropyl)trimethoxysilane (MPTMS), the surface of a fluorine-doped tin oxide coated piece of glass was functionalized. The CIS NCs then associated with the MPTMS through the terminal sulfur creating a monolayer of CIS. The photocurrent observed from this film of CIS was on the same order of magnitude as that observed from a CIS film that was 1 to 2  $\mu\text{m}$  thick. This is due to a more efficient capture of the photogenerated electrons by the  $\text{MV}^{2+}$ , leading to an increased speed of the photoreactions. XANES confirmed that the MPTMS linked CIS NCs have no structural changes compared to the CIS NCs alone.

Post processing of the CIS NC film revealed that a low-temperature (250 °C) heating under inert atmosphere produced a photocurrent enhancement. This temperature was a balance between several factors. It increased the grain size and crystallinity of the NCs, without being so high as to increase cracks and burn off the capping ligand. When CdS was added and this low-temperature annealing step was performed, an increase in photocurrent was observed. When a further layer of CdS was added, a significant increase in photocurrent was achieved. This is due to crack filling and a more homogenous distribution of the CdS. The post-synthetic annealing process increased the photocurrent so substantially that its benefits may significantly outweigh its cost.

Electrochemical deposition (ECD) of copper and indium followed by selenization in a vacuum furnace to form  $\text{CuInSe}_2$  (CISe) directly on the back contact was the final investigation in this work. CISe fabricated using this method produced the highest photocurrents out of all the different techniques discussed in this work. The material produced from an indium-rich starting ratio produced the highest photocurrent, and a pure phase CISe film. ECD produced a highly-crystalline, relatively-homogenous CISe layer that, when incorporated into a full device, produced an efficiency of 0.01%. The effect of sulfur incorporation into the CISe crystal lattice through S substituting for Se was investigated using XRD and EXAFS. While  $\text{CuIn}(\text{S},\text{Se})_2$  has many advantageous properties, the sulfur intercalation into the film may need to be better controlled before its full potential for solar cell development can be realized.

Solar cells are poised to become a main source of energy for the world. The global abundance of solar energy makes it a great candidate to be a worldwide renewable energy. This work on CIS/CISe light-absorbing films has delved into methods and techniques that have the potential to significantly reduce the costs associated with this technology, whilst keeping them environmentally friendly. The NC synthesis is carried out in normal atmosphere, at low temperature, and does not use any toxic solvents or conditions. It creates pure-phase CIS NCs that can be easily incorporated into a variety of different deposition techniques. Some of these techniques include inks for deposition, linking the NCs to the surface using MPTMS, and spin coating a dispersion of the NCs onto the substrate. The ECD of a Cu/In bilayer followed by annealing and selenization uses easily scalable methods and produces a low amount of waste.

## 7.2 Future Work

The next big step to pursue in this research is to build full devices incorporating all of the optimized CIS and CISe techniques that were developed in this thesis. The CIS NCs require further optimization to produce solar cell devices with an appreciable efficiency. The uniform deposition of the NCs and further investigation into how each additional layer addition affects the NC layer is needed. Investigation into the individual heterojunctions with regards to morphology, lattice matching, and the conditions for a more efficient electron transfer may provide more information on how to increase the efficiency of the final device. Investigations how each layer added affects the resistivity of the device could be performed. The substitution of the CdS buffer with a Zn(O,S) film would make the solar cells even more environmentally sustainable.

Further development of the ECD process needs to be completed to achieve a higher efficiency from CISe and the removal of the less dense surface structures to obtain a better contact between layers. The ECD of the more inexpensive CIS is required to further reduce costs associated with this technology. The photocurrents observed from these films are still not as high the ones produced by the CISe, most likely due to the lack of adhesion on the CIS to the molybdenum. The parameters of the sulfurization process need further optimization to overcome this issue. The process for the sulfurization of the metallic stacks to create the lower cost CIS may need considerable work to find the

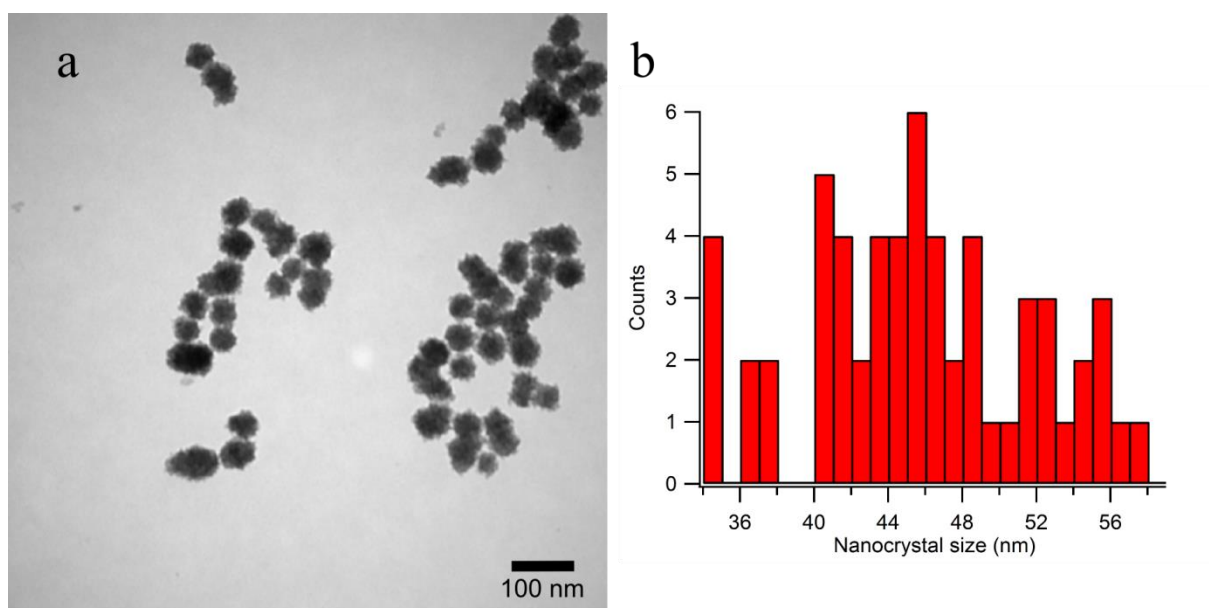
conditions that produce a film that shows photocurrent which is comparable to the CISE films.

The low-cost, non-toxic techniques developed in this thesis will reduce the costs associated with producing solar cells, making their large scale implementation closer to a reality. If this is accomplished, the global reliance on fossil fuels and the resulting devastation to our planet can be eliminated.



## List of Appendices

## Appendix A

**Chapter 3: Assessing the Band Structure of CuInS<sub>2</sub> Nanocrystals and Their Bonding with the Capping Ligand**

**Figure S3.1. a) TEM image of the high photocurrent CIS nanoparticles b) size distribution of the CuInS<sub>2</sub> nanoparticles determined from TEM.**

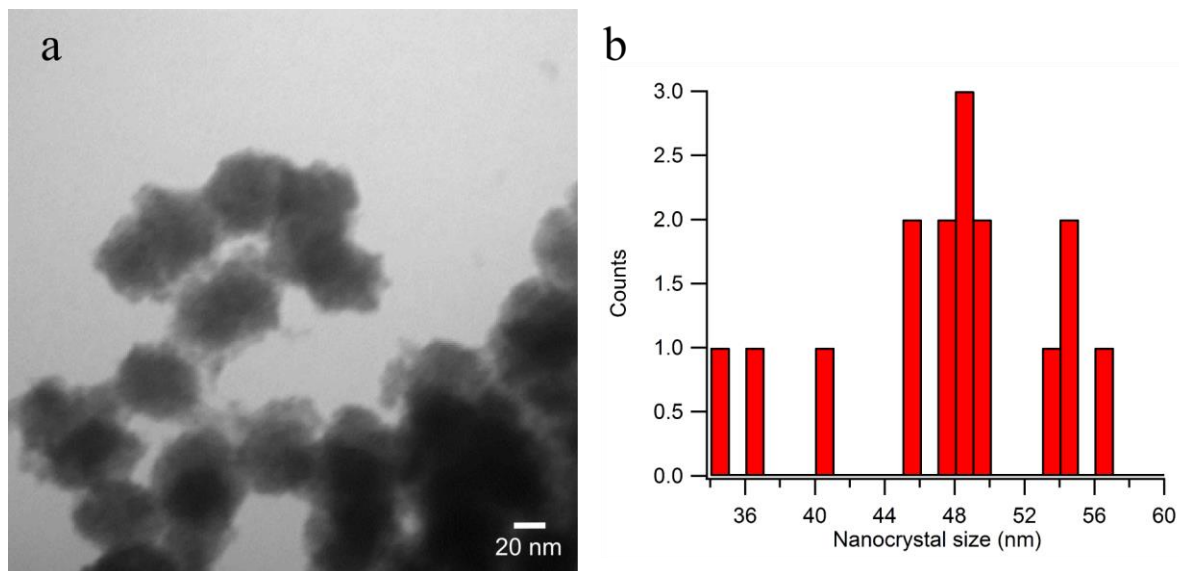


**Figure S3.2. a) TEM image of the low photocurrent CuInS<sub>2</sub> nanoparticles b) size distribution of the CuInS<sub>2</sub> nanoparticles determined from TEM.**

#### **Chapter 4: Characterization of a CuInS<sub>2</sub> Monolayer Linked to FTO by Photoelectrochemistry and X-ray Absorption Spectroscopy**

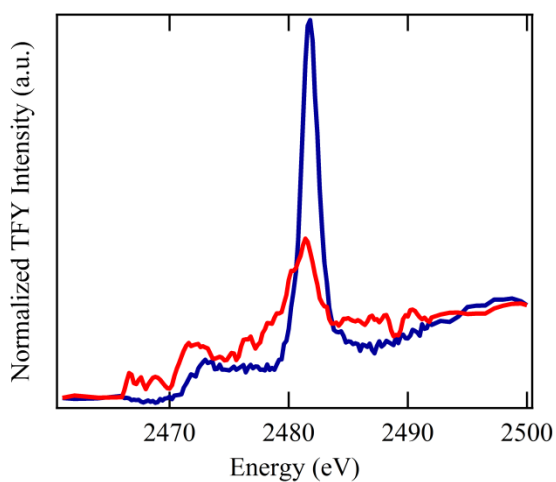


**Figure S4.1 The S K-edge for FTO alone in TFY (blue) and TEY (red).**

## Appendix B: Copyrights

RE: Copy Right Permission for a Thesis

**Subject:** RE: Copy Right Permission for a Thesis  
**From:** Gill Cockhead [REDACTED]  
**Date:** 2017-06-27 2:24 AM  
**To:** [REDACTED]

Dear Amy

The Royal Society of Chemistry (RSC) hereby grants permission for the use of your paper(s) in the printed and microfilm version of your thesis. You may also make available the PDF version of your paper(s) that the RSC sent to the corresponding author(s) of your paper(s) upon publication of the paper(s) in the following ways: in your thesis via any website that your university may have for the deposition of theses, via your university's Intranet or via your own personal website. We are however unable to grant you permission to include the PDF version of the paper(s) on its own in your institutional repository. The Royal Society of Chemistry is a signatory to the STM Guidelines on Permissions (available on request).

Please note that if the material specified below or any part of it appears with credit or acknowledgement to a third party then you must also secure permission from that third party before reproducing that material.

Please ensure that the thesis states the following:  
For the paper from *RSC Advances*; and

Reproduced by permission of The Royal Society of Chemistry  
For the paper from PCCP:

reproduced by permission of PCCP Owner Societies

Links should also be include back to the papers on the Royal Society of Chemistry's website.

Please ensure that your co-authors are aware that you are including the paper in your thesis.

Regards  
Gill Cockhead  
Publishing Contracts & Copyright Executive

Gill Cockhead  
Publishing Contracts & Copyright Executive  
Royal Society of Chemistry,  
[REDACTED]

Follow the Royal Society of Chemistry:  
[www.rsc.org/follow](http://www.rsc.org/follow)

Winner of The Queen's Award for Enterprise, International Trade 2013

-----Original Message-----

From: [REDACTED]  
Sent: 26 June 2017 15:32  
To: Gill Cockhead <[REDACTED]>  
Subject: Copy Right Permission for a Thesis

Name: Amy Tapley

RE: Copy Right Permission for a Thesis

Message: Hello

I am unclear how to obtain permission to republish my article as part of a chapter of my thesis.

Thank you

This communication is from The Royal Society of Chemistry, a company incorporated in England by Royal Charter (registered number RC000524) and a charity registered in England and Wales (charity number 207890). Registered office: Burlington House, Piccadilly, London W1J 0BA. Telephone: 0207 4378 6556, Facsimile: 0207 4490 3393 (Head Office). This communication (including any attachments) may contain confidential, privileged or copyright material. It may not be relied upon or disclosed to any person other than the intended recipient(s) without the consent of The Royal Society of Chemistry. If you are not the intended recipient(s), please (1) notify us immediately by replying to this email and delete all copies from your system and (2) note that disclosure, distribution, copying or use of this communication is strictly prohibited. Any advice given by The Royal Society of Chemistry has been carefully formulated but is necessarily based on the information available, and The Royal Society of Chemistry cannot be held responsible for accuracy or completeness. In this respect, any views or opinions presented in this email are solely those of the author and may not represent those of The Royal Society of Chemistry. The Royal Society of Chemistry owes no duty of care and shall not be liable for any resulting damage or loss as a result of the use of this email and/or attachments. The Royal Society of Chemistry acknowledges that a disclaimer cannot restrict liability at law for personal injury or death arising through a finding of negligence. The Royal Society of Chemistry does not warrant that its emails or attachments are Virus-free: Please rely on your own screening.



RightsLink®

Home

Account  
Info

Help



**Title:**

Assessing the Band Structure of  
CuInS<sub>2</sub> Nanocrystals and Their  
Bonding with the Capping Ligand

Logged in as:

Amy Tapley

LOGOUT

**Author:**

Amy Tapley, Lijia Liu, Xiaoyu Cui,  
et al

**Publication:**

The Journal of Physical Chemistry  
C

**Publisher:**

American Chemical Society

**Date:**

Sep 1, 2015

Copyright © 2015, American Chemical Society

#### PERMISSION/LICENSE IS GRANTED FOR YOUR ORDER AT NO CHARGE

This type of permission/license, instead of the standard Terms & Conditions, is sent to you because no fee is being charged for your order. Please note the following:

- Permission is granted for your request in both print and electronic formats, and translations.
- If figures and/or tables were requested, they may be adapted or used in part.
- Please print this page for your records and send a copy of it to your publisher/graduate school.
- Appropriate credit for the requested material should be given as follows: "Reprinted (adapted) with permission from (COMPLETE REFERENCE CITATION). Copyright (YEAR) American Chemical Society." Insert appropriate information in place of the capitalized words.
- One-time permission is granted only for the use specified in your request. No additional uses are granted (such as derivative works or other editions). For any other uses, please submit a new request.

BACK

CLOSE WINDOW

Copyright © 2017 Copyright Clearance Center, Inc. All Rights Reserved. [Privacy statement](#). [Terms and Conditions](#).  
Comments? We would like to hear from you. E-mail us at [customer@copyright.com](mailto:customer@copyright.com)



**Note:** Copyright.com supplies permissions but not the copyrighted content itself.

1  
PAYMENT

2  
REVIEW

3  
CONFIRMATION

### Step 3: Order Confirmation

**Thank you for your order!** A confirmation for your order will be sent to your account email address. If you have questions about your order, you can call us 24 hrs/day, M-F at +1.855.239.3415 Toll Free, or write to us at [info@copyright.com](mailto:info@copyright.com). This is not an invoice.

**Confirmation Number: 11652368**  
**Order Date: 06/26/2017**

If you paid by credit card, your order will be finalized and your card will be charged within 24 hours. If you choose to be invoiced, you can change or cancel your order until the invoice is generated.

#### Payment Information

Amy Tapley  
atapley2@uwo.ca  
+1 (519) 520-3842  
Payment Method: n/a

#### Order Details

##### Journal of the Electrochemical Society

**Order detail ID:** 70585159  
**Order License Id:** 4136540103878  
**ISSN:** 0013-4651  
**Publication Type:** Journal  
**Volume:**  
**Issue:**  
**Start page:**  
**Publisher:** ELECTROCHEMICAL SOCIETY,  
**Author/Editor:** ELECTROCHEMICAL SOCIETY

**Permission Status:** **Granted**

**Permission type:** Republish or display content  
**Type of use:** Republish in a thesis/dissertation

**Requestor type:** Academic institution

**Format:** Print, Electronic

**Portion:** chapter/article

**Title or numeric reference of the portion(s):** Chapter 6 entire Chapter

**Title of the article or chapter the portion is from:** Effect of Annealing on the Photoelectrochemical Behaviour of CuInS<sub>2</sub> Nanocrystal Films

**Editor of portion(s):** N/A

**Author of portion(s):** N/A

**Volume of serial or monograph:** 161

<b>Issue, if republishing an article from a serial</b>	12
<b>Page range of portion</b>	
<b>Publication date of portion</b>	August 16 2014
<b>Rights for</b>	Main product
<b>Duration of use</b>	Life of current edition
<b>Creation of copies for the disabled</b>	yes
<b>With minor editing privileges</b>	no
<b>For distribution to</b>	Worldwide
<b>In the following language(s)</b>	Original language of publication
<b>With incidental promotional use</b>	no
<b>Lifetime unit quantity of new product</b>	Up to 499
<b>Made available in the following markets</b>	Academic
<b>The requesting person/organization</b>	Amy Tapley
<b>Order reference number</b>	
<b>Author/Editor</b>	Amy Tapley
<b>The standard identifier of New Work</b>	N/A
<b>Title of New Work</b>	Optimization of Low-cost CuInS <sub>2</sub> and CuInSe <sub>2</sub> for used in Solar Cells
<b>Publisher of New Work</b>	Western University
<b>Expected publication date</b>	Sep 2017
<b>Estimated size (pages)</b>	130

**Note:** This item will be invoiced or charged separately through CCC's **RightsLink** service. [More info](#)

**\$ 0.00**

---

<b>Total order items: 1</b>	<b>This is not an invoice.</b>	<b>Order Total: 0.00 USD</b>
-----------------------------	--------------------------------	------------------------------



## Curriculum Vitae

**Name:** Amy Tapley

**Post-secondary Education and Degrees:** University of Western Ontario  
London, Ontario, Canada  
2008-2012 H.B.Sc

The University of Western Ontario  
London, Ontario, Canada  
2012-2017 Ph.D.

**Honours and Awards:** Province of Ontario Graduate Scholarship  
2013-2014, 2014-2015

Natural Sciences and Engineering Research Council (NSERC)  
Postgraduate scholarship- Doctoral  
2015-2017

ASPIRE Award for Travel to UCLA in Los Angeles, California  
2015

**Related Work Experience** Teaching Assistant  
The University of Western Ontario  
2012-2017

### Patents:

1. Ding, Z.; Jia, F.; Love, D.; Oh, M.I.; Vaccarello, D.; Tapley, A. **2015** Copper-containing nanocrystals and methods of preparation therefor WO2013091114A1 U.S. Patent 9346686

### Publications:

1. Tapley, A.; Turnbull, M.J.; Swick, K; Ding, Z. Electrochemical Deposition of Light-Absorbing  $\text{CuInSe}_2$  for use in Solar Cells, *Submitted* **2017**
2. Tapley, A; Love, D.A.; Sham, T.-K.; Ding, Z. Characterization of a  $\text{CuInS}_2$  Monolayer Linked to FTO by Polarization Measurements and X-ray Absorption Spectroscopy *Submitted* **2017**
3. Tapley, A.; Liu, L.; Cui, X.; Zuin, L.; Love, D. A.; Zhou, J.; Sham, T.-K.; Ding, Z.; Assessing the Band Structure of  $\text{CuInS}_2$  Nanocrystals and Their Bonding with the Capping Ligand *J. Phys. Chem. C* **2015**, *119*, 20967-20974.
4. Vaccarello, D.; Hedges, J.; Tapley, A.; Love, D. A.; Ding, Z.; Dynamic aspects of  $\text{CuInS}_2$  light absorbing nanocrystal thin films *J. Electroanal. Chem.* **2015**, *738*, 35-39.

5. Tapley, A.; Hart, C.; Vaccarello, D.; Love, D. A.; Ding, Z.; Effect of Annealing on the Photoelectrochemical Behavior of CuInS<sub>2</sub> Nanocrystal Films *J. Electrochem. Soc.*, **2014**, *161*, H725-H729.
6. Vaccarello, D.; Tapley, A.; Ding, Z.; Optimization of the Cu<sub>2</sub>ZnSnS<sub>4</sub> nanocrystal recipe by means of photoelectrochemical measurements *RSC Advances* **2013**, *3*, 3512.
7. Amy Tapley, Daniel Vaccarello, Jason Hedges, Falong Jia, David A. Love, Zhifeng Ding. Preparation and Characterization of CuInS<sub>2</sub> Nanocrystals for Photovoltaic Materials *Phys. Chem. Chem. Phys.*, **2013**,*15*, 1431-6